TOWARDS NON-INVASIVE ULTRASONIC CHARACTERIZATION OF CAROTID ATHEROSCLEROTIC PLAQUES

by

Xuan Ding, B.S.E.

Bachelor of Science in Engineering, Biomedical Engineering, Duke University, 2010

Submitted to the Graduate Faculty of

Swanson School of Engineering in partial fulfillment

of the requirements for the degree of

Doctor of Philosophy in Bioengineering

University of Pittsburgh

2016

UNIVERSITY OF PITTSBURGH

SWANSON SCHOOL OF ENGINEERING

This dissertation was presented

by

Xuan Ding

It was defended on

July 21, 2016

and approved by

Kang Kim, PhD
Dissertation Director
Associate Professor, Department of Medicine and Bioengineering

Sanjeev Shroff, PhD
Professor, Department of Bioengineering

Flordeliza Villanueva, MD
Professor, Department of Medicine

George D. Stetten, MD, PhD
Professor, Department of Bioengineering

Steven P. Jacobs, DSc
Associate Professor, Department of Electrical and Computer Engineering

TOWARDS NON-INVASIVE ULTRASONIC CHARACTERIZATION OF CAROTID ATHEROSCLEROTIC PLAQUES

Xuan Ding, Ph.D.

University of Pittsburgh, 2016

Vulnerable atherosclerotic plaques are thought to be prone to rupture due to various compositional and morphological factors. One key characteristic is thought to be the presence of a soft, lipid rich core in the plaque. Acoustic radiation force impulse (ARFI) and thermal strain imaging (TSI) are non-invasive ultrasound-based imaging modalities. ARFI imaging measures the tissue response to an ultrasonically generated mechanical perturbation. In TSI, the tissue temperature is increased and image contrast is a result of the temperature and composition dependence of the speed of sound.

Initial efforts to develop a TSI system utilized two separate ultrasound transducers for heating and imaging. We developed signal processing to improve estimates of thermal strain obtained from this system and showed that TSI could be used to detect lipids in *ex vivo* human arterial tissue samples. However, the translational obstacles encountered by this system outweighed the potential imaging utility.

In order to address these challenges, we developed temporally interleaved multi-foci beamforming which could be implemented on a standard imaging array to generate a broad, homogeneous ultrasound beam for either ARFI pushing or TSI heating. We showed that this

beamforming approach could enable simultaneous acquisition of ARFI and thermal strain data while substantially improving the frame rate for ARFI imaging.

In order to better understand the factors that affect signal quality in TSI and ARFI imaging, we conducted separate phantom studies for each imaging modality. We showed that with a temperature rise $<1^{o}$C, TSI could differentiate between phantoms with different lipid percentages. Additionally, we showed that pulse inversion harmonic imaging could be used to improve TSI signal quality in the presence of clutter. Finally, we showed that high frame rate ARFI imaging was able to achieve a 45-fold improvement in frame rate at the cost of increased estimation bias and jitter, and decreased image contrast.

These studies indicate that multi-foci beamforming can be used to enable simultaneous TSI and ARFI imaging on current clinical systems. This imaging sequences developed in this dissertation facilitate non-invasive assessment of both the composition and mechanical properties of tissue which might be especially useful for characterization of vulnerable plaques.

TABLE OF CONTENTS

LIST OF TABLES

LIST OF FIGURES

ABBREVIATIONS

ACAS – Endarterectomy for Asymptomatic Carotid Atherosclerosis (Trial)

ARF – Acoustic Radiation Force

ARFI – Acoustic Radiation Force Impulse

CNR – Contrast-to-noise ratio

CEA – Carotid Endarterectomy

CDS – Color Duplex Sonography

COV – Coefficient of Variation

CREST – Carotid Revascularization Endarterectomy Versus Stenting (Trial)

DAS – Delay and sum

eSNR – Electronic signal-to-noise ratio

HIFU – High intensity focused ultrasound

IRB – Internal Review Board

MRI – Magnetic resonance imaging

NASCET – North American Symptomatic Carotid Endarterectomy (Trial)

NIT – Non-invasive thermometry

NXcorr – Normalized Cross Correlation

PIHI – Pulse inversion harmonic imaging

RF – Radiofrequency

SNR – Signal-to-noise ratio

sSNR – Speckle signal-to-noise ratio

TSI – Thermal (Temporal) Strain Imaging

PREFACE

First and foremost, I would like to thank my thesis advisor Dr. Kang Kim for his mentorship and guidance throughout the years. When we first met, I was 21 years old and a child playing at science. Today, if I have achieved competence as a scientist, much of the credit goes to Dr. Kim. I would also like to thank the members of my committee for their advice and assistance throughout my graduate studies. Additionally, I would like to thank the faculty and staff in the Center for Ultrasound Molecular Imaging and Therapeutics and my collaborators for their assistance with my work.

A great deal of the credit for this thesis goes towards the many members of our lab throughout the years including Jaesok Yu, Dr. Deb Dutta and Dr. Ahmed Mahmoud. I would especially like to thank Dr. Man Nguyen for his willingness to engage in an endless number of, at times frustrating, but always enlightening, conversations about life and ultrasound. The nascent beginning of Chapter 3.0 was the topic one such conversation.

A special thanks goes to the incredible friends I have made throughout the years. Each of my friends has made an incredible impact on my life and this work; but I would especially like to thank Randall for the many drinks we've shared throughout this long journey, Mimi and Raisa for opening your homes and making the cold, wintery days during Thanksgiving one of the highlights of every year, and Jo for the countless great talks and adventures. Last on this list of

friends, but certainly not least, is Shweta. It’s been an amazing decade of friendship filled with science, laughs (and tears), and big dreams. I can’t wait to see what the next decade brings.

Finally, I would like to thank my parents who have made every sacrifice imaginable to provide me the opportunities and education from which I have benefited. You put me on the path of learning starting at an early age, helped me map out the road to success, and protected me from countless pitfalls along the way. Thank you.

1.0 INTRODUCTION

1.1 STROKE & CAROTID ATHEROSCLEROTIC DISEASE

A stroke, or cerebrovascular attack, is an acute neurological injury resulting from either ischemia (lack of oxygen) or hemorrhage (bleeding). Ischemic strokes comprise approximately 80% of all strokes. They are caused when the oxygen supply to the brain is impaired resulting in death of brain tissue and permanent neurological injury [1]. The oxygen impairment results from one of two mechanisms: 1) hypoperfusion (low-flow) or 2) embolism and subsequent vascular occlusion. Hypoperfusion injuries occur because of *reduced* flow and typically result in injuries to areas of the brain that draw their oxygen supply from small branching vessels (watershed regions). Embolic strokes occur when a small fragment of material originating from a distant source travels to and occludes a vessel in the brain. In this case, the injury pattern correlates with the region of the brain that is fed by the occluded vessel.

Carotid atherosclerotic disease refers to the buildup of atherosclerotic plaque in the carotid artery. The buildup is typically most severe near the bifurcation of the common carotid artery. Patients in which the buildup reaches or exceeds 70% of the luminal area of the carotid artery are at markedly increased risk for ischemic stroke. These patients are said to have >70% stenosis and account for approximately 10-20% of all cases of stroke [2].

Patients with <70% stenosis are typically managed with medical therapy and lifestyle changes. However, if the stenosis exceeds 70%, surgical removal of the plaque is often considered. Color duplex sonography (CDS), a combination of standard ultrasound B-mode and Doppler imaging, is currently the gold standard for measuring the degree of stenosis. Clinically, these high-grade stenosis patients (>70%) are subdivided into either the symptomatic or asymptomatic groups. Patients with symptomatic carotid disease have >70% stenosis and symptoms of ipsilateral (same-sided) stroke, transient ischemic attack, or amaurosis fugax. Asymptomatic patients have >70% stenosis, but no symptoms.

In symptomatic patients with >70% stenosis, surgical removal (NASCET) or stenting (CREST) of the plaque has been shown to provide a 10.1% absolute reduction in the rate of major stroke or death over 2 years as compared to medical management [3], [4]. However, in asymptomatic patients with >70% stenosis, surgical removal (ACAS) or stenting (CREST) of the plaque provides only a 4.8% absolute reduction in rate of major stroke or death over 5 years as compared to medical management [3], [5]. This corresponds to preventing only a single stroke for every 21 surgeries performed on asymptomatic patients. Additionally, the ACAS trial began in the late 1980's and reported that the rate of stroke was 11.0% over 5 years in medically managed patients or a rate of 2.2% per year [5]. However, in the proceeding decades, aggressive, improved medical therapies in the form of anti-hypertensives, anti-lipid therapies, and anti-platelet therapies have reduced the baseline risk of stroke to 1.68 – 1.99% per year [6]–[8]. Because of these factors, the surgical management of asymptomatic patients with >70% stenosis is a subject of active investigation.

1.2 VULNERABLE ATHEROSCLEROTIC PLAQUES

Although high-grade stenosis is strongly correlated with an increased risk for stroke or cerebrovascular injury, the mechanism of injury is not necessarily the result of hypoperfusion. For example, it has been observed within the clinical literature that even 100% stenosis or complete occlusion of a single carotid artery might not be associated with any neurological deficits [9], [10]. In the case where the stenosis is progressive and not sudden, the body is able to naturally develop and recruit collateral blood vessels to supplement the remaining cranial flow [11]. This point is further illustrated by the fact that the annual incidence of stroke in asymptomatic patients with high-grade stenosis is only approximately 2.2% [5]. Furthermore, it stands to reason that there must be something different about symptomatic patients that results in a much higher incidence of stroke (13% per year) as compared to their asymptomatic counterparts [4].

For these reasons, the medical community has long postulated the existence of "vulnerable atherosclerotic plaques." These plaques are thought to be especially prone to rupture due to various compositional and morphological features of the plaque [12]–[16]. In the case of carotid plaques, rupture leads to the release of thrombogenic materials that embolize to distal intracranial vessels and result in a stroke. Post-mortem and *ex vivo* studies of carotid endarterectomy samples suggest that a lipid rich necrotic core is one common characteristic of vulnerable plaques [17]–[19]. Other vulnerable features include a thin fibrous cap, intraplaque hemorrhage, and microcalcifications [18], [20], [21]. Additionally, complementary biomechanical studies have been conducted that offer explanations as to how these compositional features might lead to plaque instability and rupture [22]. These studies indicate that a *soft* lipid core serves to concentrate stress in the overlying thin fibrous cap [23]–[25].

Despite the wealth of evidence surrounding the vulnerable plaque hypothesis, there are very few *in vivo* human studies to support this hypothesis. Until recently, the primary reason for this dearth of evidence was the inability to non-invasively assess plaque composition. Takaya et al. showed using multi-contrast magnetic resonance imaging (MRI) in 154 asymptomatic patients with 50-79% carotid stenosis that patients with a large lipid rich core at baseline had a hazard ratio of 1.6 for a subsequent cerebrovascular event [26]. Even more recently, Czernuszewicz et al. showed that ultrasound acoustic radiation force impulse (ARFI) imaging could be used to non-invasively identify soft areas in plaque in patients with carotid disease. These areas that were deemed to be soft in the ultrasound image correlated well with the lipid rich necrotic core identified in histological sections [27].

1.3 THERMAL STRAIN IMAGING

Although multi-contrast MRI is currently the best-validated means of imaging carotid plaque composition, it suffers from several drawbacks. First, MRI is an inherently expensive imaging modality due to structural requirements and technical expertise. In addition, optimal image quality is only obtained with exogenous contrast which is contraindicated in certain patients with allergies or kidney failure [28]. Thus, while multi-contrast MRI has the potential to become the gold-standard for non-invasive plaque assessment, there exists a need for a cheap, fast screening tool.

Ultrasound thermal strain imaging (TSI) uses the temperature and composition dependence of the speed of sound to differentiate between lipid and water-based tissues. Figure 1 shows that the speed of sound increases in water with increasing temperature [29], [30].

However, in castor oil, like many biological lipids, the speed of sound decreases with increasing temperature [29], [31], [32]. Clinical ultrasound systems typically measure the time of the returned echoes and use an assumed speed of sound of 1540 m/s to calculate distances. An increase in the actual speed of sound results in a shorter return time for the echoes relative to baseline. In the literature, the name temporal strain imaging has been used interchangeably with thermal strain imaging in order to emphasize that the signal is a temporal shift rather than a true thermally induced mechanical strain.

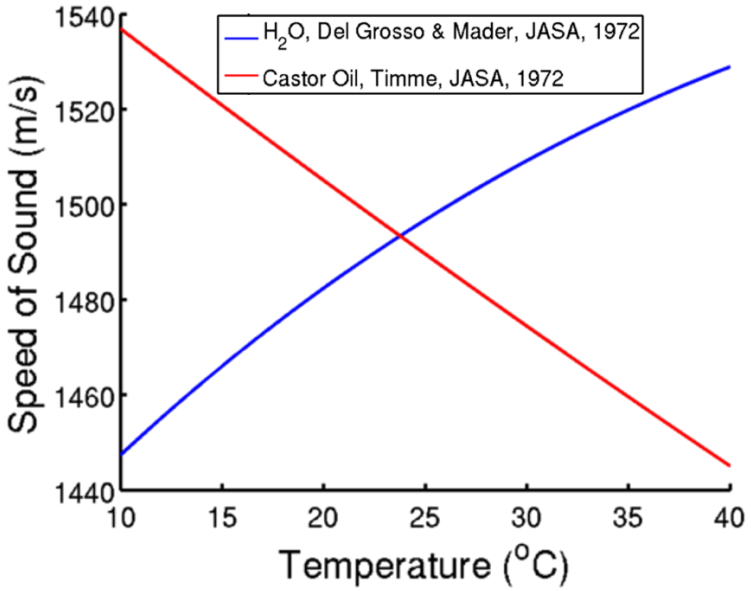

Figure 1: Speed of sound versus temperature for water and castor oil.

As a result of the echo shifts, water-based objects that are heated appear to compress towards the transducer when the time shift is converted into distance by the ultrasound system. In lipid-based media, objects appear to stretch away from the transducer. Typically, a temperature increase of 0.5–2^{o}C is sufficient to generate a measurable change in sound speed while

simultaneously minimizing any true mechanical strains generated from thermal expansion. Overall, these physics can be mathematically summarized with Equation 1:

$$\frac{du}{dz} = -\beta \Delta T.$$

Equation 1: Governing equation for TSI. "Thermal" or "temporal" strain (derivative of displacement), $\frac{du}{dz}$; Sound speed coefficient (%/ºC), β; Temperature change, ΔT.

A typical TSI sequence is presented in Figure 2 and consists of three parts. First, a reference image is captured. Second, a small temperature change is induced. Finally, a post-heating image is captured.

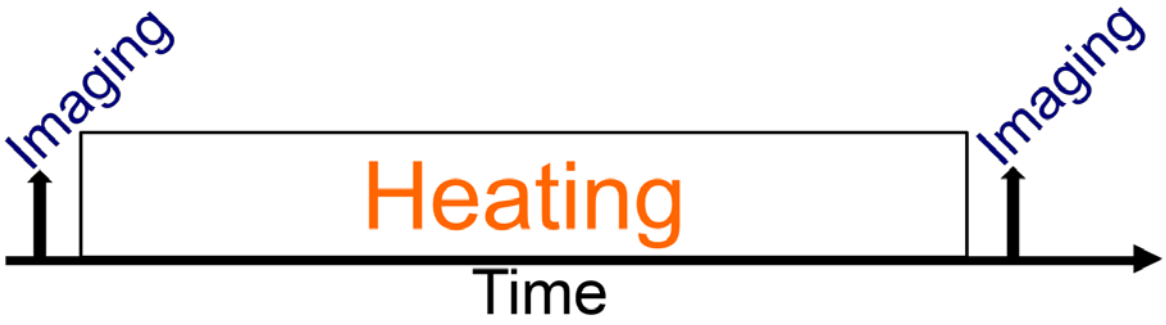

Figure 2: General TSI sequence.

The relative displacements between the reference and post-heating images are calculated and a derivative in the direction of wave propagation yields the thermal or temporal strain. Due to the technical difficulty of generating a broad, homogeneous heating beam, efforts to implement TSI on a clinical ultrasound scanner and probe have been limited [33]–[35]. Instead, separate arrays have been used for heating and imaging [36].

1.4 ACOUSTIC RADIATION FORCE IMPULSE IMAGING

ARFI imaging is an ultrasound imaging modality that utilizes the mechanical response of soft tissue to acoustic radiation force as the source of image contrast. The force is generated by the transfer of momentum from the propagating ultrasonic wave into an attenuating medium. The force generated is a body force with magnitude defined by Equation 2 [37].

$$F = \frac{2\alpha I}{c}$$

Equation 2: **Governing equation for the magnitude of acoustic radiation force. Force, F; Absorption coefficient, α; Intensity of ultrasonic wave, I; ultrasound wave speed, c.**

The tissue mechanical response depends on the applied force as well as tissue mechanical properties, geometry, and boundary conditions. However, if the applied force is distributed homogeneously, stiff structures will generally have small displacements and softer structures will have larger displacements. An ARFI imaging sequence typically consists of a reference A-line, a long (≥500 cycles) ultrasonic "push" pulse, and a series of on-axis tracking A-lines to monitor the dynamic mechanical response. This dynamic response typically has a maximum displacement on the order of microns and lasts for <10 ms.

ARFI imaging provides exquisite image contrast in mechanically heterogeneous structures. However, interpretation of images can be challenging due to the range of factors that can influence the eventual mechanical response. Additionally, due to the nature of the push and tracking pulses, ARFI imaging frame rates are typically <5 Hz [37], [38]. One logistical advantage of ARFI imaging is that it can be implemented onto standard clinical ultrasound

scanners and probes purely through pulse sequence modifications. In part because of this ease of translation, ARFI has been used in numerous *in vivo* human settings [27], [39]–[42].

1.5 THESIS OUTLINE

The purpose of this thesis is to demonstrate the feasibility of implementing a combined TSI/ARFI imaging sequence onto a standard ultrasound platform and probe for assessment of carotid atherosclerotic plaques.

Chapter 2 explores initial efforts to improve signal processing of TSI data acquired using a high frequency imaging probe and a separate high efficiency heating probe. Recognizing the limitations of such a system, Chapter 3 covers the development of novel beamforming methods that enable the implementation of combined ARFI-TSI sequences onto standard ultrasound systems. We show that this novel beamforming approach is able to be utilized for both TSI heating and ARFI pushing and is compatible with a single linear array transducer. Chapter 4 is a parametric study of sequence parameters, target composition, and tracking modes that affect TSI image quality. Similarly, Chapter 5 explores the effects of novel tracking and pushing beams on ARFI image quality. Chapter 6 discusses the implications of this work on translational efforts and future work motivated by these studies.

2.0 AN ADAPTIVE DISPLACEMENT ESTIMATION ALGORITHM FOR IMPROVED RECONSTRUCTION OF THERMAL STRAIN

The work presented in this chapter was reprinted, with permission, from X. Ding, D. Dutta, A. M. Mahmoud, B. Tillman, S. A. Leers, and K. Kim, "An Adaptive Displacement Estimation Algorithm for Improved Reconstruction of Thermal Strain," IEEE Transaction on Ultrasonics, Ferroelectronics, and Frequency Control, vol. 62, no. 1, pp. 138–151, Jan. 2015.

2.1 INTRODUCTION

For TSI, Equation 1 relates the derivative of the apparent displacement, u, in the direction of sound propagation (axial direction, z) to the change in temperature, ΔT, through a material constant β [43]–[45]. The quantity $\frac{\partial u}{\partial z}$ is referred to as the "thermal strain". Because TSI uses a small temperature change (≤2°C), the induced thermal strain is relatively small (≤1.0%) when compared to strains typically generated by ultrasound elastography imaging. However, small strains can still lead to large apparent displacements. In fact, when the temperature of a region that is several millimeters thick is increased by 1-2°C, a large dynamic range of displacement is generated (0–50 μm) with small displacements present near the top of the heated region and large displacements present near the bottom of the heated region.

Displacement estimation using ultrasound to track tissue motion and deformation has been well-studied in the literature and has led to a wealth of estimators and a rich analysis of the

properties of these estimators. One of the earliest estimators that is still widely used is normalized cross-correlation (NXcorr) [46], [47]. Other groups have described modified versions of NXcorr that include phase-sensitive estimation and iterative temporal stretching in order to improve estimation accuracy and computational efficiency [48]–[50]. In addition to NXcorr, Loupas' estimator and higher dimensional variations are also used to track tissue motion [51], [52]. Complementary studies have also been published that examine and compare the properties of many different estimators [53], [54]. Even more recently, novel algorithms that incorporate multi-level searches and Bayesian estimation approaches have been proposed [55]–[57].

However, in spite of the wide array of estimation algorithms, NXcorr and Loupas' estimator remain widely used [58], [59]. NXcorr and Loupas' estimator represent two fundamentally different formulations of the displacement estimation problem [60]. When estimation is formulated as a phase-shift estimation problem, it leads to a class of estimators commonly known as autocorrelation algorithms which include Kasai and Loupas' estimator [51], [61]. On the other hand, when displacement estimation is posed as a time-shift estimation problem, it can be shown that NXcorr, with appropriate filtering, is the maximum likelihood estimator [62].

We observed that, during TSI experiments, displacement tracking errors for time-shift and phase-shift estimators were localized to the top and bottom of the target, respectively. These tracking errors resulted in underestimation of the target dimensions in these regions when the strain was reconstructed from the displacement. We hypothesized that these errors happened because time-shift estimators improperly estimated small displacements and phase-shift estimators underestimated large displacements. One of the applications of TSI currently being investigated is the identification of lipid cores of atherosclerotic plaques in the carotid artery.

Although carotid plaques are a target of great clinical interest, they are challenging to image because the typical carotid artery is 6.10 – 6.52 mm in diameter [63], [64]. This means that in a typically sized artery with 70% stenosis, the target plaque will have an area of only 20.4 - 23.4 mm^2. Furthermore, it is expected that the lipids within the plaque will be localized to a necrotic core which comprises only a small portion of the total plaque area [64]. Anatomical differences between patients may further complicate displacement tracking because the depth of the artery will vary from patient to patient [65]. The thermal strain in the artery is linearly proportional to ΔT and β which implies that the measured displacement is proportional to the integral of these quantities. Thus, a lipid pool within a carotid plaque will experience a range of displacements that depend upon its relative position within the heating beam.

Although a median filter or another similar filter can be used to increase the SNR and potentially alleviate some of these issues, aggressive filtering can result in the loss of small spatial details and does not help to recover a phase-wrapped signal. The observed differences in the performance of Loupas' estimator and NXcorr, coupled with the challenges related to imaging carotid plaques, motivated the development of a new adaptive displacement estimation algorithm that would have robust performance over a large range of displacements. The goal of this adaptive displacement estimation algorithm was to provide more accurate displacement estimates that would result in thermal strain reconstructions with improved strain SNR and spatial accuracy.

In this study, we examined the properties of the Loupas' estimator and NXcorr over a range of displacements and noise levels that were typically observed during TSI of atherosclerotic plaques using computer simulations. Using these results, we created an adaptive estimation algorithm that combined estimates from Loupas' estimator and NXcorr. We showed

that this adaptive estimation algorithm provided superior performance when compared to either Loupas' estimator or NXcorr alone. Finally, we applied the algorithm to an *ex-vivo* amputated femoral artery of a human subject.

2.2 MATERIALS AND METHODS

2.2.1 Conventional Displacement Estimation

Displacement estimation was conducted using Loupas' estimator and NXcorr. Unless otherwise specified, the axial kernel for displacement calculations was 128 μm or 1.8λ. Loupas' estimate for displacement was calculated as in [53]. Loupas' estimator calculates displacement based off of the quadrature demodulated data or IQ data and is shown in Equation 3.

$$u = \frac{c}{4\pi f_c} \frac{\operatorname{atan}\left(\frac{\sum_{m=0}^{M-1}\sum_{n=0}^{N-2}[Q(m,n)I(m,n+1) - I(m,n)Q(m,n+1)]}{\sum_{m=0}^{M-1}\sum_{n=0}^{N-2}[I(m,n)I(m,n+1) + Q(m,n)Q(m,n+1)]}\right)}{1 + \operatorname{atan}\left(\frac{\sum_{m=0}^{M-1}\sum_{n=0}^{N-2}[Q(m,n)I(m+1,n) - I(m,n)Q(m+1,n)]}{\sum_{m=0}^{M-1}\sum_{n=0}^{N-2}[I(m,n)I(m+1,n) + Q(m,n)Q(m+1,n)]}\right)/2\pi},$$

Equation 3: Loupas' estimator. The real, I, and imaginary Q, parts of the quadrature demodulated data; Speed of sound, c; Ultrasound center frequency, f_c; Size of axial kernel, M; Size of temporal kernel, N.

The numerator calculates the average phase difference between a reference and shifted signal. When the four-quadrant inverse tangent function is used to calculate the phase difference, the result is bounded by ±π which corresponds to displacements on the range of ±λ/2. Because

medical ultrasound relies on the two-way propagation time, the maximum displacement that can be estimated is effectively bounded by ±λ/4. The denominator is a frequency normalization term to account for local variations in the center frequency. For a more thorough analysis of Loupas' estimator, the reader is referred to [51] and [53].

NXcorr calculates the displacement by finding the lag between a reference and shifted signal at which the correlation coefficient is maximized. For 1-D NXcorr, this can be expressed mathematically as Equation 4.

$$u = \frac{c}{2f_s} \arg\max_{\tau} \frac{\sum_{i=-M/2}^{M/2} y_0^*(i) y_1(i+\tau)}{\sum_{i=-M/2}^{M/2} [y_0(i)]^2 \sum_{i=-M/2}^{M/2} [y_1(i+\tau)]^2}.$$

Equation 4: Normalized cross-correlation. The reference, y_0, and shifted y_1, signal; Speed of sound, c; System sampling frequency, f_s; Size of the axial kernel, M.

Here, the signals are assumed to be complex numbers formed from the IQ data such that $y = I + jQ$ and $y^* = I - jQ$. Typical ultrasound scanners use a sampling frequency of 40 MHz which does not yield sufficient displacement resolution to track the displacements generated in low strains scenarios. As a result, the data set is typically upsampled. In order to further improve the displacement resolution, the peak of the cross correlation function is typically calculated using interpolation. These procedures yield displacement estimates with sub-micron quantization error. However, it should be noted that, as a result of these steps, the quantization error is not typically the limiting factor for modern displacement estimation in ultrasound imaging. For a more thorough analysis of NXcorr, the reader is referred to [53], [62].

For 1-D NXcorr, the IQ data were upsampled to 420 MHz. The cross-correlation coefficient was calculated from the magnitude of the baseband signal and the peak of the cross-

correlation coefficient was estimated using parabolic interpolation. 1-D NXcorr was used to estimate displacement for all simulation data. 2-D NXcorr was implemented to account for small lateral displacements observed during *ex-vivo* experiments that likely resulted from vibrations in the room. The lateral kernel size for 2-D displacement calculations was 0.32 mm or three A-lines. For 2-D NXcorr, the IQ data were upsampled to 420 MHz axially and the final displacement estimate was calculated using 2-D parabolic interpolation.

2.2.2 Ultrasound Radiofrequency (RF) 1-D Data Simulation

We conducted 1-D ultrasound simulations to verify our empirical observation that Loupas' estimator and NXcorr performed differently depending on the magnitude of displacement being tracked. In addition, we expanded the investigation to include the performance of these estimators for a wide range of scatterer densities and noise levels. The RF pulse was simulated with a center frequency of 21 MHz and a 50% bandwidth which corresponded to the specifications of the linear array transducer (MS250, FUJIFILM, Visualsonics Inc, Canada) used in *ex-vivo* experiments. The RF data were synthesized to simulate a line of scatterers experiencing a constant strain of 0.05% over 55 mm. This resulted in a linear displacement ramp with a displacement range from 0 μm to 27.5 μm. This range of displacement extends beyond the phase-wrapping limit ($\lambda/4$) for Loupas' estimator and is a good representation of displacements found in TSI. The received echo signal for the reference and shifted signals were simulated according to the following model:

$$r(t) = [x(t) * s(t)] + n(t).$$

Equation 5: Model for the received echo. Gaussian enveloped RF pulse, $x(t)$; Scatterer distribution, $s(t)$; White Gaussian system noise, $n(t)$; Received RF signal, $r(t)$.

Scatterer positions were drawn from a uniform distribution and the amplitude of the scatterers was drawn from a normal distribution. The scatterer density was varied from 0.37 – 11.0 scatterers per -3 dB width of the enveloped RF pulse. These scatterer densities correspond to calculated scatterer SNR (sSNR) of 0.79 – 1.83. Additive, white Gaussian noise was used to simulate electronic system noise present in real imaging systems. The electronic SNR (eSNR) ranged from 8.6 – 50.4 dB which corresponds to the range of SNR found in typical ultrasound systems. The received RF signal was converted to IQ data and saved with a sampling frequency of 40 MHz in order to mimic the signal processing found in typical commercial ultrasound scanners. The displacement was calculated for these simulated lines of scatterers using both Loupas' estimator and 1-D NXcorr. This process was repeated for 1000 independent scatterer realizations. Tissue attenuation of ultrasound was not accounted for in these simulations, but was incorporated into Field II simulations of TSI [66].

To evaluate the properties of the estimators, we used percent bias and coefficient of variation as metrics which are shown in Equation 6 and Equation 7. The COV of the Cramer-Rao lower bound (CRLB) was also calculated using the formulation in reference [67]. The results of these metrics were plotted as a function of simulated displacement magnitude in order to derive thresholds which specified the optimal performance regions for Loupas' estimator and NXcorr. The corresponding levels of eSNR and sSNR were also stored for future use with the adaptive displacement estimation algorithm.

$$\%\ bias = \frac{u_{True} - E[u_{Est}]}{u_{True}} \times 100,$$

Equation 6: Percent bias. True displacement, u_{True}; Expected value of estimated displacement, $E[u_{Est}]$.

$$COV = 20 \log_{10} \frac{\sigma_{Est}}{u_{True}}.$$

Equation 7: Coefficient of variation. True displacement, u_{True}; Sample standard deviation of the estimated displacements, σ_{Est}.

2.2.3 Adaptive Displacement Estimation Algorithm

Based on the simulation results, an algorithm was designed to minimize the percent bias and COV. Figure 3 is a flowchart outlining the steps in the adaptive estimation algorithm which are described in more detail below.

Step 1) We computed the displacement estimate using both NXcorr (u_{NXcorr}) and Loupas' estimator (u_{Loupas}) separately and used these estimates to compute an estimate for u_{True}, the true displacement. Unlike simulations, the true displacement is not known in real imaging scenarios. For this reason, we computed the mean displacement at every position between the two algorithms as an estimate for the true displacement.

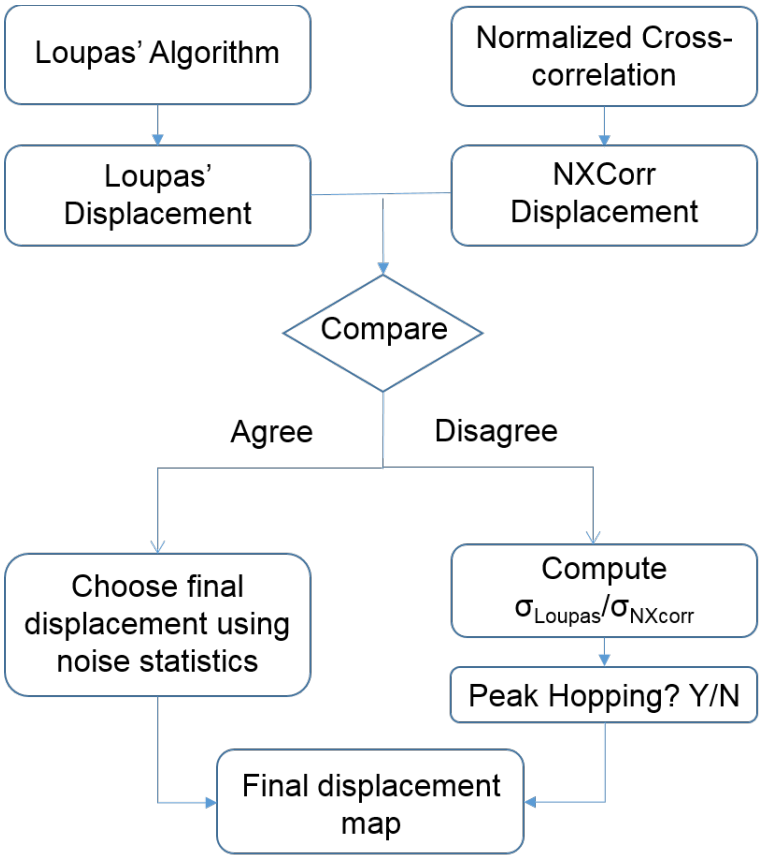

Figure 3: Flow chart describing the adaptive displacement estimation algorithm.

$$u_{mean}(z_i) = \frac{u_{Loupas}(z_i) + u_{NXcorr}(z_i)}{2}.$$

Equation 8: The mean displacement as an estimate of the true displacement. Mean displacement, u_{mean}; Loupas displacement estimate, u_{Loupas}; NXcorr displacement estimate, u_{NXcorr}; Spatial location, z_i

Step 2) If Loupas' estimate and the NXcorr estimate were both within ±50% of u_{mean} at a given z_i, then we considered the two algorithms to be in agreement. Empirically, it was found that the bias and variance in Loupas' estimate and NXcorr often resulted in estimates that were within ±30% of u_{mean} in the absence of phase-wrapping or peak-hopping errors. In the presence of phase-wrapping or peak-hopping, the difference in the estimates relative to u_{mean} was often

in excess of ±100%. A threshold of ±50% was chosen empirically in order to take into account these factors and because the accuracy of u_{mean} as an estimate for u_{True} was unknown.

If in agreement: Step 3) The eSNR and sSNR were estimated by acquiring a series of conventional B-mode frames. Let $I_j(x,y)$ be the IQ data for the *j*th frame collected prior to heating. If we assume that the electronic system noise is additive white Gaussian noise, then the temporal average is a good estimate of the true value of the IQ data in the absence of electronic noise when the number of frames, *N*, is large. The sSNR can also be estimated as the ratio of the mean and the standard deviation of $\bar{I}(x,y)$ in a local spatial kernel.

$$eSNR(x,y) = 20\,log\frac{\bar{I}(x,y)}{\sqrt{\frac{1}{N-1}\sum_{j=1}^{N}\left(I_j(x,y)-\bar{I}(x,y)\right)^2}}.$$

Equation 9: An estimate for the electronic SNR (eSNR), Temporal average of the IQ data, $\bar{I}$; Total number of frames, N.

$$sSNR(x,y) = \frac{\frac{1}{x_0y_0}\sum_{j=y}^{y+y_0}\sum_{i=x}^{x+x_0}\bar{I}(i,j)}{\sqrt{\frac{1}{x_0y_0-1}\sum_{j=1}^{N}\left(I_j(x,y)-\bar{I}(x,y)\right)^2}},$$

Equation 10: An estimate for the speckle SNR (sSNR), Temporal average of the IQ data, $\bar{I}$; Total number of frames, N; The axial, x_0, and lateral, y_0, kernel size.

The calculated values of eSNR and sSNR were used to choose two appropriate displacement thresholds from the stored simulation data. One threshold was derived using the percent bias metric and the other was derived from the COV metric. If u_{mean} was below both of

these displacement thresholds, then the Loupas estimate was used. The NXcorr estimate was used if u_{mean} was greater than both of these thresholds. However, if u_{mean} lay somewhere between the two displacement thresholds, then a weighted estimate, u_{weight}, was generated:

$$u_{weight} = (1 - \alpha)u_{Loupas} + \alpha u_{NXcorr}$$

Equation 11: A linearly weighted displacement estimate. Weighted displacement estimate, u_{weight}; Loupas displacement estimate, u_{Loupas}; NXcorr displcament estimate, u_{NXcorr}, weighting factor, α

$$\alpha = \frac{|u_{mean}| - |u_{Th,Loupas}|}{|u_{Th,NXcorr}| - |u_{Th,Loupas}|}$$

Equation 12: Weighting factor. Mean displacement of Loupas and NXcorr estimates, u_{mean}; COV or % bias threshold with the smallest magnitude, $u_{Th,Loupas}$; COV or % bias threshold with the largest magnitude, $u_{Th,NXcorr}$.

Thus, α had a value that always ranged from zero to one. When α was zero, the final estimate was equal to the estimate from Loupas' estimator. From there, α changed linearly as a function of u_{mean} until it was equal to one and the final estimate was equal to the displacement estimate from NXcorr.

If not in agreement: Step 3) If the two algorithms did not agree, it was likely because of other errors. Peak-hopping errors can occur with both Loupas' estimator and NXcorr whereas a phase-wrapping error is unique to phase-based estimators like Loupas' estimator. Typically, displacement estimates change smoothly along the axial dimension. However, in the case of a peak-hopping error, there is an interruption in this smooth change. By utilizing this observation, peak-hopping errors could detected by computing and comparing the standard deviation of the

Loupas and NXcorr estimates within a 50 μm region about z_i. A large increase in the standard deviation in one algorithm that was not present in the other indicated a peak-hopping error. Otherwise a phase-wrapping error was likely and the NXcorr estimate was chosen.

2.2.4 Simulation of Thermal Strain Imaging

A region 30 mm (axial) X 14 mm (lateral) X 4 mm (elevation) was populated with 50,000 randomly generated scatterers in order to generate a reference configuration prior to heating. A cylindrical target with a radius of 3 mm was centered at 22 mm axially. Scatterers in this region had a mean signal strength that was 40 dB greater than the background. The material constant β was chosen to be -0.4 %/^{o}C for the cylindrical target and zero for the background. The temperature rise, ΔT, was set to be 1^{o}C which corresponded to a maximum displacement of 24 μm. The values of β and ΔT were chosen so that the simulated displacements mimicked values typically seen in tissue [43]. The temperature change was assumed to be uniform across the target. A second configuration that corresponds to the speckle distribution after heating was generated by shifting the scatterers according to these specifications.

Field II, a linear acoustic simulation package, was used to simulate imaging with a linear array transducer (MS250, FUJIFILM, Visualsonics Inc, Canada) [66]. The center frequency for the transducer was set to be 21 MHz with a 50% bandwidth. The B-mode transmit and receive foci were set to 23 mm and used an F/2 configuration. The Field II data was stored with a sampling frequency of 40 MHz in order to mimic commercial ultrasound scanners. All other Field II simulation parameters were consistent with the specifications of the MS250 provided by the manufacturer. The ultrasound attenuation coefficient was set to 0.5 dB/cm/MHz. After generating images with Field II, white Gaussian noise was added to the image of the reference

configuration to generate 30 reference images for use with the adaptive algorithm. The same noise was also added to the image of the post-heating configuration. The SNR for these images was set to 35 dB. These data were used as the input for Loupas' estimator, 1-D NXcorr, and the adaptive estimation algorithm. In order to compare the performance of the adaptive algorithm with median filtering, displacement estimates were also filtered where noted. A 2-D median filter was applied in the axial direction. A kernel length of 55 X 135 μm or 3 X 3 pixels (axial X lateral) was used. The derivative of displacement along the axial direction was calculated using a first order Savitzky-Golay filter with a 1.0 mm kernel length to estimate thermal strain.

The entire simulation procedure outlined in this section was repeated for 25 randomly generated scatterer distributions. The percent error is defined as the absolute value of the percent bias (Equation 6). The target size was defined as the area within the target with >0% strain. For a single speckle realization, the strain SNR was calculated using Equation 12. Differences in target size and strain SNR were evaluated using Tukey's range test for multiple comparisons. Differences with p-values <0.001 were considered to be significant.

$$SNR_{strain} = \frac{\bar{s}_{target}}{\sigma_{target}}$$

Equation 13: Strain SNR (SNR_{strain}). Mean strain within the target, $\bar{s}_{target}$; Standard deviation of strain within the target, σ_{target}.

2.2.5 Ex-vivo Human Amputation Specimen and Thermal Strain Imaging

The femoral artery and the surrounding neurovascular bundle from an above-knee amputation were obtained under Internal Review Board consent approved at the University of Pittsburgh. The specimen was embedded in a gelatin background which was fabricated by combining gelatin (G-2500, Sigma Aldrich Corp., St. Louis, MO), water, and ultrasound scatterers (1% cellulose by wt, S3504, Sigma Aldrich Corp., St. Louis, MO) [68]. The specimen was placed in the liquid gelatin matrix and the gelatin was allowed to cool and solidify.

The specimen was simultaneously imaged and heated using the MS250 with a custom heating transducer that provided a broad heating beam [36]. The MS250 was stabilized with a mechanical arm. The heating transducer was composed of six elements that were attached to the imaging transducer through a plastic manifold and were geometrically focused such that energy was deposited from approximately 20 – 30 mm axially in an 8 mm X 2 mm (lateral X elevational) tissue volume that was centered in the imaging plane. Prior to heating, 30 consecutive reference frames were captured to calculate eSNR and sSNR for use with the adaptive displacement estimation algorithm. Then, heating pulses and imaging pulses were interleaved with the heating transducer being driven with a 56% duty cycle and the imaging being conducted at 10 Hz. Imaging was conducted at 21 MHz and IQ data was sampled at 40 MHz and saved for offline processing.

Displacement was estimated using Loupas' estimator, 2-D NXcorr, and the adaptive estimation algorithm as described in 2.2.1 and 2.2.3. 2-D NXcorr was used in order to compensate for small lateral displacements that were present due to vibrations in the room. Only axial displacements from 2-D NXcorr were used in the adaptive algorithm. The thermal strain was calculated using a first order Savitzky-Golay filter with a 1.5 mm kernel length. The strain in

regions with B-mode signal amplitudes smaller than 50 dB was ignored because the B-mode signal in this region was too poor to provide meaningful displacement estimates. The small signal amplitude likely resulted from tissue attenuation. All aforementioned computational tasks were implemented and performed in MATLAB R2013b (Mathworks Inc., MA) on an Intel i7-2600 3.40 GHz quad-core (Intel Corp., CA) machine with 12 gigabytes of memory. After imaging, Oil Red O histology was performed to identify regions with lipids [69].

2.3 RESULTS & DISCUSSION

The percent bias for several levels of eSNR and sSNR is shown in Figure 4. Figure 4 demonstrates that Loupas' estimator produced less biased estimates than NXcorr when the displacement was small and in imaging situations with low eSNR and sSNR. We found that the performance of NXcorr improved with increasing eSNR, sSNR, and displacement magnitude. Figure 4 also shows that for a given eSNR and sSNR, there exists a displacement magnitude above which NXcorr estimates are less biased than Loupas' estimates. In general, it was found that for an eSNR $\leq$25.5 dB and a displacement magnitude $\leq\lambda/8$, Loupas' estimator was less biased than NXcorr. Conversely, when the eSNR was >25.5 dB and the displacement magnitude was $>\lambda/8$, NXcorr was less biased than Loupas' estimator. These data are presented graphically in Figure 6a.

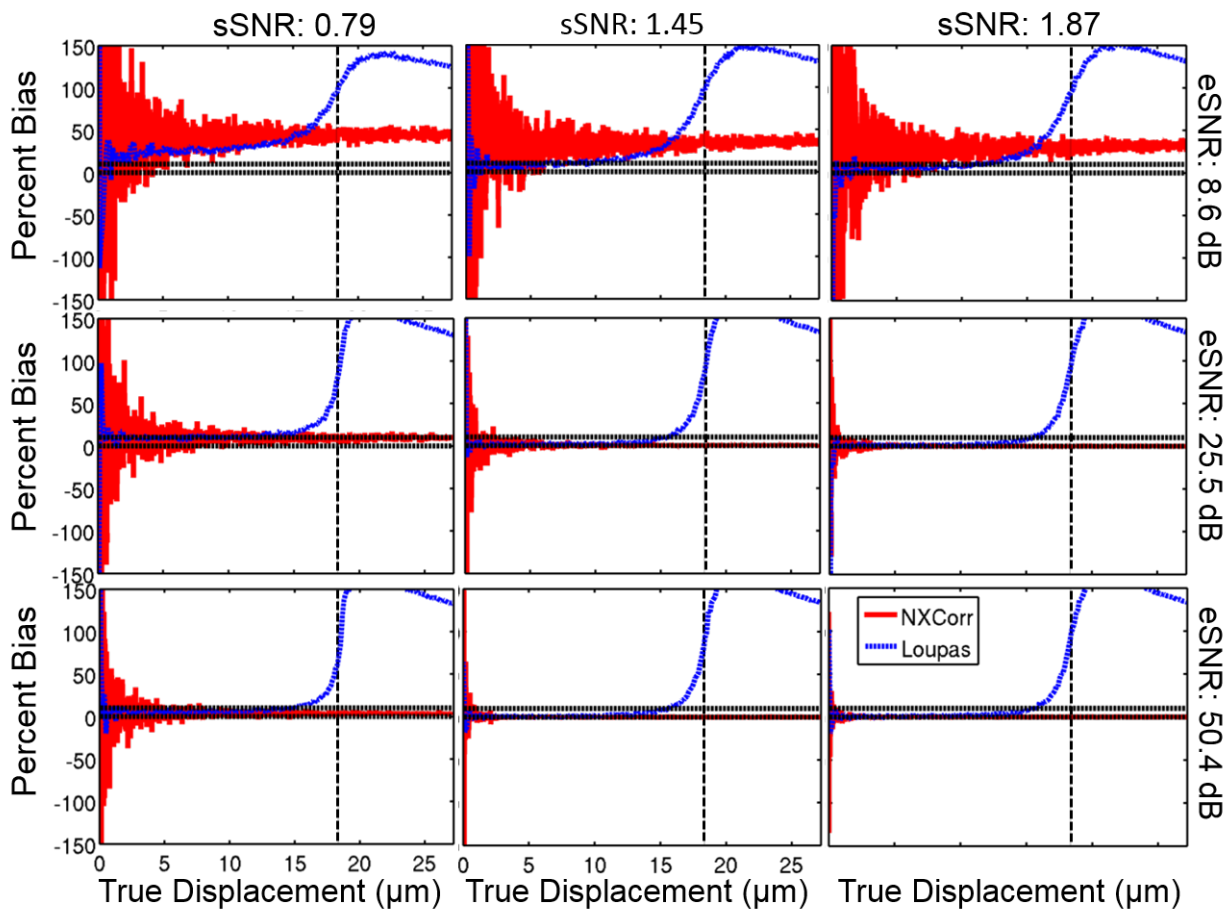

Figure 4: Percent bias as a function of displacement for the Loupas and NXcorr. Rows represent different levels of eSNR. Columns represent different sSNR. The horizontal black lines represent 0% and 10% bias. The vertical dashed line represents λ/4 displacement.

Figure 5 shows that similar trends are observed for the performances of Loupas' estimator and NXcorr when the COV is evaluated. Loupas' estimator produces estimates with smaller variance than NXcorr for small displacements, low eSNR, and low sSNR. The thresholds based on the COV corresponding to optimal ranges for Loupas' estimator and NXcorr are presented graphically in Figure 6b.

Figure 6b shows that Loupas' estimator has better performance for a wider range of noise levels and displacements when the COV metric is used as compared to the percent bias metric. However, NXcorr rapidly becomes the preferred estimator for medium and high SNR. In

general, we found that the COV was smaller for Loupas' estimator when the eSNR was ≤25.5 dB and the displacement magnitude was ≤λ/4. Conversely, when the eSNR was >25.5 dB and the displacement magnitude was >λ/4, NXcorr had smaller variance than Loupas' estimator.

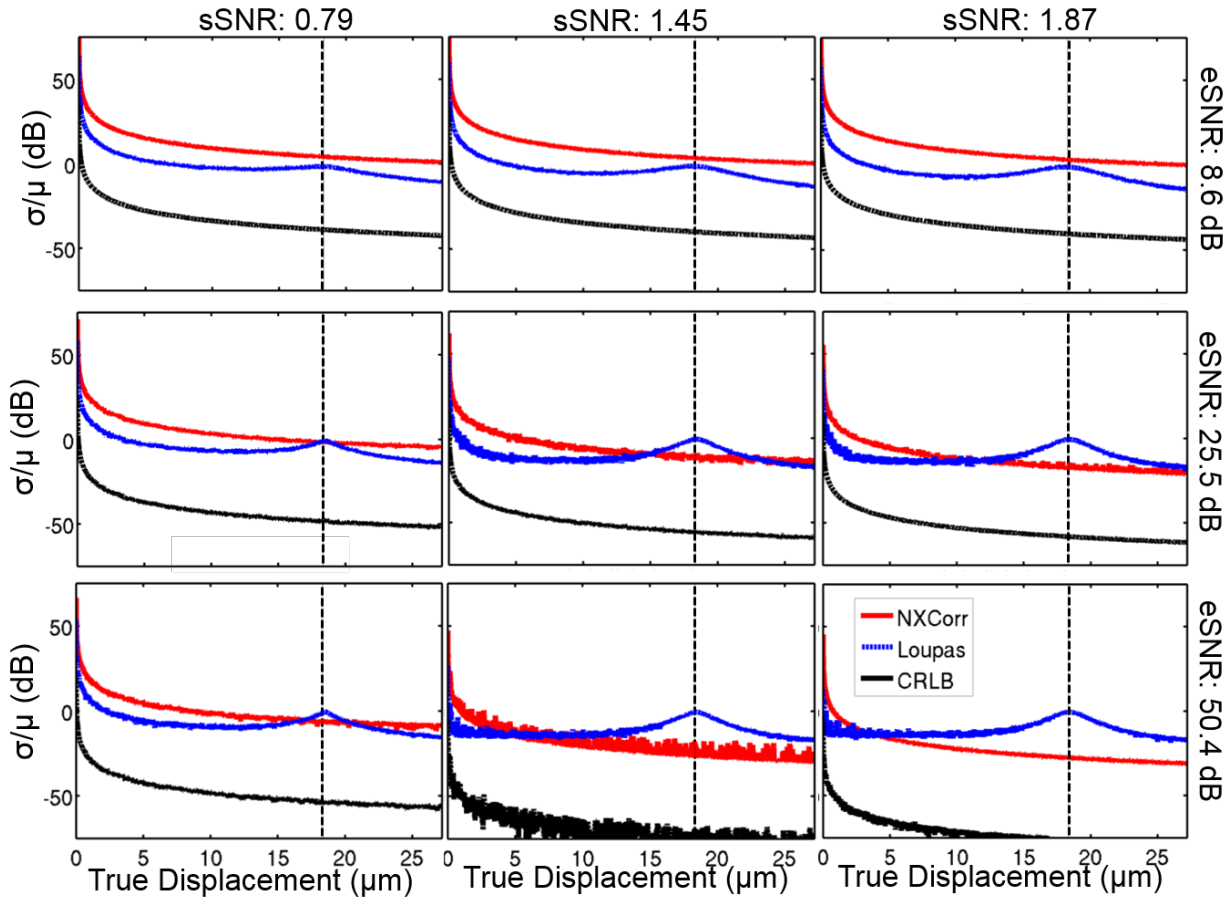

Figure 5: The coefficient of variation as a function of displacement for the Loupas, Nxcorr, and the CRLB. Rows represent different levels of eSNR. Columns represent different sSNR. The vertical dashed line represents λ/4 displacement.

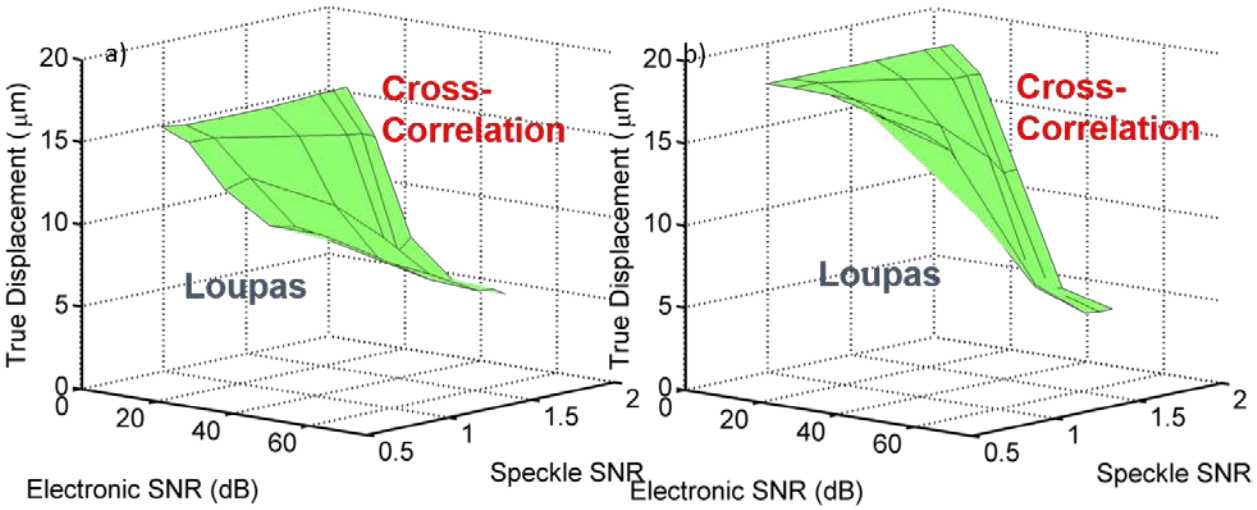

Figure 6: Performance maps for Loupas and NXcorr. a) and b) The true displacement at which Loupas' estimator and NXcorr have equal percentage bias and percentage variance respectively is plotted as a surface for different values of eSNR and sSNR. The space below the surfaces indicates the region in which estimates from Loupas either have less percentage bias or percentage variance than NXcorr and vice versa for the space above the surface.

In order to estimate eSNR and sSNR in real imaging situations, we used the procedure outlined in section 2.2.3. Panel a) in Figure 7 shows the percent bias for the IQ data as a function of imaging depth after averaging different numbers of frames. Panel b) of Figure 7 shows the average root mean square error per pixel for IQ data as a function of number of frames averaged. In both cases, the average of 100 frames was considered to be the "true" value. From these plots, it can be seen that after averaging more than 30 frames, there is little benefit in continued averaging. These data sets served as the rationale for using 30 frames to calculate eSNR and sSNR.

The top row of images in Figure 8 show displacement estimates for a single simulated speckle realization. The displacement images have been cropped and overlaid on the B-mode image to show displacement in the region where β was non-zero. This region corresponds to the true location and size of the inclusion. The strain images are shown in the second row.

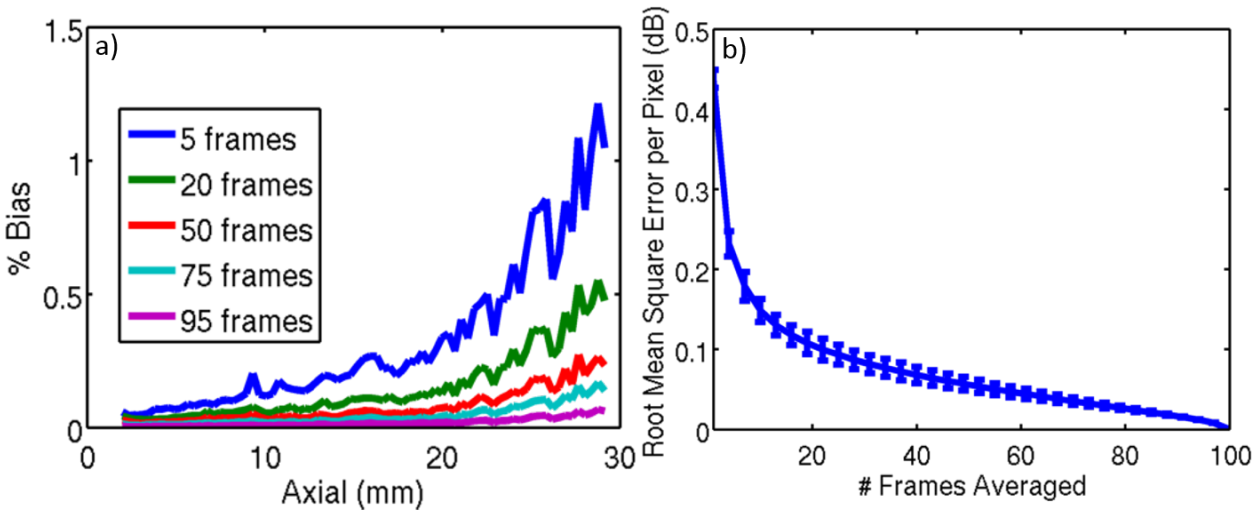

Figure 7: Effect of averaging on IQ data: a) indicates the % bias as a function of depth after averaging different numbers of B-mode frames. b) indicates the average RMS error per pixel between the # of frames averaged and the "true" value. Error bars represent the standard deviation of the RMS error across all pixels in a single frame. In both plots, the average of 100 frames was considered to be the "true" value when calculating % bias.

Figure 8a shows that the B-mode image overestimated the size of the inclusion. This is a direct result of the point spread function of the transducer. In addition, panel d), shows that Loupas' estimator underestimated large displacements. This is consistent with the theory underlying a phase-based estimator as well as simulation data in Figure 4. Large displacements beyond the phase-wrapping threshold were confined to the lower portion of the target (Figure 8a). This is because the thermal strain is the derivative of the apparent displacement. As such, constant thermal strain yields a linear displacement ramp which serves to localize small and large displacements to the top and bottom of the target, respectively. NXcorr and the adaptive algorithm did not suffer from phase-wrapping and the displacement estimates near the bottom of the target in Figure 8b and Figure 8c have less error than the corresponding region in the target tracked by Loupas' estimator (Figure 8d).

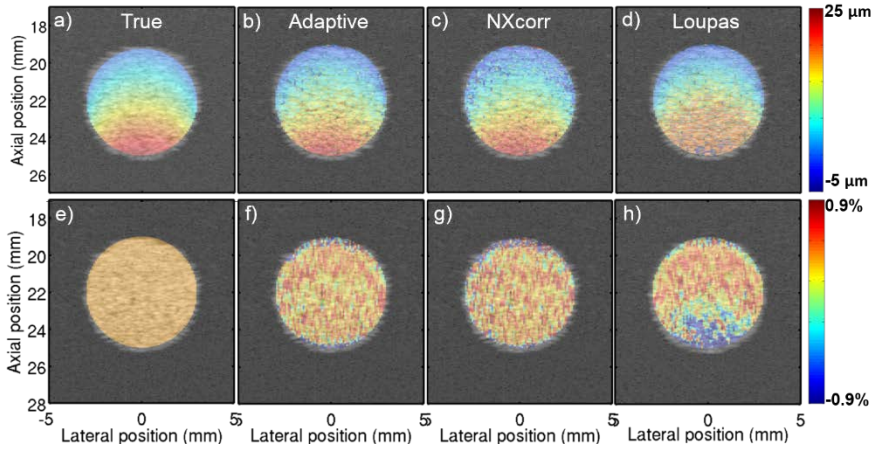

Figure 8: Displacement and TSI images for one set of computer simulations. TSI was simulated using Field II to image a cylindrical inclusion with β = -0.4 % $^{o}C^{-1}$ and where a 1^{o}C uniform temperature change was assumed. The 2nd, 3rd, and 4th columns show results from adaptive algorithm, NXcorr, and Loupas respectively. The true displacement and strain are overlaid on the B-mode image in panels a) and e) respectively. The strain and displacement within the inclusion were cropped and overlaid on the B-mode image

This result is more apparent in Figure 9a, Figure 9b, and Figure 9c which show the mean displacement error across 25 speckle realizations. Figure 8h shows that strain calculated from Loupas' estimator results in underestimation of the lesion only near the bottom of the lesion. As expected, Figure 8f and Figure 8g show that the strain calculated from the adaptive and NXcorr displacement estimates does not suffer from this error.

In the top row of images in Figure 9, the average percent displacement error is shown for each algorithm. The average percent displacement error is shown for the filtered displacement estimates in the second row of images. Strain was calculated as described in section 2.2.4 for both the unfiltered and filtered displacement estimates. The calculated target size is shown for unfiltered and filtered versions of each algorithm in Figure 9g. All possible pairs are significantly different ($p < 0.001$) in Figure 9g. Similarly, the strain SNR for each algorithm is shown in Fig. Figure 9h. The strain SNR is significantly different for all possible pairs ($p < 0.001$) except

between the A-NXF and L-LF pairs.

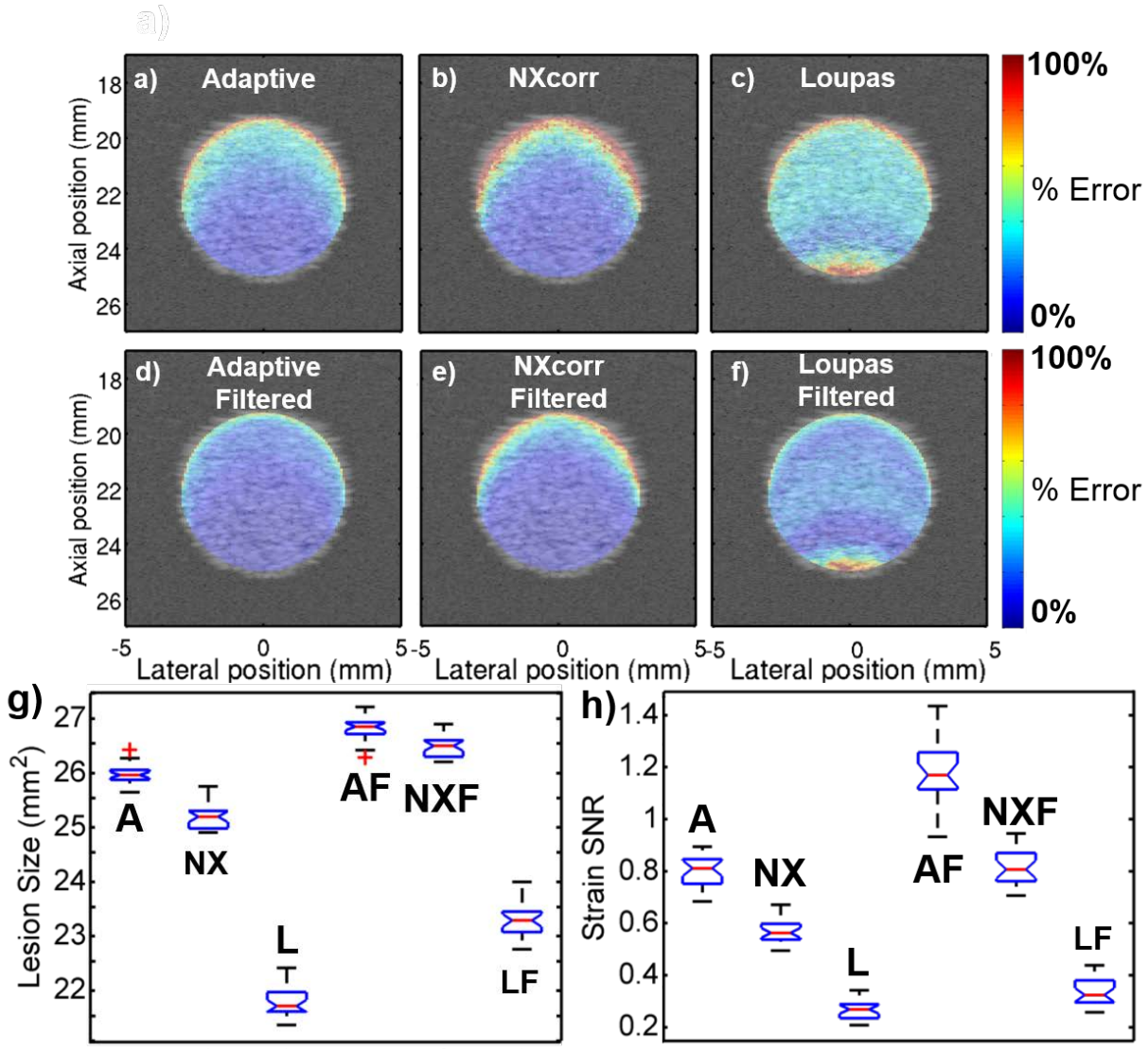

Figure 9: Displacement error and strain results from 25 simulated speckle realizations. The first row of images is the average displacement error calculated from the unfiltered displacement estimates. The second row of images is the average displacement error calculated from median filtered displacement estimates. Stain was calculated from the displacement estimates. Plots g) and h) are box and whisker plots of the target size and strain SNR. Error bars represent the interquartile range and '+' indicate outliers. A, NX, and L are where the original displacements were calculated from the adaptive, Nxcorr, and Loupas' estimator respectively. An 'F' indicates the filtered version of that algorithm. The true target size was 28.3 mm^2. All possible pairs in g) and significantly different ($p < 0.001$). In h), all pairs are significantly different except the A-AF, NX-NXF, and L-LF pairs ($p < 0.001$).

Figure 9c shows that, on average, the error in Loupas' estimator was localized to a thin rim near the top of the target and a larger region near the bottom of the target. This trend agrees with the data that was presented in Figure 4 in which the bias in Loupas is highest when the displacement is less than one micron or greater than the phase wrapping threshold. Figure 9b demonstrates that the error in NXcorr is localized to regions near the top of the target with small displacements. This effect was masked in Figure 8b due to the choice of the dynamic range, but follows the same trend as the data shown in Figure 4. Furthermore, Figure 9a shows that the overall error from the adaptive algorithm is the minimum combination of error from NXcorr and Loupas' estimator.

The second row of images in Figure 9 demonstrates that median filtering can be used to further decrease the displacement error. Figure 9g and Figure 9h demonstrate that strain calculated from the filtered, adaptive algorithm (AF) provided a 1.2 – 23.0% improvement in spatial accuracy and a 43.7 – 350% improvement in strain SNR as compared to the strain calculated from the filtered and unfiltered NXcorr (NXF, NX) and Loupas estimates (LF, L). The filtered version of the adaptive algorithm (AF) provided the best spatial accuracy and strain SNR (Figure 9g and Figure 9h). In most cases, as might be expected, the median filtered versions of the displacement estimates provided significantly better results than the unfiltered versions. The difference in the strain SNR between the filtered and unfiltered version of Loupas' estimator was not significant at the $p < 0.001$ level but was significant if this threshold was relaxed to $p < 0.05$. It is important to note that although the adaptive algorithm was shown to perform better than Loupas' estimator or NXcorr individually, we expect that the exact degree of improvement will depend on the range of displacement being tracked as well as the eSNR and sSNR.

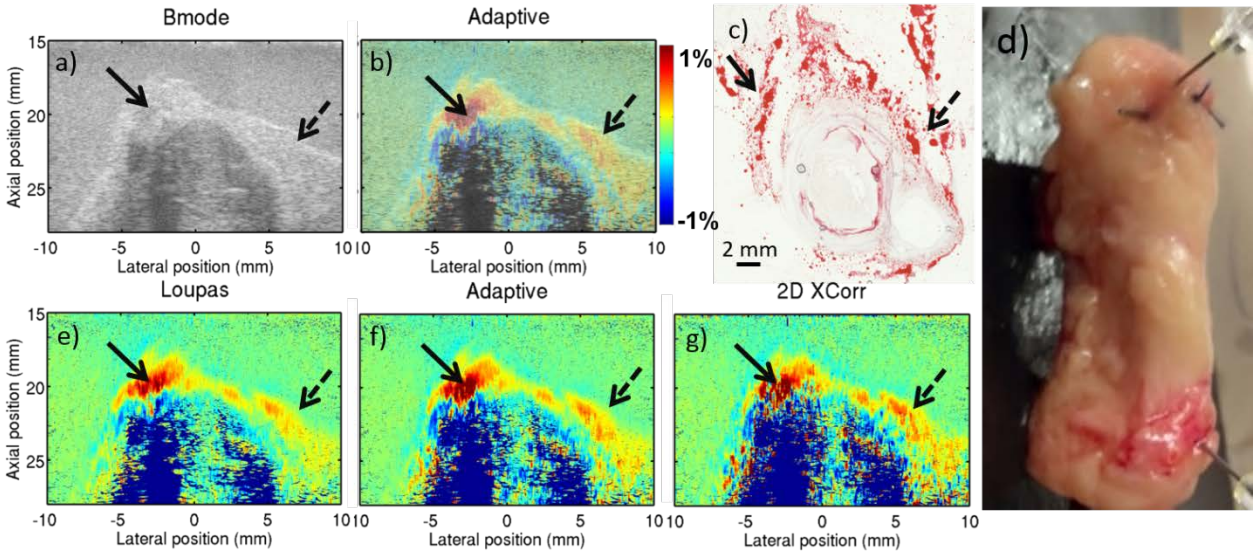

Figure 10: B-mode, TSI-B-mode overlay, and Oil red O histology for an *ex vivo* amputation sample in panels a), b), and c) respectively. In c), bright red staining indicates regions with lipids. A gross image of the specimen is shown in d). Thermal strain was calculated from displacement estimated using Loupas, 2D XCorr, and the adaptive algorithm in panels e), f) , and g) respectively. The dynamic range for the strain images is ±1.0% strain. The heated region corresponds to the entire region being shown. The strain in regions where the B-mode intensity was <50 dB was masked in b), e), f), and g). The black arrows indicate a layer of adventitial fat at the top of the tissue.

Figure 10 shows thermal strain images of an *ex-vivo* arterial specimen embedded in gelatin, corresponding Oil red O histology, and a gross image of the specimen. Approximately the entire region that is displayed was insonified with the heating transducer. In the B-mode image in Figure 10a, there is a hyperechoic layer that is surrounded by a hypoechoic interior. Oil red O staining in Figure 10c shows that this layer corresponds to a layer of bright red staining that is consistent with adventitial fat that surrounding the femoral artery. These observations are further supported by gross images of the vessel in Figure 10f where the artery is buried in a sheath of pale, yellow, adventital fat. All of the thermal strain images confirm that the hyperechoic layer was fatty and surrounded a core of water-based tissue. The black arrows point to deposits of fat that were identified in thermal strain reconstructions from all three algorithms. The strain SNR in the region indicated by the solid arrow was 1.77, 1.11, 2.03 for Loupas'

estimator, NXcorr, and adaptive estimator respectively. The strain SNR in the region indicated by the dashed arrow was 3.04, 2.12, 3.25 for Loupas' estimator, NXcorr, and adaptive estimator respectively.

The simulation results in Figure 8 and Figure 9 are consistent with the *ex-vivo* data presented in Figure 10. Figure 10e, Figure 10f, and Figure 10g, show that the adaptive algorithm provided the best strain SNR within the adventitial layer. A comparison of Figure 10e, Figure 10f, and Figure 10g shows that the lower edge of the fatty deposit indicated by the solid black arrow is missing from Figure 10e. This region was near the bottom of the adventitial layer and experienced large displacements close to or beyond the phase-wrapping threshold. As a result, Loupas' estimator underestimated the displacement in this region which resulted in an incorrect strain estimate. The strain reconstruction from the adaptive algorithm (Figure 10f) appeared to provide the best reconstruction of this region.

The CRLB is the smallest possible variance that an unbiased estimator can achieve and it predicts that the variance in the estimate should increase with increasing displacement magnitude due to signal decorrelation [67]. We quantified the variance in the estimate using the COV which was found to decrease as a function of increasing displacement magnitude. However, the *absolute* magnitude of the variance (data not shown) increased with increasing displacement magnitude which was consistent with the prediction from the CRLB and [67]. In this study, we presented bias and variance as quantities normalized to the displacement magnitude because, the relative error in the estimate is more important than the absolute error for strain estimation.

Previous studies have examined the performance of Loupas' estimator and NXcorr in response to a number of different variables including, eSNR and displacement magnitude [53]. Pinton *et al.*'s simulations applied a constant displacement and imaged with a center frequency

of 5 MHz. Pinton *et al.*, found that when the true displacement was small (~λ/12) and the eSNR was extremely low (6 dB), Loupas' estimator was less biased than NXcorr. However, this result was not generalized to other eSNR. In addition, the effects of sSNR on the respective algorithms were not studied. The simulations presented in this study were designed to mimic TSI in which strain is more likely to be constant within a given tissue type. Furthermore, our study used a center frequency of 21 MHz which corresponded to the center frequency for the ultrasound transducer used in *ex-vivo* experiments (MS250). These factors might account for some of the differences in results seen between this study and previous studies.

One limitation of this study was that the simulation experiments used to derive the displacement thresholds for the adaptive algorithm assumed a simplistic 1-D model for ultrasonic tracking. Palmeri *et al*. investigated ultrasonic tracking of acoustic radiation force induced displacements [70]. They showed that a number of parameters including tracking frequency, transducer bandwidth, and elevational focusing could affect the bias and variance of displacement estimates. A 1-D simulation experiment does not account for transducer focusing in the lateral and elevational directions. Despite neglecting these factors, the results presented showed that the adaptive algorithm performed better than Loupas' estimator and NXcorr.

The adaptive estimation algorithm presented does not rely solely on changes in signal processing. It also requires the acquisition of a series of reference frames in order to calculate image statistics. In this implementation, 30 reference frames were used to calculate these statistics. Assuming a typical clinical imaging depth of 50 mm and an ultrasound array transducer with 128 beams, this corresponds to an imaging time of 265 ms.

Another key concern is related to the safety of actively heating tissue. AIUM standards state that a 2^{o}C temperature change can be sustained for more than 50 hours without significant,

adverse, biological effects [71]. However, it is still desirable to limit the total energy being delivered due to the difficulty of accurately predicting the temperature change *in-vivo*. The adaptive displacement estimation algorithm presented might serve as one means of addressing this concern because it is able to exploit the sensitivity of Loupas' estimator in detecting small displacements while side-stepping the issue of phase-wrapping that becomes an even greater issue at higher frequencies. Maximizing the sensitivity and accuracy of estimation algorithms is one means of minimizing the amount of energy that needs to be delivered to tissue.

The adaptive estimation algorithm presented here is unique in that it selects the appropriate estimator based on the properties of the estimators and the image statistics. It exploits the fact that the performance of displacement estimators depends on the conditions under which they operate and that no single estimator is likely to achieve good performance over the full range of conditions typically encountered. It is able to compensate for errors in one estimator by switching to the alternate estimator. For example, if the displacement is larger than the phase-wrapping threshold, then the NXcorr estimate is used in place of the erroneous Loupas estimate. Since the estimator properties that govern this switching are pre-calculated and stored, the overall added computation time for steps specific to the adaptive algorithm is minimal. For the adaptive algorithm, the total computation time was found to be 2.2 hours for a data set containing 1528 axial points and 512 lines. It was found that approximately 98.6% of the total computation time was spent calculating the NXcorr estimate, less than 0.1% of the time was spent calculating Loupas' estimate, and 1.4% of the time was spent on steps specific to the adaptive algorithm.

Although the adaptive estimator is able to circumvent errors in one estimator by using another estimator, it is still possible that both Loupas' estimator and NXcorr might

simultaneously provide incorrect estimates. This situation might occur most often when the displacement is larger than the phase-wrapping threshold and NXcorr experiences a peak-hopping error. If this occurred it would be difficult to recover a good estimate of the true displacement using the current adaptive approach. In this case, however, the adaptive algorithm should have the same performance as either Loupas' estimator or NXcorr individually. In this situation, previous studies have shown that it might still be possible to achieve a good estimate of the strain by applying techniques like Kalman filtering [72].

2.4 CONCLUSIONS

We showed that when the displacement magnitude induced by thermal strain imaging was $>\lambda/8$ and the electronic system SNR was >25.5 dB, the displacement estimate obtained from normalized cross-correlation was less biased than the estimate found using Loupas' estimator. On the other hand, when the displacement magnitude was $\leq\lambda/4$ and the electronic system SNR was ≤25.5 dB, Loupas' estimator had less variance than normalized cross-correlation. We also demonstrated the feasibility of applying these results to create an adaptive displacement estimation algorithm and showed using Field II simulations that this algorithm resulted in strain reconstructions with improved strain SNR and spatial accuracy. The adaptive algorithm was also applied to thermal strain imaging of an *ex-vivo* human amputation sample with comparable results.

2.5 ACKNOWLEDGEMENTS

This work was supported by NIH grants 5R01HL098320 (PI: Kim). The small animal imaging US scanner was supported by 1S10RR027383 (PI: Kim). Student training was supported by NIH training grant 5T32HL076124 (PI: Shroff). The authors would like to thank Andrew Needles (FUJIFILM, Visualsonics Inc.) for providing technical details about the MS250 ultrasound probe for the simulations.

3.0 MULTI-FOCI BEAMFORMING FOR SIMULTANEOUS ACOUSTIC RADIATION FORCE IMPULSE AND THERMAL STRAIN IMAGING

3.1 INTRODUCTION

Data in Chapter 2.0 were acquired using a high efficiency heating array coupled with a high frequency imaging probe [36], [73]. Although signal processing changes improved TSI image quality for this system, there were a number of fundamental challenges that hampered clinical translation using this system configuration. First, the system used a series of geometrically focused heating elements to deliver energy to a small, fixed target region. Because this target region is relatively small and there is wide range of variation in human anatomy, it is quite likely that the target plaque might fall outside the chosen heating region. Second, separate heating elements would require dedicated system electronics and hardware that would require the development of entirely new ultrasound platforms and probes, resulting in a huge cost to companies as well as end-users. Additionally, the imaging center frequency was 21 MHz. At this frequency, ultrasound is highly attenuated by tissue and cannot achieve reasonable penetration in human subjects. Finally, separate heating elements would likely result in a larger, bulkier transducer that would interfere with ease of use and lead to increased risk for musculoskeletal pain and injury in sonographers [74]. For these reasons, a clinically viable TSI system would

need to utilize existing ultrasound hardware such that heating and imaging could be performed with the same ultrasound array.

Delay-and-sum (DAS) beamforming for ultrasound imaging was introduced as a means of image formation with the coming of the first multi-channel array transducers in the late 1960's and early 1970's [75]. Since then, DAS beamforming has become the staple for modern ultrasound systems. DAS beamforming is diagrammed in Figure 11 and is mathematically described by Equation 14.

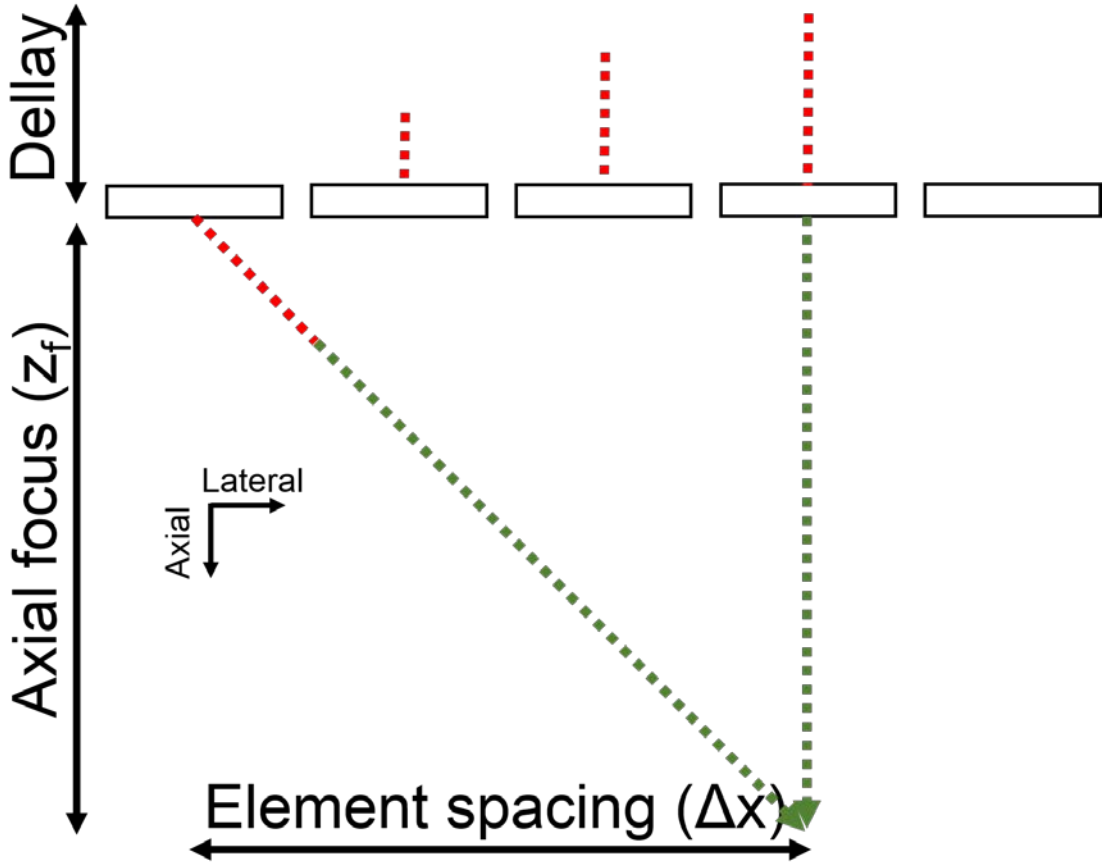

Figure 11: Diagram of delay-and-sum beamforming. Ultrasound waves from different elements need to travel different distances to reach the focal point. Delays, based on the focal point and element geometry are introduced so that the waves sum coherently at the focal point and focusing is achieved.

$$\Delta t_i = \frac{1}{c}\left(\sqrt{(x_N - x_0)^2 + \left(z_N - z_f\right)^2} - \sqrt{(x_i - x_0)^2 + \left(z_i - z_f\right)^2}\right)$$

Equation 14: Delay-and-sum beamformer. Time delay on the *i*th element, Δt_i; Speed of sound, c; Lateral position of element *i*, x_i; Lateral focal position, x_0; Axial position of element *i*, z_i; Axial focal depth, z_f. The *N*th element is the element that is furthest away from the focal point.

In clinical ultrasound imaging, the DAS beamformer is applied to both transmission of the ultrasound wave and reception of the backscattered echoes. During transmission, the user specifies a focal depth of interest. During reception, z_f is typically allowed to vary with depth and, as a result, the received echoes are dynamically focused across the entire image.

Overall, DAS generates an electronic lens that is analogous to focusing achieved in optics using a physical lens. DAS beamforming brings the far field into the focal plane and achieves diffraction limited focusing at the chosen focal depth. As a result, it can be shown with Fraunhofer diffraction theory that lateral beam profile in the focal plane is approximately equal to the Fourier transform of the aperture. For linear arrays, the lateral beamwidth and depth of field can be approximated using Equation 15 and Equation 16.

$$BW = \lambda \frac{z_f}{D} = \lambda \cdot (F/\#)$$

Equation 15: The lateral beamwidth (BW) for a DAS focused beam. Wavelength, λ; Axial focal depth, z_f; Aperture width, D; F-number, $F/\#$.

$$DOF = 7\lambda\left(\frac{z_f}{D}\right)^2 = 7\lambda \cdot (F/\#)^2$$

Equation 16: The depth of field (DOF) for a DAS focused beam. Wavelength, λ; Axial focal depth, z_f; Aperture width, D; F-number, $F/\#$.

The mathematical simplicity and theoretical elegance of DAS beamforming has likely been a key factor in the widespread dissemination of DAS beamformers in modern ultrasound. One recently popularized variant of this traditional imaging scheme is known as plane wave imaging (PWI). PWI utilizes an unfocused transmit beam. The backscattered echoes are beamformed using traditional DAS beamforming. This approach dramatically increases the frame rate at the cost of imaging resolution and contrast [76], [77]. Unfortunately, DAS beamforming is poorly suited for TSI heating because the goal of DAS beamforming is to concentrate the majority of the ultrasound energy into a diffraction limited spot. This would effectively limits the field of view of the TSI image to a single spot. The PWI transmit is also unsuitable because the unfocused beam is rapidly attenuated in tissue and cannot achieve heating at reasonable depths.

A heating field for TSI would be broad both laterally and axially, concentrate ultrasound energy within the target region, and have a homogeneous pressure distribution within the target region. Several authors have investigated alternative beamforming approaches in order to generate heating beams or arbitrarily shaped beams [78]–[80]. These methods have typically relied on solving the inverse problem for a target beam profile. Ultrasound arrays typically have between 64 and 256 elements. The user can control the delay and amplitude for each element. However, a target beam profile can have more than 1E5 field points. Because there are only 128 to 512 independent variables it is easy for the user to specify impossible target fields. Alternatively, sacrificing the resolution of the target field can lead to ill-posed problems or the generation of inhomogeneous heating beams.

ARFI imaging has been similarly limited by DAS beamforming. Traditionally, ARFI imaging push beams have utilized DAS beamforming to push a small volume of tissue. The mechanical response of this volume is tracked using traditional DAS beamforming methods. This process is repeated at each lateral position in order to build a full ARFI image. However, because the mechanical response must be tracked for several milliseconds at each lateral location, the overall ARFI imaging frame rate is slow (1-10 Hz). A broad pushing beam could be used to push a large volume. The mechanical response of this overall volume could then be monitored using PWI which would increase the frame rate by more than an order of magnitude.

An alternative beamforming approach that our lab has pioneered is the use of two temporally interleaved multi-foci beams for TSI heating [81], [82]. Both the tissue heating for TSI and the generation of acoustic radiation force (ARF) depend on tissue absorption of ultrasound. Thus, the same beam could be used for both ARFI pushes and TSI heating. Furthermore, the ARFI mechanical response decays over a period of 1-10 ms whereas tissue heating develops over the course of several hundreds of milliseconds and decays over the course of seconds. Because of this difference in temporal responses, the ARFI and the TSI response to a series of multi-foci pushes could both be monitored simultaneously. In this chapter, we explore a means of improving this multi-foci beamforming approach using simulation. Additionally, we demonstrate the feasibility of using these beams for both TSI and ARFI imaging using phantoms and excised tissue samples.

3.2 MATERIALS AND METHODS

3.2.1 Improved Temporally Interleaved Multi-foci Beamforming

Previously, we described a method using two temporally interleaved, multi-foci beams to generate a homogeneous beam field over a large region using a single linear array transducer [81]. This approach is illustrated in Figure 12.

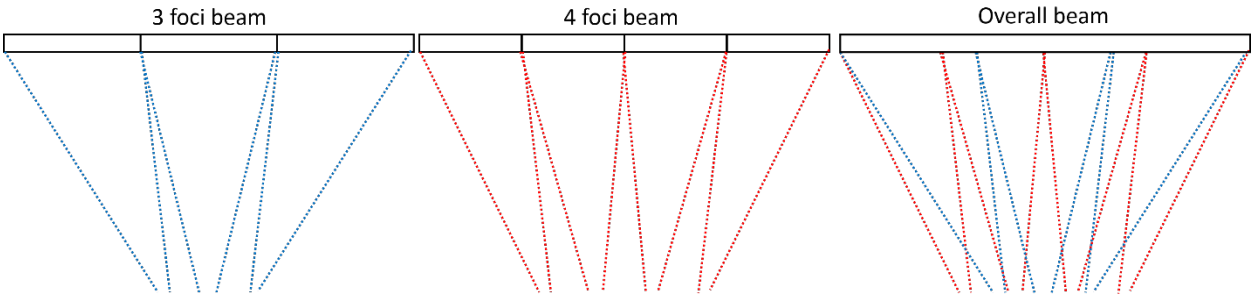

Figure 12: Diagram for the original multi-foci beamforming concept. The aperture is subdivided into sub-apertures. Each sub-aperture has a different focus. Rapid, temporal interleaving of a 3-foci beam and a 4-foci beam generates a broad, homogeneous overall beam.

The first multi-foci beam divides the transducer aperture into three sub-apertures. Each sub-aperture has a unique lateral focus which is achieved using DAS beamforming. The second multi-foci beam divides the transducer aperture into four sub-apertures with four distinct lateral foci. Because DAS beamforming is used to generate the sub-beams within each multi-foci beam, the user is able to reliably control the sub-beam positioning by adjusting the delay profile. Thermal and mechanical perturbations in tissue propagate on a time scale that is orders of magnitude slower than ultrasound propagation [70], [83]. Thus, the two multi-foci beams can be

rapidly interleaved in time in order to generate heating and pushing beams whose shape is equal to the summation of the two individual multi-foci beams.

In order to improve the homogeneity and efficiency of the beam, we modified this approach so that the sub-apertures had unique lateral and axial foci. The original beam generated peak heating deep to the region of interest. Additionally, even though the main lobe of each sub-beam had a predictable shape, constructive and destructive interference of the side-lobes of a sub-beam interfered with the main lobes of adjacent sub-beams. As a result, each multi-foci beam was not simply the sum of the individual sub-beams.

In order to optimize the position of the foci for each sub-beam, we iteratively simulated the beam pattern of individual sub-beams using different foci positions. This process is shown graphically in Figure 13. First, the focus of the central sub-beam in the three foci beam was fixed to correspond to the middle of the target region. We then designated the central two sub-beams in the four foci beam as the “test beams.” We used Field II to simulate the beam pattern of the test beams for a range of axial and lateral foci within the target region. For each simulated test beam, the overall beam generated from the sum of the test beams and the fixed sub-beam was calculated. The best overall beam was chosen using quantitative metrics and subjective impressions of the amplitude, homogeneity, and area of the overall beam. Then, the axial and lateral foci for the test beams corresponding to best overall beam were also fixed. At this point, three of the seven sub-beams were fixed. Next, the remaining two sub-beams in the three foci beam were chosen to be the test beams. The search and assessment of the overall beam was repeated for these test beams to yield the next set of fixed beams. The final two remaining sub-beams in the four foci beam were chosen to be the test beams and the process was repeated to yield the complete delay profiles.

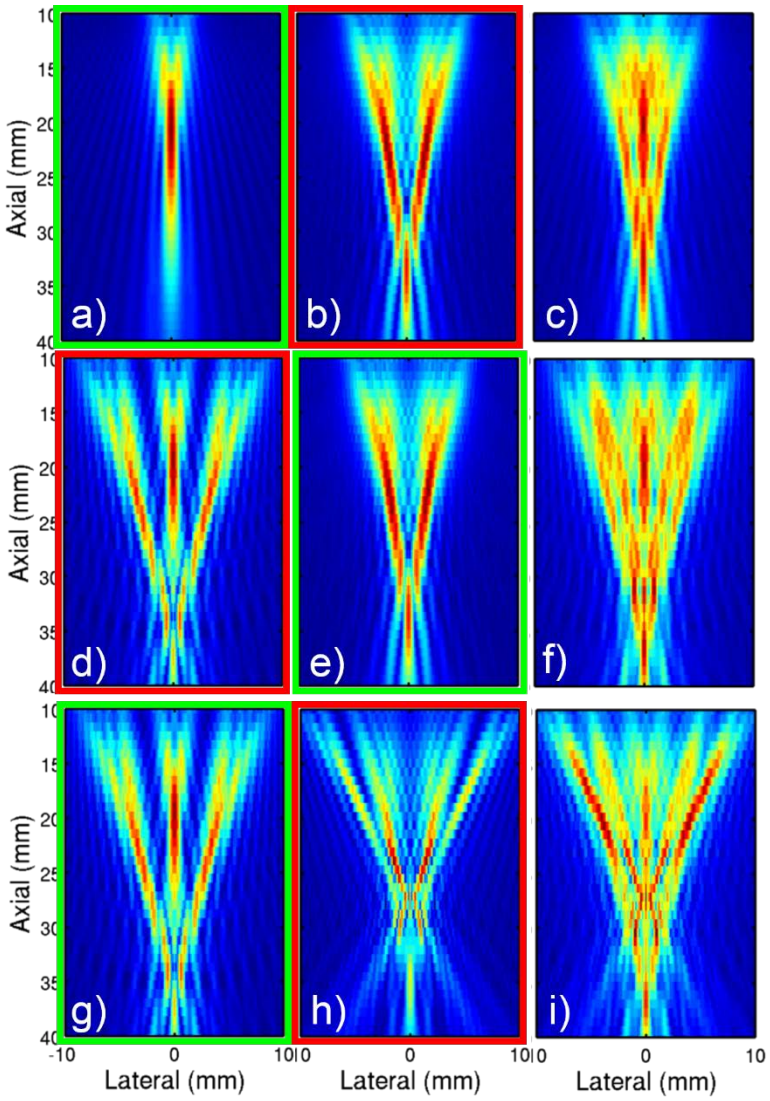

Figure 13: Iterative optimization for multi-foci beamforming. The 1st column of images are the beams generated from the 3 foci beam. The 2nd column are the beams generated from the 4 foci beam. The 3rd column is the overall beam generated from the sum of the two multi-foci beams. The rows show successive iterations after new beams are added. The fixed beams are outlined in green in a), e), and g). The test beams are outlined in red in b), d) and h).

The Field II sampling rate was set at 200 MHz and the attenuation coefficient, α, was set to 0.5 dB/cm/MHz. Multi-foci beams were simulated using three different transducers: 1) L22-14v (Verasonics Inc., Kirkland, WA), 2) ATL L7-4 (Philips Healthcare, Amsterdam, Netherlands), and the 3) ATL C4-2 (Philips Healthcare, Amsterdam, Netherlands). The parameters for these probes are shown in Table 1.

Table 1: Probe Parameters for the Field II Simulation

Probe Name	**L22-14v**	**L7-4**	**C4-2**
Pitch (mm)	0.100	0.298	0.421
Kerf (mm)	0.002	0.048	0.05
Height (mm)	16.0	7.0	13.0
Convex radius (mm)	-	-	41.219
Elevation Focus (mm)	8.0	25.0	70.0
Transmit Frequency (MHz)	15.0	4.20	2.71
# of elements (total)	128	128	128
# of elements (3 foci beam)	34-30-34	33-30-33	42-44-42
# of elements (4 foci beam)	32-32-32-32	31-33-33-31	20-44-44-20

3.2.2 Combined ARFI-TSI Imaging Sequence

The multi-foci beams designed for the L7-4 transducer were implemented onto a Verasonics Vantage (Kirkland, WA) system which drove an ATL L7-4 trasnducer. A combined ARFI-TSI pulse sequence utilizing the multi-foci beams is shown in Figure 14.

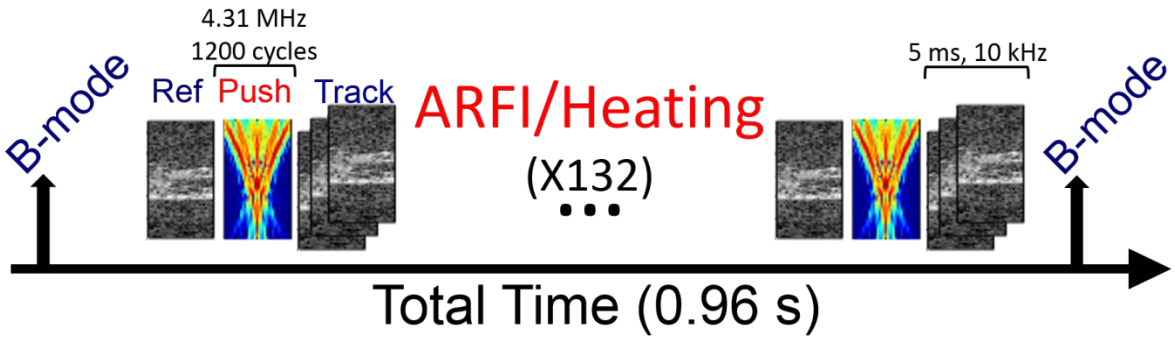

Figure 14: Combined ARFI-TSI pulse sequence.

First, a standard B-mode image with 79 lines spaced 0.298 mm apart was acquired for TSI. An F/2 configuration was used for transmit with a 30 mm focus and a F/1.5 configuration was used for dynamic receive. A transmit frequency of 6.25 MHz and a pulse length of two cycles was used for all imaging pulses. During ARFI acquisition the tissue response to the multi-foci push was tracked for 5 ms using PWI with a pulse repetition frequency of 10 kHz and a F/1 dynamic receive configuration. The multi-foci push had 1200 total cycles transmitted at 4.31 MHz. The three and four foci beams were interleaved in 100 cycle bursts. This ARFI sequence was repeated 132 times in 0.96 sec. The overall duty cycle during the heating or ARFI phase was ~4.5%. At the end of the ARFI frames, another standard B-mode frame was acquired for TSI tracking. The probe was driven at 20 V for all transmit events in the sequence. Backscattered radiofrequency data were sampled at 41.67 MHz and saved for offline processing.

For TSI, the displacement from the reference frame to the post-heating frame was tracked using Loupas' estimator with a 2.2λ tracking kernel [51]. After displacement estimation, the displacement data were filtered with a 0.46 X 1.19 mm (axial X lateral) median filter and a 2 kHz axial low pass filter. A 4 mm 2^{o} Savitzky-Golay filter was applied in the axial direction to calculate the thermal strain from the displacement estimate. For ARFI imaging, Loupas'

estimator with a 3λ kernel was used to track the displacement. After displacement estimation, the ARFI displacement data were filtered with a 0.46 X 0.89 mm (axial X lateral) median filter and a 2 kHz temporal low pass filter.

3.2.3 Homogeneous Phantom

A homogeneous gelatin phantom was fabricated in order to demonstrate successful implementation of the multi-foci beamforming as well as simultaneous TSI-ARFI imaging. In order to fabricate the phantom, 35 g (7% g/mL) of gelatin from porcine skin (Sigma Aldrich Co., MO, USA) was added to 500 mL of cold water and allowed to mix homogeneously. The solution was heated until it reached approximately 65^{o}C or became clear. Then, 35 g (7% g/mL) of cellulose (Sigma Aldrich Co., MO, USA) was added and allowed to thoroughly mix. The mixture was poured into a pre-chilled mold in a -20^{o}C freezer. The phantom was allowed to cure at this temperature for an additional hour. Afterwards, it was allowed to come to room temperature and imaged using the aforementioned system. The ultrasound probe was held with a clamp and coupled to the phantom using degassed water. The combined ARFI-TSI sequence was used to image five distinct locations in the phantom corresponding to unique speckle realizations.

3.2.4 Adipose Phantom

A gelatin phantom with an embedded layer of subcutaneous fat was fabricated. The fat was obtained with University of Pittsburgh Internal Review Board (IRB) exemption because it met the criteria for medical waste. In order to fabricate the phantom, a layer of gelatin was first mixed and poured using a variation of the recipe in 3.2.3. The phantom was constructed with 7%

gelatin (g/mL) and 7% cellulose (g/mL). After the first layer of gelatin had almost set, the excised subcutaneous fat was layered over the gelatin so that it was approximately 5 – 10 mm thick. Then, the remainder of the gelatin was poured on top of the fat to form a layer that was approximately 20 mm thick and allowed to set. The ultrasound probe was held with a clamp and coupled to the phantom using degassed water.

3.3 RESULTS & DISCUSSION

A set of multi-foci beams was generated for the L7-4 transducer using the iterative optimization approach detailed in 3.2.1. In Figure 15, the focusing configuration and the resultant beam fields for the new approach are compared to the multi-foci approach from [81]. With the original approach, only the lateral foci of the sub-beams were allowed to vary. This produced a broad and relatively homogeneous beam in the target region (20-30 mm). However, this configuration also generated geometric alignment of the sub-beams which resulted in an undesirable focusing effect deep to the target region. Inadvertent deposition of energy in this region is primarily undesirable because it means that energy which could have been used to heat or push tissue is instead concentrated in an undesired region. Also, depending on the transmitted pressure, it might represent a safety concern. In comparison, the multi-foci beam generated with variable axial and lateral foci had a more homogeneous pressure distribution due to the arrangement of the foci. When the beams were compared quantitatively, the original multi-foci beam had an area of 29.1 mm^2 within 6 dB of the peak pressure. The new beam had an area of 102.1 mm^2 within 6 dB of the peak pressure.

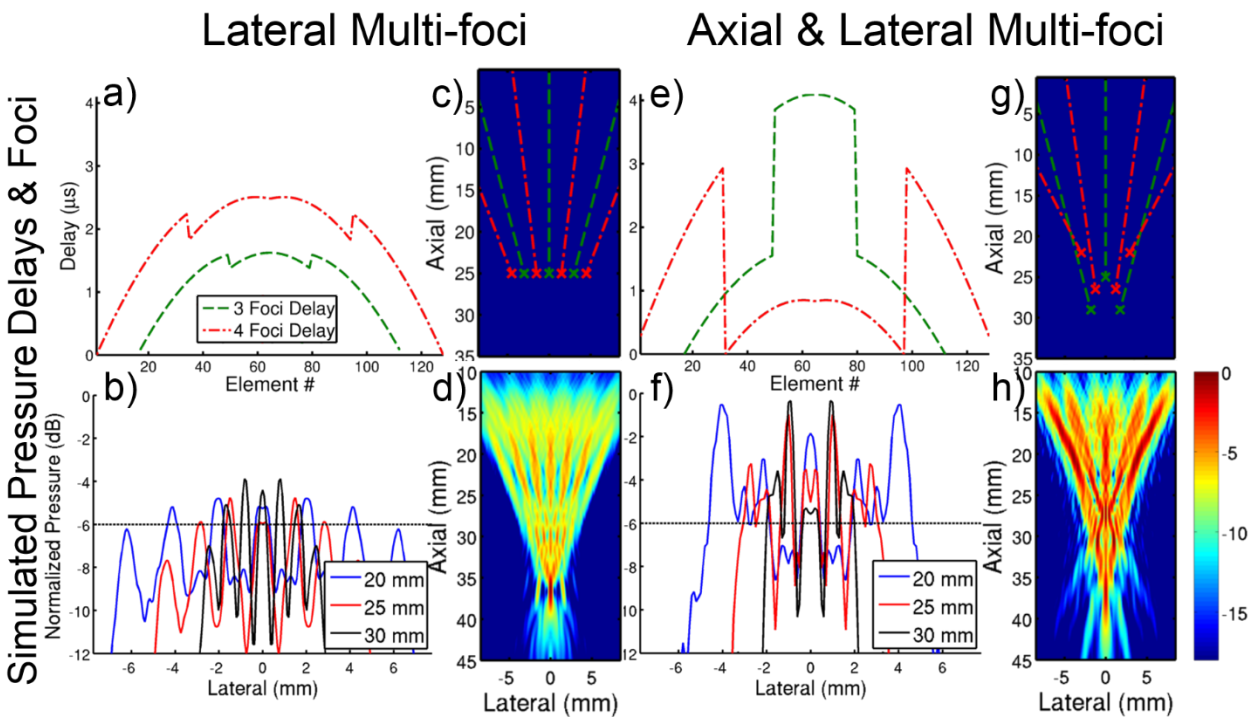

Figure 15: A comparison of multi-foci beamforming with variable lateral foci versus variable axial and lateral foci. Panels a), b), c), and d) show the delay profile, simulated lateral pressure profiles (dB), focal positions, and simulated pressure fields (dB) using the previously developed approach [81]. Panels e), f), g), and h) show the same data using the iterative approach with variable lateral and axial foci. In panels a), c), e), and g), data are shown in red and green for the 3 and 4-foci beams respectively.

Given the success of the novel multi-foci approach, we sought to investigate how broadly applicable this approach was for different target depths as well as different transducer geometries. We found that the most important factor for achieving the desired target depth was the transmit frequency of the beam (data not shown). This is likely because the multi-foci approach is, in many ways, analogous to a weakly focused or unfocused transducer. For unfocused transducers, the focal region is determined by the aperture size as well as the frequency of the transducer [84]. Additionally, the peak pressure for these beams will depend on the attenuation of the medium.

We sought to apply the multi-foci beamforming approach to generate beams targeting shallow (1-10 mm) and deep regions (>30 mm). Because ultrasound transducers typically have a

limited bandwidth, we used the L22-14v for the shallow target region and the C4-2 for the deep target region. The results of the novel multi-foci approach for these two target regions are show in Figure 16.

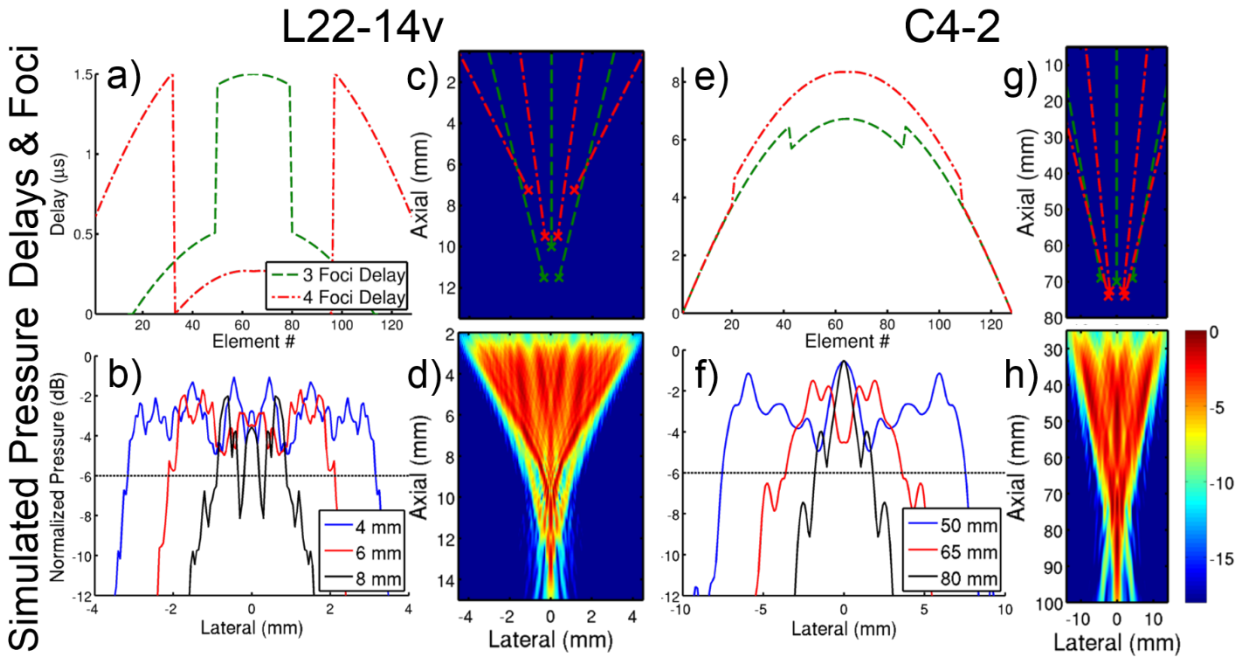

Figure 16: A comparison of multi-foci beamforming using the L22-14v and C4-2 transducers. Panels a), b), c), and d) show the delay profile, simulated lateral pressure profiles (dB), focal positions, and simulated pressure fields (dB) For the L22-14v. Panels e), f), g), and h) show the same data for the C4-2. Note that the axial and lateral scales are different in panels d) and h).

These data show that the multi-foci approach is able to produce broad, homogeneous beams at both shallow and deep depths. The L22-14v produces a beam that is centered on 6 mm and ranges from 2-10 mm whereas the C4-2 produces a beam that is centered on approximately 60 mm and ranges from 30 – 90 mm. Additionally, it demonstrates that the multi-foci approach can be used with curvilinear arrays as well as linear arrays. These data also show that the width of the beam depends on the aperture size. The L22-14v has a small aperture size and produces a

narrower beam relative to the beam produced by the C4-2. While this approach could theoretically be applied to cardiac phased arrays, it would likely have a limited width due to the narrow aperture sizes for most cardiac phased arrays. However, beam steering, which was not explored in this study, might be able to be combined with our multi-foci approach to provide swept multi-foci beams for these phased arrays.

The multi-foci beams for the L22-14v and C4-2 are qualitatively more homogeneous compared to the beam for the L7-4. This is likely due to a number of a reasons. First, as was noted in 3.2.1, this optimization approach is greedy and requires manual, subjective evaluation of the beams. These two factors mean that is unlikely that optimization will achieve a global maximum. In other words, there could be more optimal beams that exist. The multi-foci beam for the L7-4 was designed first, so it was unclear whether it was possible to achieve a more homogeneous beam or what steps in the optimization could be modified to achieve a more homogeneous beam.

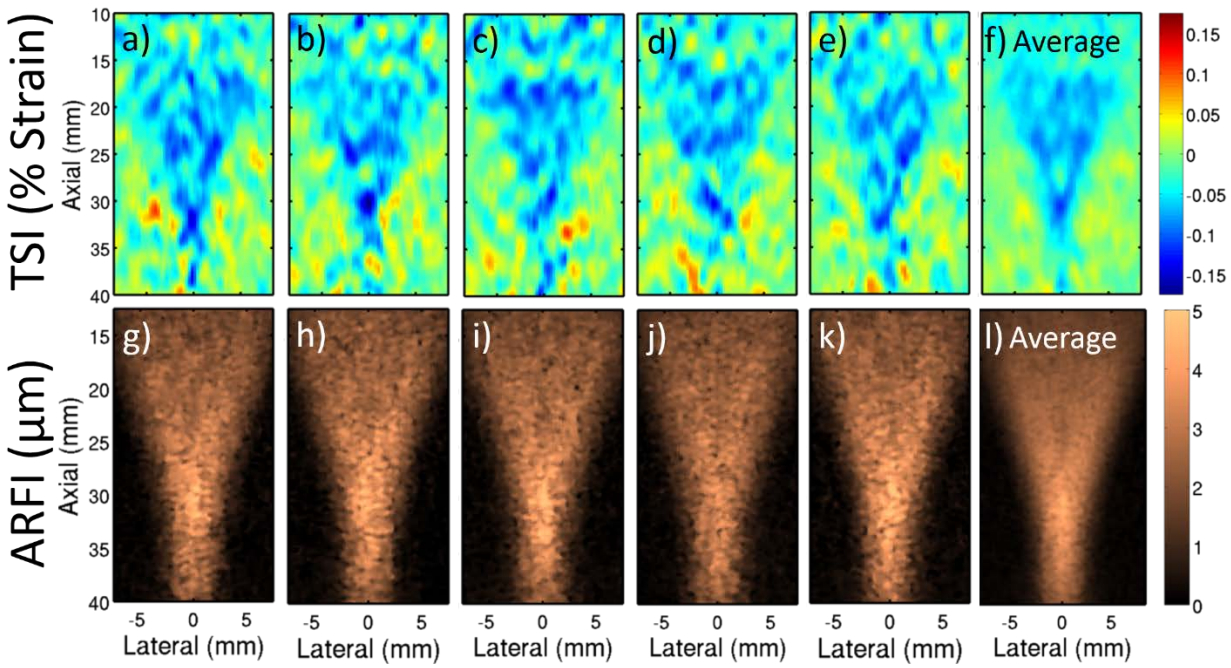

Figure 17: Combined TSI-ARFI imaging in a homogenous gelatin phantom. a) – e) show TSI at 5 different locations within the phantom. f) is the average thermal strain across those 5 positions. g) – k) show ARFI imaging at 5 different locations within the phantom. l) is the average displacement across those 5 positions.

ARFI and TSI data in Figure 17 were collected simultaneously using the sequence described in 3.2.2 at 5 different locations in the phantom. It demonstrates that the multi-foci beam can be used for both ARFI pushing and TSI heating. The figure shows that the majority of the observed inhomogeneities are due to variations in the speckle pattern. The average strain and displacement are homogeneous and do not contain the high frequency spatial variation that is present in the pushing/heating beam. For TSI, this is likely due to the effects of heat conduction smoothing out the heating profile. For ARFI imaging, it is likely due to a combination of the viscosity of the phantom as well as degraded tracking from PWI.

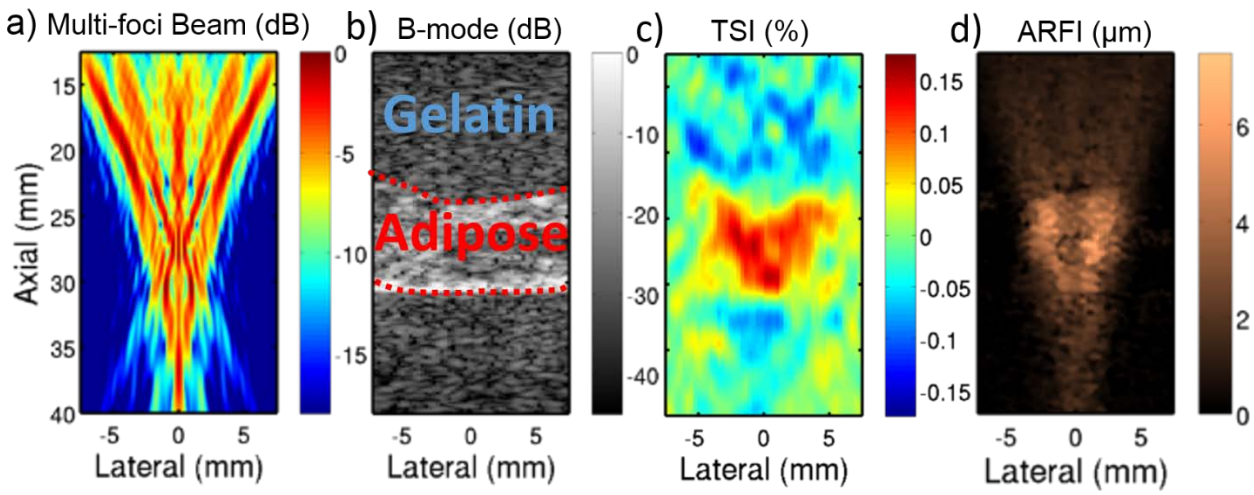

Figure 18: Combined TSI/ARFI imaging in an adipose phantom. a) The Field II simulated multi-foci push beam. b) The B-mode image shows fat embedded between two gelatin layers. c) TSI image of the phantom. d) ARFI of the phantom.

Figure 18 shows the combined sequence applied to the liposuction phantom from 3.2.4. The beam is shown with the TSI and ARFI images to show that the heating and pushing pattern clearly reflect the overall shape of the beam. In the TSI image, it can be seen that the gelatin has negative strain and that the layer of adipose tissue has positive strain. Additionally, the heating pattern within the adipose layer appears to be slightly larger than the width of the beam. This is likely due to the high thermal conductivity of the adipose which promotes conduction of heat. In this case, the gradient in signal at the edge of the beam in the fat layer is not due to differing concentrations of fat, but rather a gradient in heat.

For the ARFI image, there is also good contrast between the stiff gelatin and the soft adipose layer. Interestingly, a thin vertical layer in the middle of the adipose layer has low displacement. This vertical layer was not present in any of the images taken in homogeneous phantom suggesting that it is the result of the structure of the layer as opposed to error in the tracking. This low displacing inclusion could be the result of either a locally non-absorbing region or a stiff inclusion. However, the TSI image shows relatively homogeneous, positive

strain in this same region which increases the likelihood that the inclusion is stiff. This demonstrates the utility of combined compositional and mechanical imaging. Atherosclerotic plaque is typically quite heterogeneous in composition and both imaging modalities add unique information about the plaque status.

3.4 CONCLUSIONS

In this chapter, we demonstrated that an iterative semi-manual optimization approach could be used to develop improved temporally interleaved multi-foci beams. These novel beams have improved homogeneity as compared to the previous iteration of multi-foci beams. This is the result of allowing the sub-beams to have variable axial as well as lateral foci. We showed that this approach could be used to develop beams with target regions at different depths and for different transducers. Additionally, we showed that the multi-foci beams could be used for simultaneous TSI and high frame rate ARFI imaging. We demonstrated that the beams produced homogeneous pushing and heating profiles in a homogenous phantom. Additionally, we showed that they provided good mechanical and compositional contrast in a layered gelatin and adipose phantom.

3.5 ACKNOWLEDGEMENTS

This work was supported by NIH grant 5R01HL098320 (PI: Kim). Student training was supported by NIH training grant 5T32HL076124 (PI: Shroff). I would like to thank Dr. Man Nguyen for invaluable feedback and constructive conversations regarding this work.

4.0 IMPROVED ESTIMATION OF THERMAL STRAIN USING PULSE INVERSION HARMONIC IMAGING

The work presented in this chapter was published in Ultrasound in Medicine and Biology, vol. 42, no. 5, pp. 1182–1192, May 2016.

4.1 INTRODUCTION

Ultrasound thermal strain imaging (TSI), which has also been referred to as temporal strain imaging, is a non-invasive imaging technology that relies on the temperature dependence of the speed of sound as a means of differentiating fatty tissue from water-based tissue. In water-based tissues, the speed of sound increases with increasing temperature and in lipid-based tissues, the speed of sound decreases with increasing temperature. This relationship is quantified with the material constant β, which has units of %/^{o}C and is a measure of the percentage change in sound speed per unit change in temperature [43]. For water-based tissues like normal liver or muscle, β has been found to be between 0.06 and 0.13 %/^{o}C. For lipid-based tissues like abdominal fat, β is typically between -0.13 and -0.20 %/^{o}C [29]. Clinically, TSI development is focused on non-invasive detection of fatty liver disease and identification of lipids in atherosclerotic plaques [69], [85].

In TSI, a reference ultrasound image is acquired. Next, custom beamforming and pulse sequences are used to generate a high intensity ultrasound beam that will homogeneously increase the temperature in the target region by <2ºC. The temperature rise is the result of absorption of the propagating ultrasound wave. After the heating sequence is completed, a post-heating ultrasound image is acquired. As a result of the change in the sound speed, there is an apparent displacement (time-shift), u, between received echoes in the reference and post-heating images. The derivative of this displacement in the ultrasound wave propagation (axial) direction is the "thermal (temporal) strain," $\frac{du}{dz}$, and is proportional to the change in sound speed. In water-based tissue, this strain is negative and the tissue appears to undergo relative compression. In lipid-based tissue, the strain is positive and the tissue appears to undergo relative expansion. For the small temperature changes utilized in TSI, the temperature induced mechanical strain resulting from volumetric tissue expansion is approximately an order of magnitude smaller than the apparent strain resulting from the change in sound speed and can typically be ignored [43]. Equation 1 is the governing equation for TSI where ΔT is the temperature change. In TSI, u is tracked by comparing the reference and post-heating images and $\frac{du}{dz}$ is calculated from the measured displacement.

Ultrasound non-invasive thermometry (NIT) is based on the same underlying physics as TSI but incorporates three major differences. First, NIT is typically used to assess temperature changes during high intensity focused ultrasound (HIFU) or radiofrequency (RF) ablation procedures which result in temperature changes on the range of 2ºC to >20ºC [86], [87]. In this temperature range, it is no longer acceptable to ignore thermally induced mechanical strains.

$$\frac{du}{dz} = (\alpha - \beta)\Delta T$$

Equation 17: Governing equation for TSI including thermal expansion. "Thermal" or "temporal" strain (derivative of displacement), $\frac{du}{dz}$; Coefficient of thermal expansion (%/ºC), α; Sound speed coefficient (%/ºC), β; Temperature change, ΔT.

As a result, the governing equation is modified to Equation 17. Finally, in NIT, the material constants are assumed to be known parameters. The temperature change is found by dividing the measured strain by the material constants.

Both TSI and NIT have been tested using *in vivo* animal models and *ex vivo* tissue preparations [34], [73], [85], [88]–[90]. For TSI, these studies have aimed at identifying the lipid rich core of atherosclerotic plaques or quantifying hepatic steatosis. The clinical applications of NIT are focused on monitoring of thermal ablation as well as theranostic approaches utilizing temperature-sensitive drug delivery vehicles. However, a number of challenges are present in human patients that are absent or less flagrant in small animal models. One major challenge is clutter-based degradation of image quality [91]. Clutter is a general term for noise that serves to decrease image contrast. One prominent source of clutter in patients is near-field reverberation. Near-field reverberation occurs because the propagating ultrasonic wave is reflected multiple times within superficial tissue layers (e.g. skin, subcutaneous fat). These multiple reflections corrupt echoes arriving from deeper tissue structures and appear as a haze in the ultrasound image [92]. One well-established method commonly used in clinics to reduce clutter is harmonic imaging. Harmonic imaging exploits the non-linear propagation of the fundamental wave and images the resulting second harmonic signal. The second harmonic signal is typically weak in the near-field and reaches its peak intensity in the focal zone which helps to mitigate near-field clutter artifacts [93].

Recently, groups have shown that harmonic imaging can not only be used to improve traditional B-mode images, but can also be used to improve ultrasound-based displacement tracking which serves as the basis for acoustic radiation force and shear wave imaging [94], [95]. Doherty et al found that pulse inversion harmonic imaging (PIHI) provided the greatest improvement to ultrasonically tracked displacements. In the pulse inversion technique, two 180^{o} phase-shifted (inverted) fundamental pulses are transmitted sequentially. Summation of the received signals from these pulses results in cancellation of the fundamental signal and amplification of the harmonic. Because TSI measures strain calculated from ultrasonically tracked apparent displacements, we hypothesized that PIHI could also be applied to improve estimation of apparent strains produced as result of temperature-induced changes in the speed of sound. In this study, we experimentally show that PIHI can be used to improve the quality of thermal (temporal) strain images using a variety of relevant imaging phantoms and *ex vivo* human tissue samples. Conventionally, NIT uses the same ultrasound tracking scheme as TSI. As such, we point out potential applications and parallels of this work to NIT when they are relevant.

4.2 MATERIALS AND METHODS

4.2.1 Ultrasound TSI Pulse Sequence

The pulse sequence and timing for the TSI sequence is diagrammed in Figure 19a. PIHI was incorporated into the imaging portions of the TSI pulse sequence using a research ultrasound platform with an external HIFU power supply (Vantage, Verasonics Inc, Kirkland, WA) using an

ATL L7-4 transducer (Philips Healthcare, Amsterdam, Netherlands) [93]. The -6 dB bandwidth of this transducer was measured to be 3.3 – 6.6 MHz. The overall sequence consists of imaging, followed by a heating phase, and ends with a post-heating imaging phase. There was a 35 ms pause between the first imaging phase and the beginning of the heating phase and a 500 μs pause between the end of the heating and the beginning of the final imaging phase. These pauses were inserted to allow time for data transfer and power supply switching.

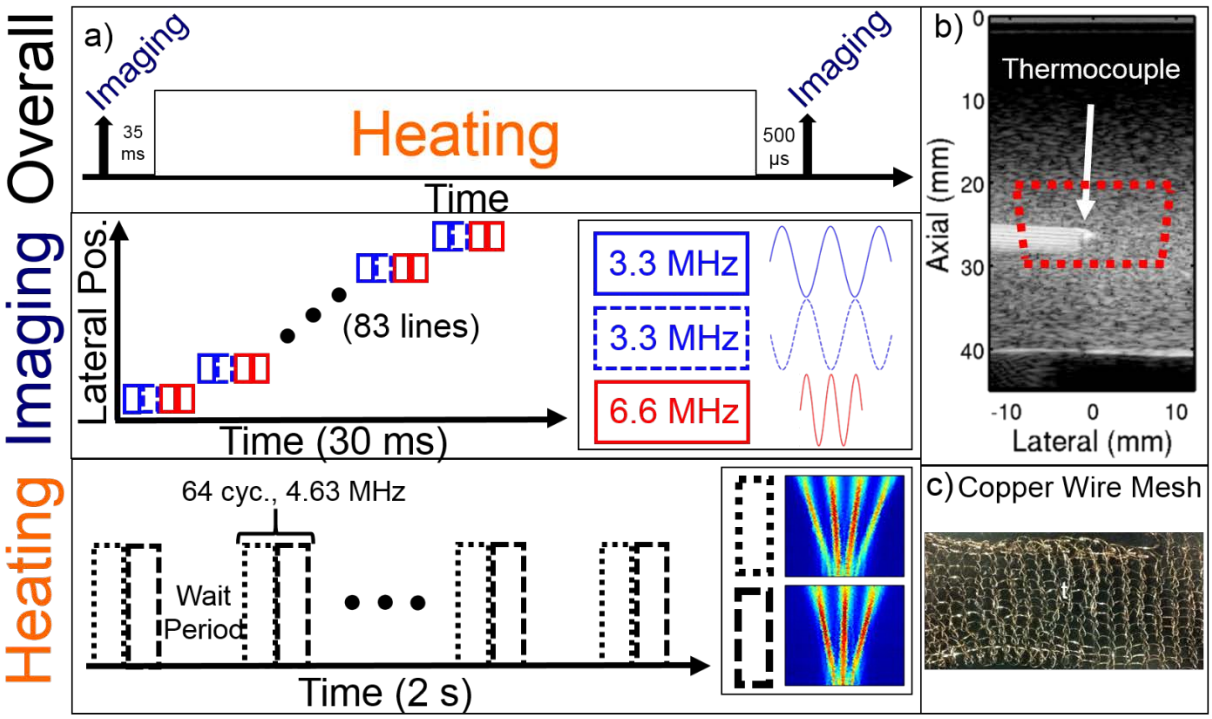

Figure 19: Schematic for TSI pulse sequence using PIHI, B-mode image showing thermocouple positioning, and a photographic image of the copper mesh. The overall TSI sequence, as well as individual pulse sequences for imaging and heating are shown in a). The duration of the heating portion of the sequence is fixed at 2 seconds and a variable length "wait period" is used to control the heating duty cycle. For temperature measurements, the tip of the thermocouple was placed at 25 mm axially and 0 mm laterally as shown in b). The red dashed lines designate the region used to calculate the SNR. A single layer of copper mesh is shown in c).

During imaging, the transducer was first excited with a 3.3 MHz pulse. RF backscattered echoes were received on 128 parallel channels at a sampling frequency of 41.7 MHz and saved for offline processing. This process was repeated for a 180^{o} phase-shifted (inverted) 3.3 MHZ excitation, and again for two 6.9 MHz excitations with the same phase. All excitations were 2.5 cycles long. It was found that by using excitations at 3.3 MHz and 6.9 MHz, the center frequency (f_c) of the received echoes was approximately 3.3 MHz and 6.6 MHz. This was likely due to the convolution of the excitation pulses with the impulse response of the transducer. This transmit/receive sequence was repeated at each of the 83 imaging lines and corresponded to an imaging time of approximately 30 ms. The spacing between lines was 0.298 mm. The f-number for both transmit and receive focusing was set to 1.97 in order to minimize beamforming errors due to changes in sound speed.

We previously described specialized beamforming utilizing two temporally interleaved beams with multiple lateral foci that could be used to achieve homogeneous heating in a trapezoidal region from 20 – 30 mm axially (Figure 19b) [81]. In this study, the heating sequence has been modified slightly in order to improve the overall efficiency. The excitation frequency was shifted to 4.6 MHz as a compromise between attenuation and transducer bandwidth. The first beam utilizes four lateral foci and is transmitted for 32 cycles. Immediately afterwards, a second beam utilizing three lateral foci is transmitted for 32 more cycles. The seven foci are spaced to provide a broad, homogeneous heating region. Finally, a variable length waiting period with no transmits is utilized. These three events repeat until the total heating duration is equal to two seconds (Figure 19a, “Heating”). Because the duration of the heating sequence is fixed at two seconds, the length of the waiting period determines the overall duty cycle during the heating period. Unless otherwise specified, the duty cycle was fixed at 5% and corresponded to a

wait time of 264 μs. The excitation amplitude used for heating was 15 V and corresponds to a peak negative pressure of approximately 2.3 MPa in degassed water which was measured using an ONDA HGL0200 bullet type hydrophone at the heating focus of 25 mm axially.

4.2.2 Offline Ultrasound TSI Signal Processing

3.3 MHz fundamental data was generated by *subtracting* the RF data from the first pair of phase-inverted 3.3 MHz transmits. PIHI data was generated by *summing* the RF data from the first pair of phase-inverted 3.3 MHz transmits. 6.6 MHz fundamental data was generated by *summing* the RF data from the pair of in-phase 6.6 MHz transmits. RF data were beamformed using delay-and-sum beamforming and Hilbert transformed in order to obtain IQ data. Apparent axial displacements between the reference and post-heating frame were calculated using Loupas' estimator with a kernel size equal to 1.5 wavelengths [51]. For all quantitative calculations, displacement data were median filtered with a 0.10 X 0.89 mm (axial X lateral) median filter and the apparent axial strain was calculated using a 2 mm 1^{st} order Savitzky-Golay filter. For display purposes, the strain was calculated using a 3 mm 1^{st} order Savitzky-Golay filter. In this study, TSI acquisition refers to both the ultrasound pulse sequence and these offline signal processing steps.

4.2.3 *In vitro* Gelatin-Castor Oil Phantom Experiments

Mixed gelatin-castor oil phantoms were fabricated in order to mimic fat-water mixtures that might be found in hepatic steatosis of heterogeneous atherosclerotic plaques. The phantom fabrication technique was modified from a recipe previously reported in the literature [96]. The

respective volumes of water and sulphonated castor oil (Spectrum Chemical , CA, USA) were first calculated in order to obtain a castor oil percentage ranging from 0 – 50% (vol/vol). Then, based off of the total volume, 5% (wt/vol) gelatin from porcine skin (Sigma Aldrich Co., MO, USA) and 2% (wt/vol) cellulose (Sigma Aldrich Co., MO, USA) were weighed. The percentages of gelatin and cellulose, which provide underlying structure and ultrasound scatterers respectively, were fixed for all phantoms in this study. The gelatin was added to cold water, allowed to mix, and then heated to approximately 65^{o}C or until the solution became clear. Then, the cellulose was added to the solution and allowed to thoroughly mix. Finally, castor oil was slowly added to the mixture in order to ensure homogeneous mixing. The mixture was allowed to cool while maintaining constant stirring. When the mixture approached approximately 35^{o}C, the mixture was poured into a pre-chilled plastic mold in a -20^{o}C freezer. The phantom was allowed to cure at this temperature for an additional hour. After the phantom cured, it was carefully removed from the plastic mold and placed on sound attenuating rubber for imaging. In this study, the sound speed of the phantoms were not modulated using n-propanol. The scatterer concentration used produced fully developed speckle in all phantoms. Throughout this study, degassed ultrasound gel was used to couple the transducer to the phantom and the transducer was held using a clamp.

A gelatin (0% castor oil) phantom was allowed to come to room temperature and TSI was performed with heating duty cycles ranging from 0.1 – 10% (11 total duty cycles). At each duty cycle, TSI was performed at 5 different locations within the phantom resulting in a total of 55 TSI measurements for the 0% castor oil phantom. Following imaging, one temperature measurement was obtained for each duty cycle using a Type T needle sheathed thermocouple (MT-23/5, Thermoworks, UT, USA) connected to a data logger (Quadtemp, Thermoworks, UT,

USA). The thermocouple was accurate to within ±0.1 ^{o}C and had a time constant of 25 ms. For all temperature measurements in this study, the tip of the thermocouple was placed at an axial depth of 25 mm and a lateral position of 0 mm (centered). The thermocouple was aligned as shown in Figure 19b in order to reduce temperature underestimation.

TSI was also performed on 6 more homogeneous gelatin-castor oil phantoms with castor oil concentrations from 0 – 50%. Imaging occurred immediately after the phantoms were removed from the freezer because phantoms with high castor oil concentrations were mechanically unstable at room temperature. TSI was performed at 5 different spatial locations in each phantom with and without clutter. Clutter was introduced by placing layers of copper wire mesh (Fly-Bye Bird Control Products, WA, USA) between the transducer face and the phantom [91]. A single layer of mesh has pore sizes of approximately 0.5 X 0.5 cm (Fig. 1c). The level of noise generated by the copper mesh was measured relative to an anechoic background and found to be 27.5 dB, 28.9 dB, and 31.6 dB for 2, 3, and 4 layers of mesh respectively. For the gelatin-castor oil phantoms, two layers of clutter were used. A total of 60 TSI measurements were made across 6 phantoms. The theoretical elevational beamwidth of the ultrasound heating beam was 1.01 mm at 4.6 MHz which made thermocouple measurements across different phantoms sensitive to elevational misalignment errors. In order to obtain a better temperature estimate, 5 temperature measurements with and without clutter were obtained for each castor oil concentration. Between temperature measurements, the ultrasound probe was raised, lowered, and re-aligned with the thermocouple. As a result, the variation in the temperature measurements incorporate error inherent to the thermocouple (<0.1^{o}C) as well as errors relating to the alignment of the ultrasound probe and thermocouple. A total of 60 temperature measurements were taken across 6 phantoms.

4.2.4 Liposuction Phantom

Liposuction fat was collected from a patient undergoing body contouring surgery for massive weight loss. University of Pittsburgh IRB exemption was obtained for the use of human tissues because they met criteria for medical waste. Following liposuction, fat was centrifuged at 1286g for 3 minutes in order to remove aqueous and oil layers from intact adipose tissue. A two layered phantom was constructed. Both layers were approximately 25 mm thick. The top layer was a gelatin layer and the bottom layer was fresh liposuction fat.

TSI was performed with 0, 2, and 4 layers of copper mesh. A motor-controlled translation stage was used to raise and lower the transducer so that clutter could be introduced without disturbing the imaging plane. In this manner, paired, cluttered and clutter-free images were obtained. An independent set of paired clutter-free images were obtained for 2 and 4 layers of clutter. This process was repeated at 5 spatial locations corresponding to a total of 20 TSI acquisitions.

4.2.5 *Ex vivo* Carotid Endarterectomy (CEA)

Informed consent to obtain a surgical specimen was granted by a 73 year old female asymptomatic patient with >70% carotid stenosis previously scheduled to undergo CEA surgery. During surgery, the atherosclerotic plaque, intimal, and some medial portions of the carotid artery were removed. This sample was retrieved and frozen at -80^{o}C with University of Pittsburgh IRB approval. At a later date, the sample was defrosted and embedded in a gelatin phantom.

TSI was performed and images were acquired every 0.5 – 1 mm along the short axis of the artery using the translation stage. Spatially matched imaging with and without clutter was performed using 0 and 3 layers of clutter. Following imaging, the CEA sample was carefully extracted from the gelatin and immersed in formalin. The sample was sectioned every 1 mm along the short axis and stained using Oil red O staining. B-mode ultrasound was compared to histology to find matching sections.

4.2.6 TSI Quality Metrics and Statistical Analysis

Three metrics were used to evaluate the quality of TSI images in this study. First, the experimentally measured value for β was calculated using Equation 18. When multiple temperature measurements were available, this error was propagated into the final calculated value of β_{exp}.

$$\beta_{exp} = \frac{1}{\Delta T}\frac{du}{dz}$$

Equation 18: Experimental calculation for sound speed coefficient. Experimentally calculated "thermal" or "temporal" strain (derivative of displacement), $\frac{du}{dz}$; Temperature change, ΔT.

When multiple temperature measurements were not available, the error was assumed to be 27% which is experimentally measured variation for a gelatin (0% castor oil) phantom heated using a 5% duty cycle. This metric provides a temperature-normalized measure of the relative biases of each TSI tracking mode. In addition, it is an important parameter for NIT measurements because it must to be known in order to calculate the absolute temperature change.

Homogeneous regions, were evaluated using signal-to-noise ratio (SNR) which was defined using Equation 19. For inhomogeneous regions, the contrast-to-noise ratio (CNR) was used to measure image contrast and overall image quality and is defined in Equation 20.

$$\boldsymbol{SNR = \frac{|\mu|}{\sigma}}$$

Equation 19: Signal-to-noise ratio for a homogeneous region. Mean strain, μ, and standard deviation of strain σ within the red dashed area in Figure 19b.

$$CNR = \frac{\mu_{lipid} - \mu_{water}}{\sqrt{\sigma_{lipid}^2 + \sigma_{water}^2}}.$$

Equation 20: Contrast-to-noise ratio. Mean apparent strain within the lipid, μ_{lipid}, and water-based regions, μ_{water}; The standard deviation of the apparent strain within the lipid, σ_{lipid}, and water-based regions, σ_{water}.

The percent true and false positive areas were also measured. The percent true positive area was the percentage area with positive strain greater than 0.1% strain within a known *lipid region*. Conversely, the percent false positive area was the percentage area with positive strain greater than 0.1% strain within a known water-based (gelatin) region. The 0.1% threshold was chosen in order to prevent small, unreliable strains from influencing the calculation.

A one-tailed, paired t-test was used to evaluate statistical differences. The difference between PIHI and 6.6 MHz tracking and between PIHI and 3.3 MHz tracking was evaluated. For the liposuction phantom, differences in the strain estimates before and after addition of clutter were also evaluated. Thus, a maximum of three comparisons were used in order to minimize the probability of type I error. A paired t-test was used because all three tracking methods were

implemented within a single pulse sequence such that the temporal and spatial variation in the targets was negligible. In the case of the liposuction phantom, a mechanical translation stage was used to ensure spatially matched images before and after the addition of clutter. A one-tailed test was used because the goal was only to test the hypothesis of whether PIHI tracking improved strain estimates as compared to 6.6 MHz and 3.3 MHz tracking. In all cases, when $p < 0.05$, differences were considered significant. MATLAB R2014a (MathWorks Inc., MA, USA) was used for all statistical analyses.

4.3 RESULTS & DISCUSSION

4.3.1 Homogeneous Gelatin Phantom Experiment

Figure 20 shows the results for the homogeneous gelatin (0% castor oil) phantom imaged using TSI. The heating duty cycle was varied from 0.1 – 10% which produced monotonically increasing ΔT on the range of <0.10 – 0.78ºC. A single temperature measurement was taken for each duty cycle in order to avoid potential damage to the transducer at higher duty cycles. Figure 20a shows β as a function of ΔT. We observe that β converges to a value of approximately 0.13 %/ºC for ΔT > 0.26ºC (4% duty cycle). Although β converged to a smaller value for fundamental as compared to PIHI tracking, the difference was not statistically different. Prior studies using ultrasound tracking simulations have shown that a 5-10% bias in displacement can be expected in the presence of stationary clutter or lower tracking transmit frequencies [53], [70]. The reason statistically significant bias was not reproduced in this study was likely the result of uncertainty in the thermocouple measurements. In the context of the literature, these data suggest

that if a large enough region is chosen, a wide range of tracking frequencies will provide estimates of the apparent strain that agree within 5-10% of each other.

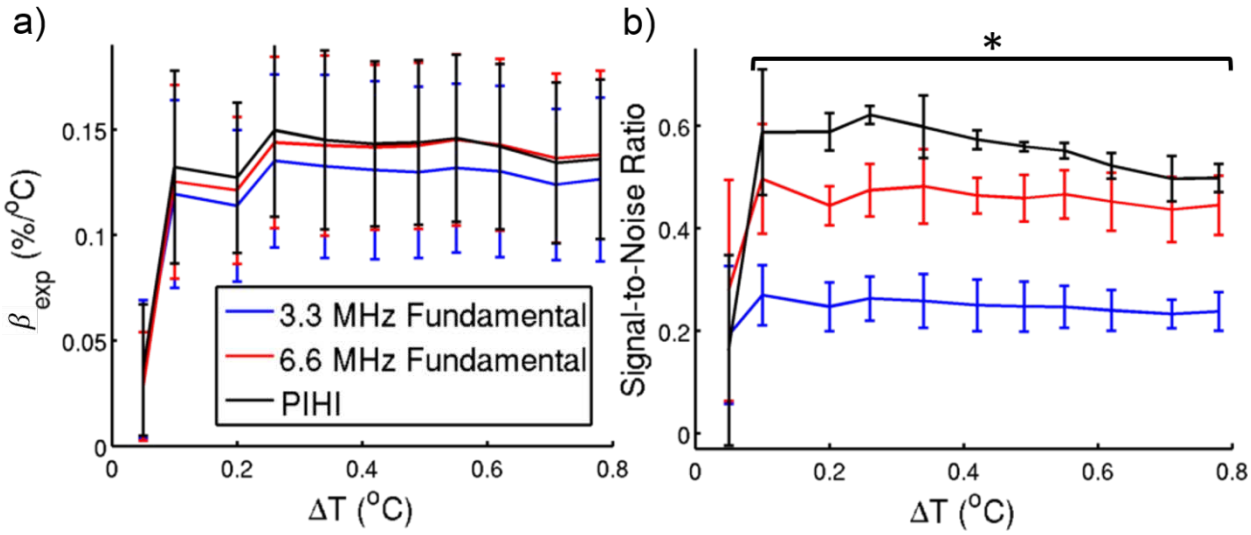

Figure 20: Results for the homogeneous gelatin (0% castor oil) phantom. In a), β_{exp} as a function of the measured temperature change is shown for three different TSI tracking modes. In b), the SNR in the heated region as a function of measured temperature changes is calculated. The "*" designates the temperatures over which PIHI tracking provides better SNR than either 6.6 MHz or 3.3 MHz tracking ($p < 0.05$).

Figure 20b shows SNR as a function of ΔT. The region over which the SNR was calculated is shown in Figure 19b and has an area equal to 125 mm^2. We observe that the trend in SNR parallels the trend in β_{eff}. In other words, for $\Delta T > 0.26$°C, the measured SNR appears to converge to a fixed value for all imaging modes. In addition, PIHI tracking improves the SNR by an average of 21% and 124% as compared to the 6.6 MHz and 3.3 MHz tracking respectively for $\Delta T > 0.10$°C (Fig. 2b, $p < 0.05$). This improvement is largely due to decreased spatial variation in the PIHI tracked thermal strain image. The decreased spatial variation is likely due to two factors which have improved the variance in the original displacement estimate. First, the PIHI tracking beam has a f_c close to 6.6 MHz. Doubling the f_c relative to the 3.3 MHz tracking pulse will

decrease the variance in the displacement tracking [70]. In addition, because the pulse inversion signal is proportional to the square of the fundamental signal, the PIHI tracking beam will have side lobes that are 6 dB lower than the side lobes for the 6.6 MHz tracking beam and will reduce off-axis scattering and further decrease variance in the displacement estimate. For ΔT < 0.10°C, the apparent strain has a very small magnitude such that there is effectively no signal which likely reflects a lower temperature limit for reliable TSI and NIT measurements.

Additionally, for NIT applications, the data in Figure 20 suggest that if a large region of interest (>100 mm^2) is chosen, temperature estimation will agree within 5-10% over a range of tracking frequencies. However, if the goal is to estimate the temperature rise in a small region of interest (≤10 mm^2), higher tracking frequencies and PIHI will provide more precise estimates of the temperature change. These tradeoffs might be important to consider in the case of monitoring of HIFU liver ablation where the penetration achieved with a lower frequency might need to be balanced against accurate temperature estimation within a pre-defined treatment area.

4.3.2 Gelatin-Castor Oil Phantom Experiment

Figure 21a shows β_{exp} as a function of castor oil percentage. Similar to Figure 20a, the value of β_{exp} is not statistically different for fundamental and PIHI tracking. This is true both with and without clutter. As previously noted, simulations have shown that a small degree of bias is introduced in the presence of stationary echoes or lower tracking frequencies [53], [70]. In spite of these simulations, Doherty et al also experimentally found that clutter corrupts displacement tracking primarily by introducing variance to the estimate [94]. Our findings are consistent with those findings because the derivative of an unbiased or minimally biased estimate should also be unbiased or minimally biased.

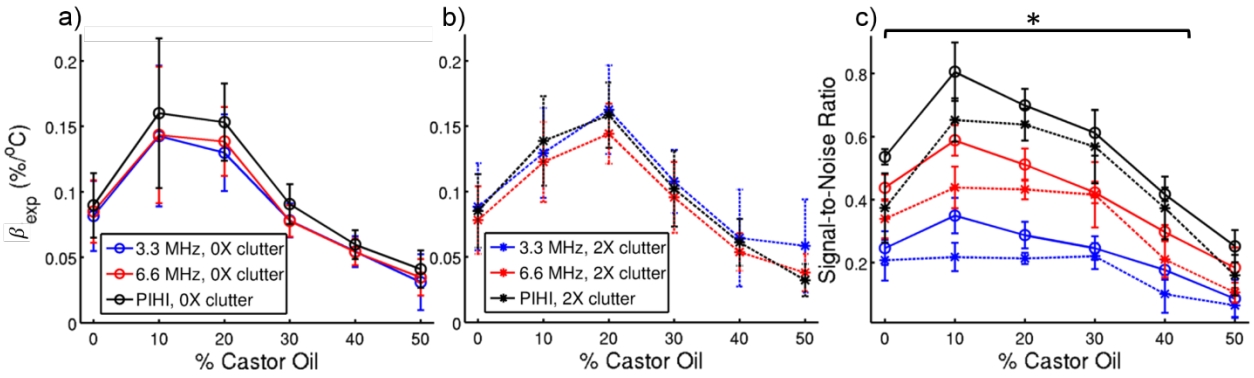

Figure 21: Results for the mixed gelatin-castor oil phantoms. In a), β_{exp} as a function of % castor oil is shown for three different TSI tracking modes with zero layers of clutter. The same data are shown with two layers of clutter in b). In c), the SNR in the heated region as a function of % castor oil is calculated. The "*" designates the temperatures over which PIHI tracking provides better SNR than either 6.6 MHz or 3.3 MHz tracking with no clutter (solid line) and with two layers of clutter (dotted line).

The literature reports that for pure castor oil, β is approximately -0.13 %/°C at room temperature [31]. We found that small percentages of castor oil initially resulted in an increase in sound speed as compared to pure gelatin. This means that the speed of sound further increases with increasing temperatures. Above 10% castor oil, β_{exp} decreases monotonically for increasing castor oil concentrations. While this finding was unexpected, Nguyen et al reported a similar trend between absolute sound speed and castor oil concentration suggesting that our measurement might be a consistent physical phenomena resulting from low concentrations of oil in gelatin [96].

Miller et al previously used a mixture model to simulate the effects of mixtures of materials on sound speed properties [90]. Our data suggests that for low percentage mixtures, Miller et al's model might not be valid because their model only produced monotonic changes in sound speed properties. These are empirical findings and, to the best of the authors' knowledge, no thorough investigations of the physics underlying the relationship between β and material

composition have been completed [29]. Additionally, our data suggest that for NIT applications where ablation is being performed in the presence of fatty liver disease, temperature underestimation is likely if β is not appropriately adjusted. Further studies are required in order to fully understand the properties of tissue mixtures that might be found in fatty liver disease or atherosclerotic plaques.

Figure 21b shows the SNR as a function of castor oil percentage. Like Figure 20b, it shows that, in the absence of clutter, PIHI tracking results in a better SNR than fundamental tracking. With the introduction of clutter, all tracking schemes suffer a decrease in SNR. However, PIHI tracking still provides a SNR which is the same or better than 6.6 MHz fundamental tracking without clutter. In the absence of clutter, PIHI tracking improves the SNR by an average of 36.4% and 145% as compared to 6.6 MHz and 3.3 MHz tracking respectively (Figure 19b, $p < 0.05$). In the presence of this clutter, the advantage of PIHI tracking grows to an average SNR improvement of 52.1% and 213% as compared to 6.6 MHz and 3.3 MHz tracking respectively (Figure 21b, $p < 0.05$). For the 50% castor oil phantom, the apparent strain and, as a result, the SNR are very small for all tracking modes. Although the trend is consistent when compared with the other phantoms, a larger number of independent images would be required to detect a significant difference.

The data from Figure 20 and Figure 21, when taken together, show that for $\Delta T > 0.26^{o}$C, the SNR is correlated with β_{exp} but not further increases in ΔT. Interestingly, these data suggest that only a small temperature increase well below American Institute of Ultrasound in Medicine thermal safety limits of 1.5^{o}C is necessary to achieve an optimal SNR. This is not only important from a safety standpoint, but also because it is expected that attenuation and phase aberration and will decrease the maximum acoustic pressure of the heating beam *in vivo* resulting in a smaller

maximum temperature rise. These data show that, for TSI, acceptable SNR might be achieved *in vivo* even with lower than expected temperature increases. This might be important for the feasibility of TSI in hepatic steatosis due to the depth of the liver and attenuation of the ultrasound beam from thick, superficial, abdominal fat. In addition to temperature rise generated, the inherent material properties, specific tracking configuration, and signal processing steps will determine the absolute SNR level.

4.3.3 Liposuction Phantom

Data for the liposuction phantom are presented in Figure 22, Figure 23, and Table 2. In Figure 22, the B-mode and TSI images are shown for a single spatial location with no clutter and two layers of clutter. Black dashed lines indicate the -6 dB beamwidth for the heating beam. The processed liposuction fat is expected to be even more homogeneous than native adipose tissue and PIHI tracking provides a qualitatively smoother TSI estimate than fundamental tracking. This is true in the absence of clutter and with two layers of clutter. It can be seen that the magnitude of the apparent strain in the images with clutter is smaller than in the images without clutter. This is because the copper mesh attenuates the heating beam resulting in a smaller temperature increase. In gelatin phantom experiments, the temperature difference with and without clutter was found to be 0.030 – 0.13ºC. Figure 23 and Table 2 show quantitative analyses for the liposuction data. Examples of lipid and water-based (gelatin) regions chosen for these calculations are shown in Figure 22b. The interface between the liposuction fat and gelatin was not perfectly flat. As a result, the exact regions chosen varied slightly depending on the spatial location imaged. In Figure 23, CNR, percent true positive area, and percent false positive

area are presented for 0, 2, and 4 layers of clutter. The statistical analyses of the magnitude of differences between the different TSI tracking modes are shown in Table 2.

Clutter degrades the performance of all TSI tracking modes in the liposuction phantom in a manner consistent with what was seen previously for the gelatin-castor oil phantoms. Furthermore, as might be expected, the degree of performance degradation is correlated to the number of layers of clutter used. PIHI tracked TSI has suffers the smallest degradation to performance. It maintains the highest CNR, the highest true positive area, and the smallest false positive area. This advantage grows when more layers of clutter are used. CNR is a useful metric to evaluate image contrast when the imaging target is inhomogeneous. This is relevant to TSI applications in which the goal is to differentiate a lipid rich core from the surrounding atherosclerotic plaque. The percent true and false positive areas are relevant metrics for atherosclerotic plaques, but are also relevant to imaging relatively homogeneous structures like livers with suspected fatty liver disease.

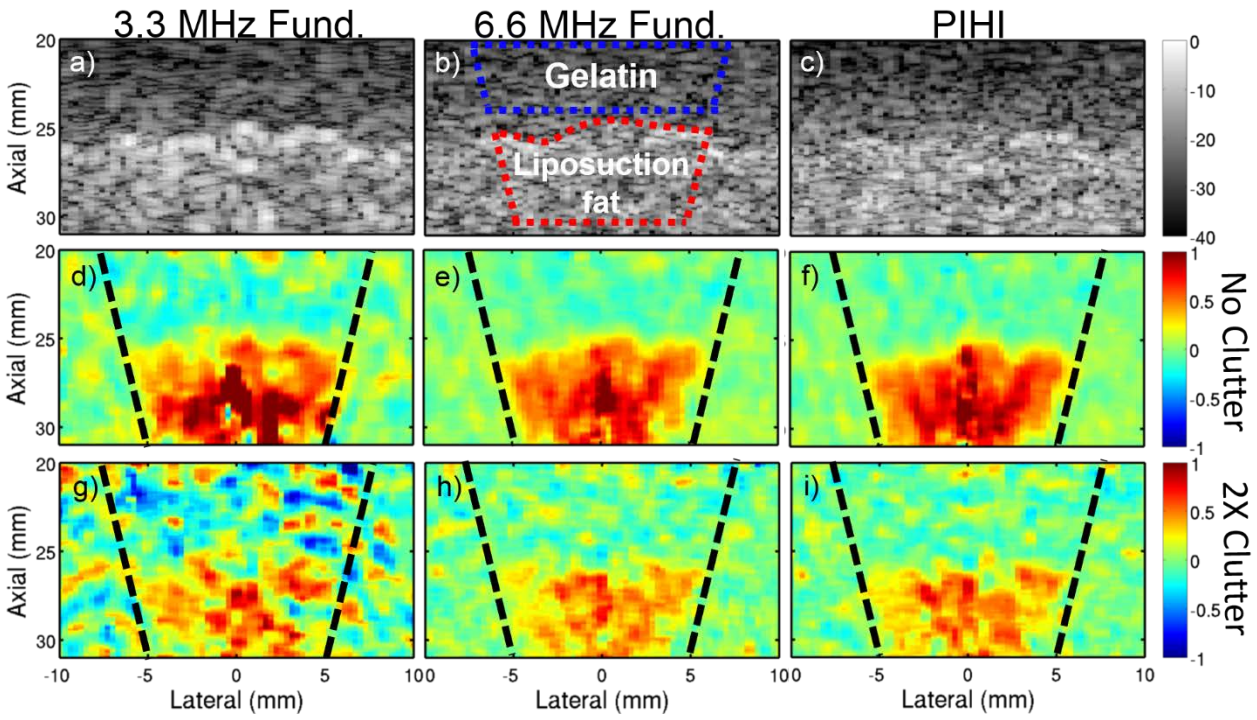

Figure 22: A set of spatially matched images of TSI using 3.3 MHz, 6.6 MHz, and PIHI tracking with zero and with two layers of clutter in the liposuction phantom. a), b), and c) show the B-mode reference images used for tracking. The dynamic range is in dB. Gelatin and liposuction layers are labeled in b). TSI images with no clutter are shown in d), e), and f). TSI images with 2 layers of clutter are shown in g), h), and i). In d) – i), the scale bar indicates % strain. Black dashed lines designate the -6 dB width of the heating beam.

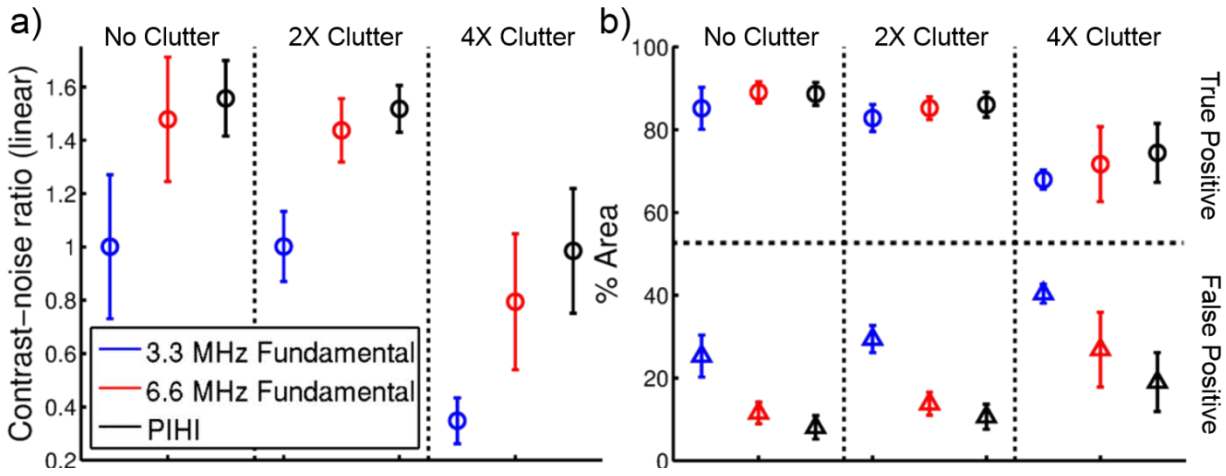

Figure 23: The CNR, true positive area, and false positive area for liposuction phantom for varying degrees of clutter. In a), the CNR for 3.3 MHz, 6.6 MHz, and PIHI TSI tracking modes are calculated for zero, two, and four layers of clutter. In b), the true and false positive percent area within the lipid and gelatin regions, respectively, are shown for the same conditions

Table 2: Differences in TSI Tracking Mode Performance for Liposuction Phantom

Pair Compared		ΔCNR (%)	Δ True Positive (%)	Δ False Positive (%)	
PIHI	6.6 MHz	NS	2.78*	3.65*	No clutter
PIHI	3.3 MHz	63.9**	NS	15.4***	
6.6 MHz	3.3 MHz	52.2*	2.76*	11.8**	
PIHI (0X)	PIHI (2X)	NS	3.84*	2.38*	2X clutter
6.6 MHz (0X)	6.6 MHz (2X)	NS	4.63**	NS	
3.3 MHz (0X)	3.3 MHz (2X)	NS	4.28*	NS	
PIHI (0X)	PIHI (4X)	35.1*	13.0*	11.1***	4X clutter
6.6 MHz (0X)	6.6 MHz (4X)	43.7**	16.6*	15.3***	
3.3 MHz (0X)	3.3 MHz (4X)	62.4*	15.3***	17.1***	

Tracking modes are compared against each other in the absence of clutter. They are also compared against themselves in the presence of two and four layers of clutter. For CNR, the percent difference is tabulated. For true and false positives, the absolute difference expressed as the percent area is tabulated. * $p < 0.05$, ** $p < 0.01$, *** $p < 0.001$, NS = Not significant

B-mode, TSI, and Oil red O histology images of the *ex vivo* CEA sample are shown in Figure 24. In Oil red O staining, lipid rich regions appear red. Based on the histology, red and blue dashed boxes were drawn to mark lipid rich and lipid poor regions, respectively. Matching regions are marked in the TSI imaging. The 3.3 MHz tracking overestimates the extent of the lipid region within the artery and produces a large number of false positive lipid regions in the surrounding gelatin. In 6.6 MHz tracking, the number of false positive lipid regions is drastically reduced and it produces an accurate representation of the lipid deposits within the artery. The images in the third row are spatially matched to the second row, but were taken in the presence of three layers of clutter. After the introduction of clutter, 3.3 MHz tracking produces false positives within the artery in the blue dashed box. The homogeneity within the surrounding gelatin region is also degraded. In the 6.6 MHz tracked image, the lipid rich region marked by

the red dashed box is lost. After the introduction of clutter, the PIHI tracked image is the most spatially comparable with the histology image and qualitatively provides best CNR between lipid and water-based regions within the artery.

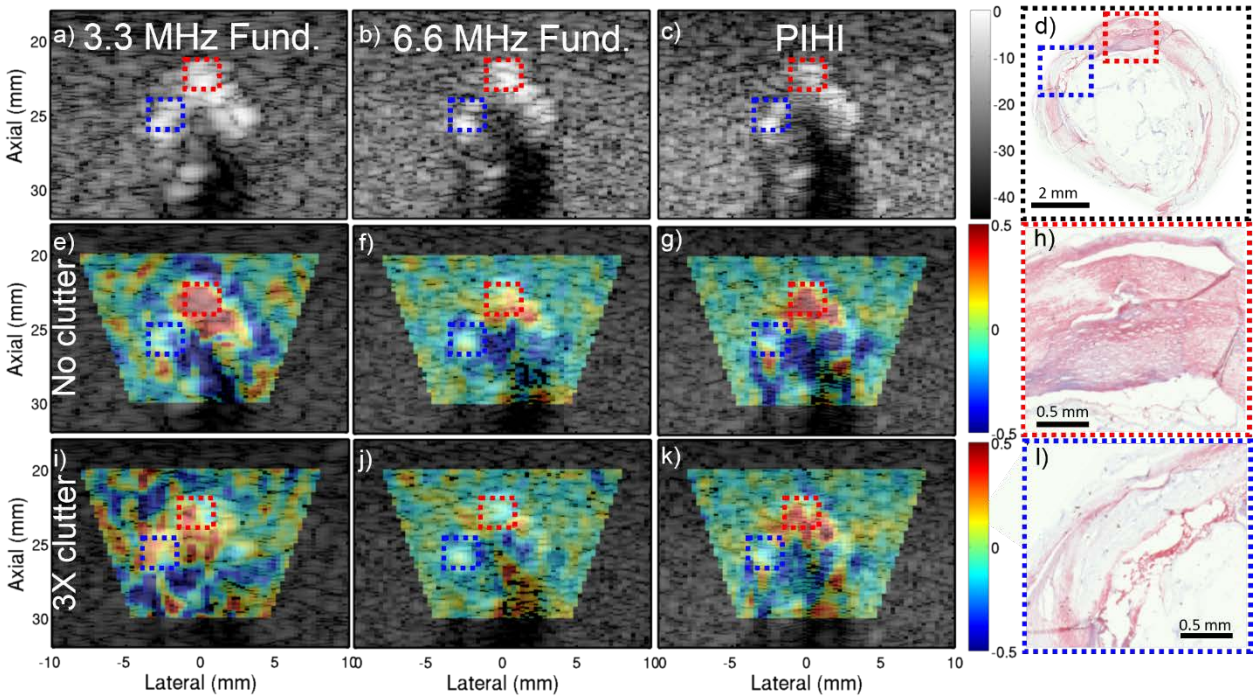

Figure 24: A set of spatially matched images of a CEA sample with TSI using 3.3 MHz, 6.6 MHz, and PIHI tracking with no clutter and with three layers of clutter. a), b), and c) show the B-mode reference images used for tracking. The scale bar indicates the dynamic range in dB. The heated region for TSI is overlaid on the reference B-mode image in e), f), and g). The scale bar indicates the dynamic range in % strain. Spatially matched images tracked in the presence of three layers of clutter are shown in i), j), and k). The scale bar is the dynamic range in % strain. A gross image of the matching Oil red O histology is show in d) and red staining indicates the presence of lipids. Red and blue dashed boxes designate lipid rich and lipid-poor regions and are magnified in h) and l) respectively.

Overall, the CEA data show that the findings previously demonstrated using simplified phantom setups are applicable to real, complex tissues. PIHI-based tracking has potential to improve TSI and NIT estimates across a range clinical applications where clutter might affect image quality.

This study is subject to several limitations resulting from practical constraints in the experimental design. The first limitation was the bandwidth (3.3 – 6.6 MHz) of the ATL L7-4

transducer used in this study. Ideally, this transducer would have had a bandwidth that extended beyond 6.6 MHz. This is because the harmonic signal has a finite bandwidth which should be captured within the passband of the transducer. Although the ATL L7-4 was able to receive harmonic signals satisfactorily, a transducer with a broader bandwidth would be expected to provide further improved harmonic signal transduction which might further improve strain estimation.

Another limitation of this study is that experiments were conducted at $\leq 25^{o}$C in order to prevent the gelatin from melting. The absolute value of β is known to change with temperature [32]. Nevertheless, we found that for the gelatin (0% castor oil) phantom between approximately 5.0 – 20^{o}C, β was within ±10% of the mean value. For pure castor oil, β was approximately constant between 25 – 40^{o}C. These finding suggest that the data in Figure 21a and Figure 22a are likely to be internally consistent. However, it still possible that these values are different than the actual values of β for *in vivo* water-based tissues. This concern is somewhat alleviated because data in Figure 21b, show that PIHI tracking consistently improves performance for a wide range of β. Nevertheless, reference values for β should be carefully measured for NIT applications which deviate significantly from the temperature ranges provided for this study in order to obtain accurate estimates of ΔT.

4.4 CONCLUSIONS

Pulse inversion harmonic tracking is combined with thermal (temporal) strain imaging in order to improve estimates of apparent strains. The improvement is quantified by comparing the strains calculated using PIHI tracking against the strains calculated from both 6.6 MHz and 3.3

MHz fundamental tracking. For large homogeneous targets >100 mm^2, precise measurements can be made independently of tracking frequency; however, for small homogeneous targets, the SNR will play a role in determining the precision of the estimate. In homogeneous oil-gelatin phantoms with clutter, PIHI tracking provides an average SNR improvement of 52.1% and 213% as compared to 6.6 MHz and 3.3 MHz tracking. In liposuction phantoms with clutter, the contrast-to-noise ratio is degraded by 35.1% for PIHI as compared to 43.7%, and 62.4% for 6.6 MHz and 3.3 MHz tracking respectively. This degradation in CNR is accompanied by an increase in false positives and decrease in true positives that parallels the trend in CNR. These changes to image quality were reflected in *ex vivo* CEA data which showed that PIHI tracking reduces false positives, identifies true positive lipid regions, and maintains the CNR between lipid rich regions and the background. Pulse inversion-based tracking can be used to improve thermal (temporal) strain estimates with applications in identification of the lipid rich cores of atherosclerotic plaques as well as quantifying hepatic steatosis.

4.5 ACKNOWLEDGEMENTS

This work was supported by NIH grants 5R01HL098320 (PI: Kim). Student training was supported by NIH training grant 5T32HL076124 (PI: Shroff).

5.0 IMAGING CHARACTERISTICS OF HIGH FRAME RATE ACOUSTIC RADIATION FORCE IMPULSE IMAGING

5.1 INTRODUCTION

ARFI imaging has been described as “remote palpation” and uses the tissue mechanical properties as the basis for image contrast. It has been investigated for a number of clinical applications including the assessment of vulnerable plaques, tumor characterization in breast and prostate tissue, and improved needle guidance [27], [39], [40], [97]–[99]. Additionally, the mechanical contrast provided by ARFI imaging is oftentimes superior to traditional B-mode acoustic contrast [41], [42]. However, the ability to provide unique, mechanical contrast in heterogeneous tissues has traditionally been counterbalanced by several weaknesses which include the inability to measure absolute elastic moduli and a low imaging frame rate [37], [38]. The rising popularity of shear wave elasticity imaging can be seen as a direct response to the first weakness [100].

Traditionally, ARFI imaging has been performed with a track-push-track configuration at each imaging line. The first track is a reference line to establish the baseline position of the tissue. The push is several hundred cycles long and mechanically perturbs the tissue. The second tracking series is 3-10 ms in duration and measures the tissue mechanical response to the push. This sequence is then repeated across all imaging lines in order to build a full image. Depending

on the number of total imaging lines, this results in an overall imaging frame rate of 1–5 Hz. In this case, there is a direct correlation between the size of the image field of view and the overall image frame rate. Efforts have been made to address the low frame rate using parallel tracking methods or novel pushing and tracking schemes [38], [101]. The most commonly used scheme is a 4:1 (track:push) scheme. In this realization of ARFI imaging, the mechanical response to the push is allowed to propagate laterally as a shear wave over a very small spatial region (<1 mm) and then tracked using four simultaneous tracking beams [102]. Thus, the total number of pushes required is reduced by a factor of four and, as a result, the overall imaging frame rate is increased by a factor of four.

One of the primary advantages of ultrasound imaging as compared to computed tomography or magnetic resonance imaging, other common non-invasive medical imaging modalities, is the ability to provide real-time imaging. This not only critical for visualizing dynamic structures like peripheral vessels or the heart, but it also compensates for ultrasound's relatively narrow field of view by enabling "scanning" and acquisition of targets. In other words, the narrow field of view of ultrasound imaging means that searching for and identifying a target using real-time imaging is an important step prior to the acquisition of images of the target organ. Because ARFI imaging is typically unable to achieve real-time frame rates, it is must rely on traditional, real-time B-mode imaging to first identify the target. If the target has poor or no acoustic contrast, the operator will be unable to locate the target for subsequent ARFI interrogation. Additionally, traditional ARFI imaging will struggle to image dynamic structures and cannot practically be used to assist in image-guided procedures.

Utilizing the multi-foci push beam and PWI approach detailed in Chapter 3.0 , we were able to achieve frame rates of more than 100 frames per second. Because one push corresponded

to a full image, it reduced the acoustic dose required to generate a single ARFI image. In this high frame rate (HFR) scheme, the limiting factor for the frame rate was the time required for the mechanical response to return to baseline. However, these advantages were enabled by the use of the multi-foci push beam as well as PWI. The multi-foci push beam provides a different stress distribution as compared to the traditional DAS push. Additionally, PWI has decreased resolution and contrast as compared to traditional DAS tracking. The aim of this chapter is to explore how these factors affect ARFI image quality.

5.2 MATERIALS AND METHODS

5.2.1 Bias and Jitter from PWI and Multi-foci Pushing

All sequences in this chapter were implemented on a Vantage (Verasonics Inc., Kirkland, WA) system with the external HIFU power supply option driving an ATL L7-4 linear array (Philips Healthcare, Amsterdam, Netherlands). We implemented two kinds of tracking modes (DAS and PWI) and two kinds of push beams (DAS and multi-foci). We designed four pulse sequences for each possible tracking and push beam combination. In order to measure the bias and jitter (standard deviation) of PWI relative to DAS tracking, we centered the push at 0 mm laterally and tracked a single A-line at 0 mm laterally. RF data were saved and dynamic receive beamforming was performed offline. Loupas' estimator was used to calculate displacement between the A-lines before and after the push using a 2.2λ kernel. The displacement data were median filtered using a 10 pixel kernel and then filtered with a 2 kHz temporal low pass filter. Each of the four sequences was applied at 10 different locations within a homogeneous phantom

for a total of 40 acquisitions. Bias and jitter were calculated in a 1 mm region centered about 25 mm axially using Equation 21 and Equation 22, respectively. During all imaging sequences in this chapter, the transducer was held with a clamp and coupled to the phantoms with degassed water.

$$Bias = E[u_{PWI} - u_{DAS}]$$

Equation 21: Bias introduced by plane wave tracking. The bias is the expected value of the difference in the displacement found with PWI tracking, u_{PWI}, and the displacement found with DAS tracking, u_{DAS}.

$$Jitter = \sigma_u$$

Equation 22: Equation to calculate jitter. The jitter or standard deviation is the sample standard deviation across the ten independent datasets.

5.2.2 Full frame ARFI Acquisition

We implemented two pulse sequences to acquire full ARFI images. The first sequence is a "standard" 1:1 push-track ARFI sequence using DAS beamforming. In this sequence, the tracking parameters are shown in Table 3. The push was 500 cycles in duration transmitted at 4.46 MHz with an F/1.3 configuration focused at 25 mm axially. The second sequence was the HFR ARFI sequence utilizing multi-foci pushing and PWI. The PWI tracking parameters are also shown in Table 3. The multi-foci push is also transmitted at 4.46 MHz. in 100 cycle bursts that alternated between the three and four foci beams. A total of 500 three foci beams and 500 four foci beams were transmitted (1000 cycles overall).

Table 3: Tracking Parameters for Full Frame ARFI Acquisition

	Delay-and-sum	Plane Wave
Frequency	5.21 MHz	5.21 MHz
F/# (Transmit | Receive)	F/1 | F/1	N/A | F/1
Transmit Focus	25 mm, no apodization	N/A
Pulse repetition frequency	10 kHz	10 kHz
# lines (full image)	45	256
Line spacing	0.298 mm	0.148 mm

The signal processing was the same as in 5.2.1 except that a 2-D median filter with a 10 X 3 pixel kernel was used. The contrast and contrast-to-noise ratio (CNR) were calculated using Equation 23 and Equation 24, respectively.

$$Contrast = \frac{u_{bg}}{u_t}$$

Equation 23: Equation for mechanical contrast. The mean displacement in the background, u_{bg}, is divided by the mean displacement in the target region, u_t.

$$CNR = \frac{(u_{bg} - u_t)}{\sqrt{\sigma_{bg}^2 + \sigma_t^2}}$$

Equation 24: Equation for CNR. Mean displacement in the background, u_{bg}; Mean displacement in the target, u_t; Standard deviation of the displacement in the background, σ_{bg}; Standard deviation of the displacement in the target, σ_t.

5.2.3 Homogeneous Phantom

A homogeneous gelatin phantom was fabricated to assess the bias, jitter, and the ARFI imaging field of view. The phantom was made with water, 4% (g/mL) gelatin from porcine skin (Sigma Aldrich Co., MO, USA), and 10% (g/mL) cellulose (Sigma Aldrich Co., MO, USA). The gelatin and water were mixed thoroughly and then heated until the solution reached approximately 65^{o}C or became clear. Then, cellulose was added and allowed to thoroughly mix. The mixture was allowed to cool to room temperature and then poured into a pre-chilled mold in a -20^{o}C freezer. The phantom was allowed to cure at this temperature for an additional hour. Afterwards, it was allowed to come to room temperature and imaged using the aforementioned system. The ultrasound probe was held with a clamp and coupled to the phantom using degassed water. The Young's modulus of a representative phantom sample was measured to be 8.6 ± 0.4 kPa using a compression test machine (Insight, MTS Systems, Eden Prairie, MN, USA).

5.2.4 Layered Contrast Phantom

A layered phantom was constructed in order to assess the image contrast. The phantom was constructed in two steps. The first step was the construction of a rectangular, stiff gelatin phantom. The phantom was 7% gelatin (g/mL) and 5% cellulose (g/mL). The phantom was otherwise fabricated using the same procedure as 5.2.2 and had a Young's modulus of 16.8 kPa ± 4.4 kPa. After this phantom had set, it was removed from the original mold and placed in a larger, rectangular mold. The phantom and container were held at room temperature. A second phantom using the recipe from 5.2.2 was fabricated. It was allowed to cool to approximately 45^{o}C and then poured into the rectangular mold containing the first phantom. This was allowed

to set in a -20^{o}C freezer for one hour. The layered phantom was imaged with the interface orthogonal to the transducer face and positioned at 0 mm laterally. In this manner, the left half of the field of view was used to image the stiff gelatin layer and the right half was used to image the soft layer.

5.3 RESULTS & DISCUSSION

The effects of multi-foci pushing and plane wave tracking on the calculated displacement are shown in Table 4. Multi-foci pushing generates a smaller peak displacement and smaller jitter. The decrease in the peak displacement is likely the result of the nature of the multi-foci push beam. Because it is temporally interleaved, the time averaged intensity is reduced at locations where the two multi-foci beams do not completely overlap. This reduction in intensity reduces the magnitude of the impulsive force (Equation 2) and results in a smaller peak displacement. Jitter is known to scale with displacement magnitude and the percentage jitter is slightly smaller, but very similar between both the multi-foci and DAS pushes [70]. Decreased shearing due to the broader multi-foci pushing beam might also contribute to the slightly smaller percentage jitter in the case of the multi-foci push.

Plane wave tracking of both pushing modes resulted in an increase in the measured jitter. Because PWI only utilizes one-way beamforming, there is a loss in resolution as well as a degradation of contrast. Both of these factors have been shown to affect the jitter in the estimate [70], [94]. Interestingly, the relative increase in jitter is smaller when the multi-foci push is tracked. This is likely because the push beam is broad which reduces shearing under the tracking point spread function. Additionally, PWI results in a 15% bias relative to DAS tracking. Overall,

when “standard” (DAS push/DAS tracking) and HFR ARFI (Multi-foci push/plane wave tracking) are compared, the percentage jitter for HFR ARFI is slightly greater than the percentage jitter for standard ARFI. HFR ARFI also results in a small increase in bias relative to DAS tracking.

Table 4: The Effects of Multi-foci Pushing and Plane Wave Tracking

		DAS focus Tracking			Plane Wave Tracking			
		Peak Disp. (μm)	**Bias (μm, %)**	**Jitter (μm, %)**	**Peak Disp. (μm)**	**Bias (μm, %)**	**Jitter (μm, %)**	**ΔJitter (%)**
Push Type	**Multi-foci**	4.6	n/a	0.68 (15%)	3.9	0.70 (15%)	0.94 (24%)	0.26 (38%)
	DAS focus	5.4	n/a	1.05 (19%)	4.6	0.83 (15%)	1.32 (29%)	0.37 (35%)

The temporal response of the mechanical perturbations generated by standard ARFI and HFR ARFI were also compared in a homogeneous phantom. The tracked displacement profiles are shown in Figure 25. As expected, the magnitude of jitter is greatest at the point of peak displacement. The HFR ARFI response has a slower temporal response than traditional ARFI imaging. This is likely because the multi-foci push contains lower spatial frequencies than the DAS push beam. The spatial frequencies in the push beam are known to affect the frequency content of the mechanical perturbation [103], [104]. Shear wave dispersion imaging is related to ARFI imaging and aims to measure the dispersive characteristics of tissue. Because of the unique frequency content in the multi-foci beam, it might also be useful for shear wave dispersion imaging.

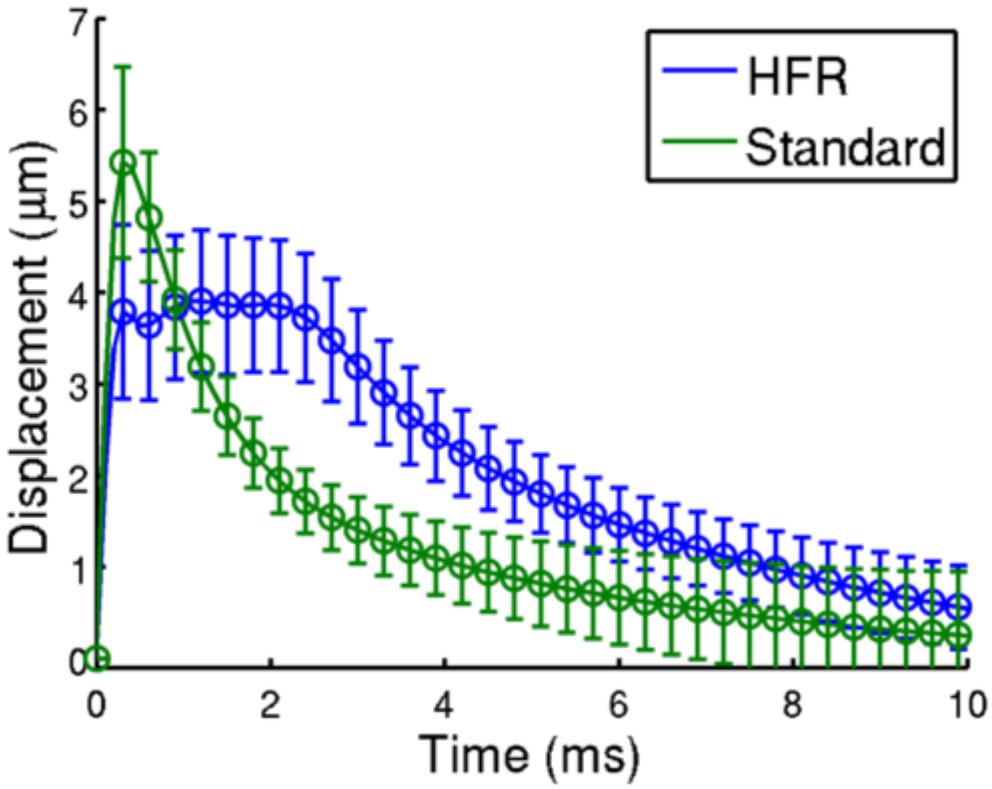

Figure 25: Displacement vs. time for HFR and standard ARFI imaging. The displacement is calculated in a 1 mm region about 25 mm for both imaging modes. The error bars represent the jitter across the 10 acquisitions.

Full frame standard and HFR ARFI imaging are compared in Figure 26. In panels a) and b), the mean displacement and jitter are shown for standard ARFI imaging. It can be seen that displacement is generated in a narrow axial region centered about 25 mm corresponding to the depth of field of the DAS push beam. The jitter is also greatest in the region of peak displacement. The mean displacement and jitter for HFR ARFI imaging are shown in panels c) and d). The displacement pattern closely resembles the simulated pressure profile for the multi-foci beam. This displacement profile has a long depth of field. However, the lateral width of the push beam narrows with depth. Additionally, it should be noted that the images in panels a) and b) were generated using 45 push pulses and that the overall acquisition time is 45 times longer than the data shown in panels c) and d). The overall displacement magnitude in panel c) is lower

than the displacement found using standard ARFI imaging and is consistent with the data presented in Table 4. The jitter in HFR imaging is of similar magnitude to the jitter in standard ARFI imaging.

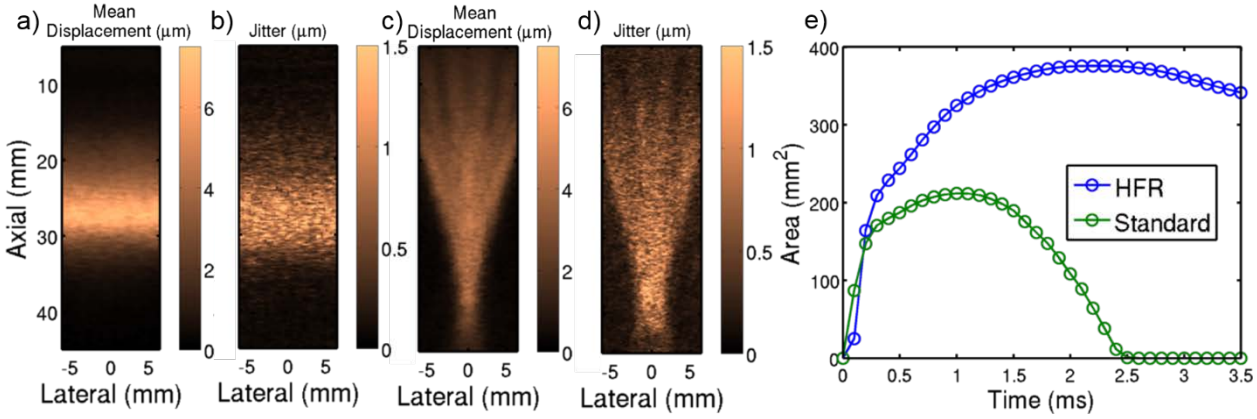

Figure 26: Full frame standard ARFI imaging compared to HFR ARFI imaging. In a) and b), the mean displacement and jitter for standard ARFI imaging are shown. In c) and d), the mean displacement and jitter are shown for HFR ARFI imaging. Panels a), b), c), and d), correspond to data at t = 0.3 ms. In e), the area (>2 μm displacement) of the push beams are compared.

However, given the decreased displacement magnitude, this results in a smaller displacement SNR. In panel e), the effective field of view (>2 μm displacement) of the ARFI imaging modes are compared. Typically, the peak displacement occurs around approximately 0.3 ms. The exact time of the peak will depend on the configuration of the push beam as well as the tissue elasticity. ARFI displacement images are displayed near the peak displacement because the resolution of the images becomes degraded at later time steps [105]. Thus, the most relevant times to consider in panel e) are those early time steps. During those time steps, it is evident that HFR imaging provides a comparable or greater effective field of view as compared to standard ARFI imaging.

The CNR and contrast are compared for standard and HFR imaging in Figure 27. In order to calculate the CNR and contrast, the beam shape was obtained from the mean displacement data in Figure 26. The displacement within the beam inside the stiff and soft gelatin were used to calculate values for the target and background regions respectively. The CNR is shown as a function of depth for both HFR and standard ARFI for three different times after the push. It can be seen that in standard ARFI imaging, good CNR is achieved within the depth of field of the push beam. The peak CNR occurs near the axial focus and continues to grow in magnitude at later time steps. These findings are consistent with similar studies in the literature [105]. As was noted previously, later time steps after the peak displacement demonstrate blurring of the lesion boundaries and degradation in the spatial resolution. For HFR ARFI imaging, the magnitude of the CNR is greatest near 20 mm axially and is relatively stable over the entire axial range. Overall, the peak CNR for HFR ARFI imaging is smaller in magnitude than the peak CNR for standard ARFI imaging. Despite the degradation in CNR for HFR ARFI imaging, the stiff layer is visible in panel h) of Figure 27. However, these data do suggest that, especially for small or low contrast inclusions, HFR ARFI imaging will likely provide poorer image quality than standard ARFI imaging.

The contrast for standard and HFR ARFI imaging show similar trends to the CNR. However, the contrast for standard and HFR ARFI have similar magnitudes. This is likely because the CNR accounts for the variability in the displacement estimate in the target and background. Data in Table 4 show that the variation (jitter) is greater when plane wave tracking is compared to DAS tracking. The increased jitter can be appreciated in panels g) and h) which show a single acquisition of standard and HFR ARFI respectively.

These data suggest that plane wave tracking has the largest impact on HFR ARFI imaging quality. Data from Table 4, Figure 26, and Figure 27 suggest that PWI results in increased jitter and bias as well as decreased CNR. These image quality tradeoffs come with a 45-fold increase in the overall imaging frame rate. Even with degraded image contrast relative to standard ARFI, HFR ARFI was able to demonstrate sufficient contrast to differentiate between two layers with a 2:1 contrast ratio.

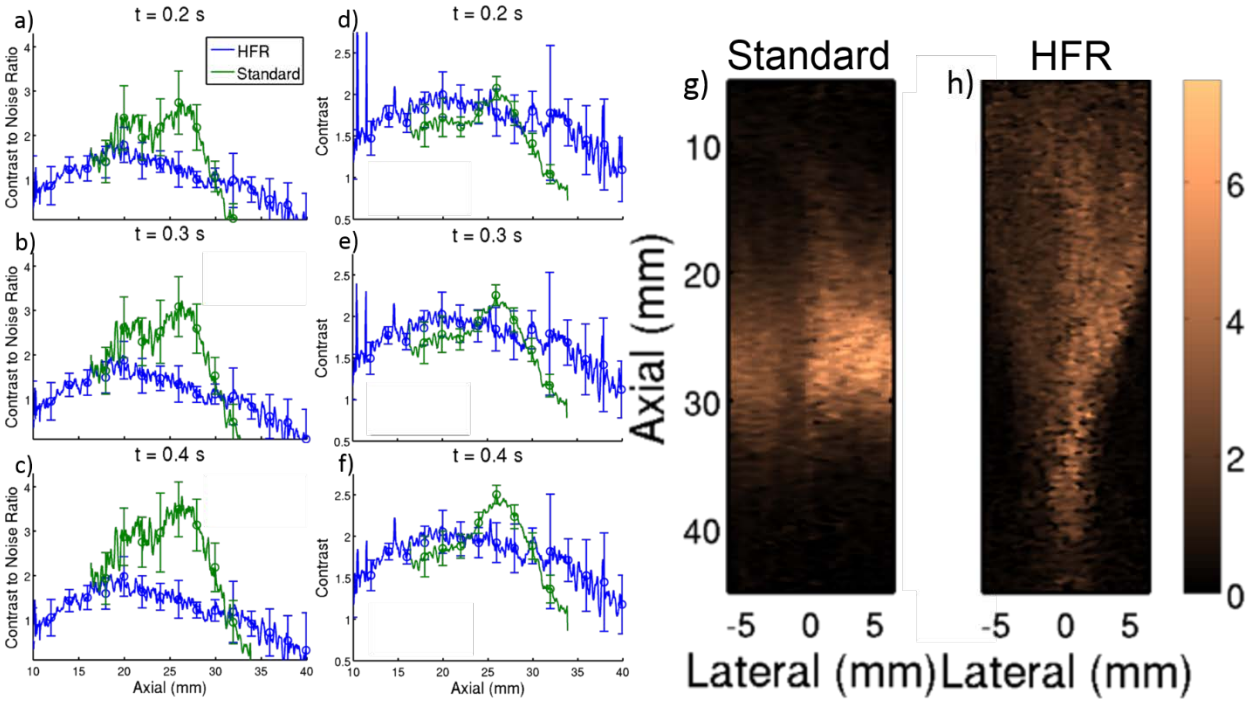

Figure 27: Contrast and CNR for standard and HFR ARFI with a layered phantom. In panels a), b), and c), the CNR is plotted as a function of depth for different times. Similarly, d), e), and f) show the contrast versus depth. Representative ARFI images are show in g) and h).

If indeed, the decreased image quality is due to plane wave tracking, there exist several techniques that might help to improve the image quality. Several groups have shown that harmonic tracking can be used to improve displacement estimation [82], [94], [95]. Additionally,

it is possible that the multi-foci push beam could be further optimized in order to improve either the push area or the mechanical contrast that is generated. In addition to changes in the pulse sequence, several groups have explored more sophisticated displacement tracking algorithms. One particularly promising algorithm utilizes a form of Bayesian estimation which has been shown to dramatically reduce the jitter in ARFI images [55], [56]. These approaches were not implemented in this chapter because the goal was to establish a baseline for the two imaging modes.

In addition to the image acquisition time, another barrier to real-time ARFI imaging is real-time signal processing. In this chapter, all signal processing was performed offline. However, several groups have already shown that GPU-based algorithms can be used to accelerate these computationally expensive techniques to real-time speeds [106], [107]. Both real-time image acquisition and signal processing are critical for potential point-of-care or ARFI-guided imaging applications. To date, these applications have been hindered by long image acquisition times. However, the HFR ARFI imaging approach presented in this chapter enables further exploration of these applications.

5.4 CONCLUSIONS

Temporally interleaved multi-foci beamforming was combined with plane wave imaging in order to create an ultrasound pulse sequence for high frame rate acoustic radiation force impulse imaging. In our implementation a single multi-foci push is able to produce a full ARFI image. This image has a field of view that is comparable or larger than standard ARFI imaging sequences which require 45 pushes. In our realization, this corresponded to a 45-fold increase in

the effective frame rate. The use of plane wave imaging to track the mechanical response to the ARFI push degrades the image quality. It increases the jitter by 6%, increases the relative bias by 15%, and decreases the peak contrast-to-noise ratio from approximately 3.5 ± 0.6 to 2.0 ± 0.4. Interestingly, despite the decrease in CNR, the standard and HFR ARFI approaches have similar contrast suggesting that more advanced tracking techniques could be used to improve the overall image quality in HFR ARFI. HFR ARFI could be coupled with existing GPU-based displacement tracking algorithms to produce real-time ARFI imaging which would have numerous applications including imaging dynamic structures like the heart or vasculature, needle guidance, and point-of-care assessment.

5.5 ACKNOWLEDGEMENTS

This work was supported by NIH grants 5R01HL098320 (PI: Kim). Student training was supported by NIH training grant 5T32HL076124 (PI: Shroff). I would also like to thank Dr. Mark Palmeri for invaluable discussions related to this work.

6.0 CONCLUSIONS AND FUTURE WORK

6.1 CONCLUSIONS

Thermal strain and acoustic radiation force impulse imaging are promising ultrasound technologies that might have applications for non-invasive assessment of vulnerable atherosclerotic plaques. Initial efforts in the development of TSI were based on a system that utilized separate heating and imaging arrays. Signal processing was developed to improve estimates of thermal strain from data acquired using this system. This work showed that utilizing two different displacement estimators was a means of improving the final estimate of thermal strain.

However, fundamental limitations in the system ranging from the center frequency for imaging as well as the impractical nature of separate heating and imaging arrays motivated the development of new approach. Temporally interleaved multi-foci beamforming is an approach to beamforming that permits the formation of broad, homogeneous beams that are suitable for both TSI heating and ARFI pushing. We demonstrated that when this approach was modified to allow for variable lateral and axial foci, highly homogeneous beams with broad areas could be achieved for a number of transducer geometries and frequencies. This beamforming approach was used as the basis for a combined TSI and high frame rate ARFI imaging sequence that provided information about both the compositional and mechanical properties of tissue.

In order to better understand the imaging properties of TSI with multi-foci beamforming, we performed a series of phantom and *ex vivo* studies to explore the effects of the heating duty cycle and percentage lipid on the estimated thermal strain signal. These studies showed that under ideal conditions, a temperature rise as small as 0.25^{o}C could be detected and that TSI was sensitive to mixtures of lipid and water-based tissues. We further went on to show that pulse inversion harmonic tracking could be combined with the multi-foci heating approach to generate an improved estimate of the thermal strain signal in all of these cases.

In order to explore the tradeoffs of HFR ARFI imaging, we conducted a series of phantom studies to understand the consequences of multi-foci pushing and plane wave imaging on jitter, bias, and image contrast. In our implementation, we showed that HFR AFRI imaging improved the imaging frame rate by 45-fold at the cost of increased jitter, bias, and degradations in image contrast. It appeared that these decreases in image quality were due, in large part, to plane wave imaging. Despite these degradations, we showed that HFR ARFI imaging was able to provide enough contrast to differentiate two layers with a 2:1 stiffness ratio.

Overall, there is large potential utility for simultaneous TSI and HFR ARFI imaging. TSI provides compositional contrast and HFR ARFI provides mechanical contrast. While the contrast might be similar in many circumstances, there are key, potential exceptions which give insight into the utility of these complementary imaging modalities. For example, in ARFI imaging, the tissue displacement is measured and tissue with low, relative displacement is generally assumed to have a higher Young's modulus. However, the displacement actually depends on the intensity of the push beam as well as the acoustic absorption coefficient of the tissue. Thus, phase aberration and varying acoustic properties within a heterogeneous plaque can complicate interpretation of ARFI images. On the other hand, TSI generates differential contrast between

water and lipid-based tissues. Thus, positive thermal strain, independent of magnitude, is an unambiguous indicator of lipid-based tissue.

However, TSI also suffers from certain limitations. In TSI, the strain is calculated from the derivative of the displacement. In general, calculating a numerical derivative is a noise amplifying step. In order to minimize amplification of noise, the derivative was calculated using a Savitzky-Golay filter that was several millimeters in length. While this helps to suppress the noise, it also degrades the spatial resolution of the subsequent thermal strain image. As a result, clearly measuring the thickness of the fibrous cap is challenging from thermal strain images. However, ARFI image contrast is directly derived from the displacement estimates and groups have recently shown that measurements of fibrous cap thickness from ARFI images correlate well with cap thickness measurements from histology [97].

Overall, HFR ARFI and TSI provide mechanical and compositional imaging contrast with complementary applications in interrogation of carotid atherosclerotic plaques. The work in this dissertation provides a foundation for further development of these technologies and future studies involving human subjects.

6.2 FUTURE WORK

6.2.1 Temporally Interleaved Multi-foci Beamforming

The multi-foci beamforming approach presented in 3.0 utilized variable axial and lateral foci to produce a broad, homogeneous beam. In order to choose the foci, a semi-manual, greedy, iterative, optimization approach was used. This approach was utilized primarily to simplify a

computationally expensive optimization. Thus, although the beams that were achieved met the minimum design criteria, the final result is unlikely to be truly optimal.

One of the primary deficiencies that forced this approach was the absence of a well-defined cost function. A good cost function would reflect the desire to achieve a broad, homogeneous beam meaning that it should account for both the amplitude of the pressure distribution as well as the effective area of the pressure distribution. Designing a good cost function would open the approach to a number of well-studied optimization algorithms that were developed to address problems associated with large, complex search spaces. Furthermore, a well-designed cost-function would give the user much more control over the final properties of the beam. Better control of the beam properties could lead to improved heating or pushing beams.

6.2.2 Thermal Strain Imaging Motion Correction

One of the primary remaining challenges before large scale studies of TSI can proceed is the issue of motion correction. TSI measures a signal that is typically on the order of microns. However, operator motion, patient motion, and cardiac motion are all orders of magnitude larger and will completely corrupt even the most robust TSI signal. ARFI and shear wave imaging have also been faced with this problem. Those imaging modalities have successfully addressed this issue by exploiting the fact that the imaging occurs within milliseconds and that the ARFI tissue mechanical response should return to a zero baseline [108]–[110]. Using these assumptions, a polynomial motion filter can be used to extract a micron level signal even in the presence of large motion artifacts.

However, unlike ARFI, the TSI sequence occurs over seconds and the measured signal does not return to a zero baseline within a reasonable time frame. Dutta et al. utilized a time-series analysis approach to separate TSI motion from cardiac motion. However, this approach required acquisition of data over several cardiac cycles [111]. Additionally, it does not account for the stochastic nature of operator and bulk patient motion. In reality, it is unlikely that a single approach will be sufficient to adequately address this issue. Below, I outline four potential approaches that could be explored to address this issue.

1. The physics of ultrasonic heat transfer in biological tissues is well understood and can be accurately modeled [83]. It follows that the thermal strain generated from ultrasound heating should also follow a predictable course which is in direct contrast to the stochastic nature of operator or patient motion. This relationship can be exploited to assist in correction of operator or patient motion. The problem is slightly complicated by the presence of convective cooling from large arteries [111]. Although initial simulations suggest that this cooling is minimal, experiments should be conducted to confirm this result.
2. Cardiac motion is highly periodic. Dutta et al. have already shown that it is possible to separate the thermal strain signal from mechanical cardiac motion over several cardiac cycles [111]. A sequence could be designed to separate acquire several cycles worth of representative cardiac motion. Then, TSI could be performed within a single cardiac cycle. The representative cardiac motion could be used to correct the TSI signal generated over a single cardiac cycle.
3. We showed in 3.0 that adequate heating for TSI could be achieved within 1 second. This corresponds to approximately one cardiac cycle for normal heart rates. However,

the duration could be further shortened. We showed in 4.0 that, in the absence of motion artifacts, robust TSI signal could be detected even for temperature rises <1ºC. Further improvements in multi-foci beamforming or updated safety guidelines might also make this option feasible [112], [113]. Additionally, advanced displacement estimation techniques can be used to increase the accuracy of detecting of small signals [55], [56].

4. In order to compensate for motion, a reasonable requirement is to first be able to track the motion. This can be easily achieved by interleaving imaging frames within the heating pulse. To some degree, this was already achieved using the sequence described in 3.0 . However, this could be further improved by updating these images in real-time so that the operator can use this feedback to minimize motion.

6.2.3 High Frame Rate Acoustic Radiation Force Imaging

As was noted in 5.1 and 5.3, there are several interesting future directions for HFR ARFI imaging. ARFI is already a relatively well-established imaging modality relative to TSI. Siemens Medical Solutions and GE Healthcare have received United States Food and Drug Administration 510K approval for devices that utilize ARF for diagnostic imaging. To date, however, ARFI imaging has suffered from the aforementioned limitations. Real-time ARFI imaging has a number of potential applications for a broad range medical specialties including emergency medicine, anesthesiology, orthopedic medicine, cardiovascular medicine, hepatology, and radiology. The success of many of these potential applications will depend on maintaining and improving current image quality. A number of approaches to address these concerns were presented in 5.3 and should be explored.

One future application that was only briefly mentioned was the application of the multi-foci push beam to shear wave elastography imaging. Shear wave elastography imaging relies on the propagation of the "push" as a shear wave. The propagation speed of this wave is proportional to the shear modulus of the tissue. Recently groups have been investigating the use of shear wave imaging to measure the dispersive characteristics of tissue [114]. However, the push beams used to conduct these investigations have been limited to DAS generated push beams. Multi-foci beamforming might provide a wider range of push beams which might have applications for shear wave dispersion imaging.

6.2.4 Future Human Studies

In future human studies, there are two critical goals. First, studies should be conducted to establish the accuracy and reproducibility of TSI and ARFI imaging in a representative population of human subjects. These factors are of critical importance and will strongly influence the potential clinical impact of TSI and ARFI imaging. Aside from the technical issues with the imaging modalities that have already been discussed, one important choice that must be determined for such a study is the gold standard against which TSI and ARFI imaging will be compared. Histology has long been the benchmark against which non-invasive imaging modalities were graded. However, comparisons between histology and imaging data are rife with complicating factors including, but not limited to, different slice thicknesses, deformation of tissue during the embedding and cutting process, and challenging image co-registration. For these reasons, multi-contrast MRI might be a suitable alternative to histology. In MRI, there is some control over the slice thickness and the *in vivo* shape of the artery is preserved.

Additionally, MRI is able to obtain isotropic 3-D volumes, which might more accurate and easy co-registration of images.

Depending on the results of this first study, subsequent studies should be directed towards identifying the clinical utility of combined TSI and ARFI imaging. As was previously mentioned, the concept of the vulnerable plaque is well-established, but there is little high quality evidence to support clinical intervention based off of this concept. A randomized, double-blind study is the gold standard for clinical evidence and could be used to establish protocols for the manner in which TSI and ARFI imaging findings would influence CEA intervention. Specifically, this study would be structured to randomize asymptomatic patients with high-grade stenosis and clinically worrisome findings on TSI and ARFI imaging into either a surgical or medical arm. Such a study would help to definitively establish whether a soft, lipid rich necrotic core or a thin fibrous cap were predictors of future, adverse cerebrovascular outcomes. Additional studies to establish the efficacy of longitudinal monitoring and the effects of medical therapies on plaque stabilization could also be pursued. Overall, if the remaining technical challenges facing TSI and ARFI imaging are addressed, there are a number of clinically significant studies that could be pursued that could have an important impact on clinical practice.

BIBLIOGRAPHY

[1] D. Mozaffarian, E. J. Benjamin, A. S. Go, D. K. Arnett, M. J. Blaha, M. Cushman, S. R. Das, S. de Ferranti, J.-P. Després, H. J. Fullerton, V. J. Howard, M. D. Huffman, C. R. Isasi, M. C. Jiménez, S. E. Judd, B. M. Kissela, J. H. Lichtman, L. D. Lisabeth, S. Liu, R. H. Mackey, D. J. Magid, D. K. McGuire, E. R. Mohler, C. S. Moy, P. Muntner, M. E. Mussolino, K. Nasir, R. W. Neumar, G. Nichol, L. Palaniappan, D. K. Pandey, M. J. Reeves, C. J. Rodriguez, W. Rosamond, P. D. Sorlie, J. Stein, A. Towfighi, T. N. Turan, S. S. Virani, D. Woo, R. W. Yeh, and M. B. Turner, "Heart Disease and Stroke Statistics—2016 Update A Report From the American Heart Association," *Circulation*, p. CIR.0000000000000350, Dec. 2015.

[2] J. C. Grotta, "Carotid Stenosis," *New England Journal of Medicine*, vol. 369, no. 12, pp. 1143–1150, Sep. 2013.

[3] V. A. Mantese, C. H. Timaran, D. Chiu, R. J. Begg, and T. G. Brott, "The Carotid Revascularization Endarterectomy Versus Stenting Trial (CREST) Stenting Versus Carotid Endarterectomy for Carotid Disease," *Stroke*, vol. 41, no. 10 suppl 1, pp. S31–S34, Oct. 2010.

[4] "Beneficial effect of carotid endarterectomy in symptomatic patients with high-grade carotid stenosis. North American Symptomatic Carotid Endarterectomy Trial Collaborators," *N. Engl. J. Med.*, vol. 325, no. 7, pp. 445–453, Aug. 1991.

[5] "Endarterectomy for asymptomatic carotid artery stenosis. Executive Committee for the Asymptomatic Carotid Atherosclerosis Study," *JAMA*, vol. 273, no. 18, pp. 1421–1428, May 1995.

[6] A. L. Abbott, "Medical (Nonsurgical) Intervention Alone Is Now Best for Prevention of Stroke Associated With Asymptomatic Severe Carotid Stenosis Results of a Systematic Review and Analysis," *Stroke*, vol. 40, no. 10, pp. e573–e583, Oct. 2009.

[7] L. Marquardt, O. C. Geraghty, Z. Mehta, and P. M. Rothwell, "Low Risk of Ipsilateral Stroke in Patients With Asymptomatic Carotid Stenosis on Best Medical Treatment A Prospective, Population-Based Study," *Stroke*, vol. 41, no. 1, pp. e11–e17, Jan. 2010.

[8] G. Raman, D. Moorthy, N. Hadar, I. J. Dahabreh, T. F. O'Donnell, D. E. Thaler, E. Feldmann, J. Lau, and G. D. Kitsios, "Management Strategies for Asymptomatic Carotid

StenosisA Systematic Review and Meta-analysis," *Ann Intern Med*, vol. 158, no. 9, pp. 676–685, May 2013.

[9] F. H. McDowell, J. Potes, and S. Groch, "The natural history of internal carotid and vertebral-basilar artery occlusion," *Neurology*, vol. 11, no. 4 Part 2, pp. 152–157, Apr. 1961.

[10] Dyken ML, Klatte E, Kolar OJ, and Spurgeon C, "Complete occlusion of common or internal carotid arteries: Clinical significance," *Arch Neurol*, vol. 30, no. 5, pp. 343–346, May 1974.

[11] J. R. Romero, A. Pikula, T. N. Nguyen, Y. L. Nien, A. Norbash, and V. L. Babikian, "Cerebral Collateral Circulation in Carotid Artery Disease," *Curr Cardiol Rev*, vol. 5, no. 4, pp. 279–288, Nov. 2009.

[12] Z. A. Fayad and V. Fuster, "Clinical Imaging of the High-Risk or Vulnerable Atherosclerotic Plaque," *Circulation Research*, vol. 89, no. 4, pp. 305–316, Aug. 2001.

[13] J. R. Guyton and K. F. Klemp, "The lipid-rich core region of human atherosclerotic fibrous plaques. Prevalence of small lipid droplets and vesicles by electron microscopy.," *Am J Pathol*, vol. 134, no. 3, pp. 705–717, Mar. 1989.

[14] F. Jashari, P. Ibrahimi, R. Nicoll, G. Bajraktari, P. Wester, and M. Y. Henein, "Coronary and carotid atherosclerosis: Similarities and differences," *Atherosclerosis*, vol. 227, no. 2, pp. 193–200, Apr. 2013.

[15] W. Peeters, W. E. Hellings, D. P. V. de Kleijn, J. P. P. M. de Vries, F. L. Moll, A. Vink, and G. Pasterkamp, "Carotid Atherosclerotic Plaques Stabilize After Stroke Insights Into the Natural Process of Atherosclerotic Plaque Stabilization," *Arterioscler Thromb Vasc Biol*, vol. 29, no. 1, pp. 128–133, Jan. 2009.

[16] R. Virmani, F. D. Kolodgie, A. P. Burke, A. Farb, and S. M. Schwartz, "Lessons from sudden coronary death: a comprehensive morphological classification scheme for atherosclerotic lesions," *Arterioscler. Thromb. Vasc. Biol.*, vol. 20, no. 5, pp. 1262–1275, May 2000.

[17] J. N. E. Redgrave, J. K. Lovett, P. J. Gallagher, and P. M. Rothwell, "Histological Assessment of 526 Symptomatic Carotid Plaques in Relation to the Nature and Timing of Ischemic Symptoms The Oxford Plaque Study," *Circulation*, vol. 113, no. 19, pp. 2320–2328, May 2006.

[18] J. N. Redgrave, P. Gallagher, J. K. Lovett, and P. M. Rothwell, "Critical Cap Thickness and Rupture in Symptomatic Carotid Plaques The Oxford Plaque Study," *Stroke*, vol. 39, no. 6, pp. 1722–1729, Jun. 2008.

[19] B. Verhoeven, W. E. Hellings, F. L. Moll, J. P. de Vries, D. P. V. de Kleijn, P. de Bruin, E. Busser, A. H. Schoneveld, and G. Pasterkamp, "Carotid atherosclerotic plaques in patients with transient ischemic attacks and stroke have unstable characteristics compared

with plaques in asymptomatic and amaurosis fugax patients," *Journal of Vascular Surgery*, vol. 42, no. 6, pp. 1075–1081, Dec. 2005.

[20] A. V. Finn, M. Nakano, J. Narula, F. D. Kolodgie, and R. Virmani, "Concept of Vulnerable/Unstable Plaque," *Arterioscler Thromb Vasc Biol*, vol. 30, no. 7, pp. 1282–1292, Jul. 2010.

[21] N. Maldonado, A. Kelly-Arnold, Y. Vengrenyuk, D. Laudier, J. T. Fallon, R. Virmani, L. Cardoso, and S. Weinbaum, "A mechanistic analysis of the role of microcalcifications in atherosclerotic plaque stability: potential implications for plaque rupture," *Am J Physiol Heart Circ Physiol*, vol. 303, no. 5, pp. H619–H628, Sep. 2012.

[22] L. Cardoso and S. Weinbaum, "Changing Views of the Biomechanics of Vulnerable Plaque Rupture: A Review," *Ann Biomed Eng*, vol. 42, no. 2, pp. 415–431, Jul. 2013.

[23] M. J. Davies, P. D. Richardson, N. Woolf, D. R. Katz, and J. Mann, "Risk of thrombosis in human atherosclerotic plaques: role of extracellular lipid, macrophage, and smooth muscle cell content.," *Br Heart J*, vol. 69, no. 5, pp. 377–381, May 1993.

[24] P. D. Richardson, M. J. Davies, and G. V. R. Born, "Originally published as Volume 2, Issue 8669INFLUENCE OF PLAQUE CONFIGURATION AND STRESS DISTRIBUTION ON FISSURING OF CORONARY ATHEROSCLEROTIC PLAQUES," *The Lancet*, vol. 334, no. 8669, pp. 941–944, Oct. 1989.

[25] C. L. Lendon, M. J. Davies, G. V. R. Born, and P. D. Richardson, "Atherosclerotic plaque caps are locally weakened when macrophages density is increased," *Atherosclerosis*, vol. 87, no. 1, pp. 87–90, Mar. 1991.

[26] N. Takaya, C. Yuan, B. Chu, T. Saam, H. Underhill, J. Cai, N. Tran, N. L. Polissar, C. Isaac, M. S. Ferguson, G. A. Garden, S. C. Cramer, K. R. Maravilla, B. Hashimoto, and T. S. Hatsukami, "Association between carotid plaque characteristics and subsequent ischemic cerebrovascular events: a prospective assessment with MRI--initial results," *Stroke*, vol. 37, no. 3, pp. 818–823, Mar. 2006.

[27] T. J. Czernuszewicz, J. W. Homeister, M. C. Caughey, M. A. Farber, J. J. Fulton, P. F. Ford, W. A. Marston, R. Vallabhaneni, T. C. Nichols, and C. M. Gallippi, "Non-invasive in Vivo Characterization of Human Carotid Plaques with Acoustic Radiation Force Impulse Ultrasound: Comparison with Histology after Endarterectomy," *Ultrasound in Medicine & Biology*, vol. 41, no. 3, pp. 685–697, Mar. 2015.

[28] C. Yuan, W. S. Kerwin, M. S. Ferguson, N. Polissar, S. Zhang, J. Cai, and T. S. Hatsukami, "Contrast-enhanced high resolution MRI for atherosclerotic carotid artery tissue characterization," *Journal of Magnetic Resonance Imaging*, vol. 15, no. 1, pp. 62–67, 2002.

[29] F. A. Duck, *Physical Properties of Tissues: A Comprehensive Reference Book*. Academic Press, 2013.

[30] V. A. D. Grosso and C. W. Mader, “Speed of Sound in Pure Water,” *The Journal of the Acoustical Society of America*, vol. 52, no. 5B, pp. 1442–1446, Nov. 1972.

[31] R. W. Timme, “Speed of Sound in Castor Oil,” *The Journal of the Acoustical Society of America*, vol. 52, no. 3B, pp. 989–992, Sep. 1972.

[32] N. R. Miller, J. C. Bamber, and P. M. Meaney, “Fundamental limitations of noninvasive temperature imaging by means of ultrasound echo strain estimation,” *Ultrasound in Medicine & Biology*, vol. 28, no. 10, pp. 1319–1333, Oct. 2002.

[33] S.-W. Huang, K. Kim, R. S. Witte, R. Olafsson, and M. O’Donnell, “Inducing and imaging thermal strain using a single ultrasound linear array,” *IEEE Trans Ultrason Ferroelectr Freq Control*, vol. 54, no. 9, pp. 1718–1720, Sep. 2007.

[34] K. Kim, S.-W. Huang, T. L. Hall, R. S. Witte, T. L. Chenevert, and M. O’Donnell, “Arterial vulnerable plaque characterization using ultrasound-induced thermal strain imaging (TSI),” *IEEE Trans Biomed Eng*, vol. 55, no. 1, pp. 171–180, Jan. 2008.

[35] Y. Shi, R. S. Witte, S. M. Milas, J. H. Neiss, X. C. Chen, C. A. Cain, and M. O’Donnell, “Microwave-Induced Thermal Imaging of Tissue Dielectric Properties,” *Ultrason Imaging*, vol. 25, no. 2, pp. 109–121, Apr. 2003.

[36] D. N. Stephens, A. M. Mahmoud, X. Ding, S. Lucero, D. Debaditya, F. T. H. Yu, X. Chen, and K. Kim, “Flexible Integration of Both High Imaging Resolution and High Power Arrays for Ultrasound-Induced Thermal Strain Imaging (US-TSI),” *IEEE Transactions on Ultrasonics, Ferroelectrics and Frequency Control*.

[37] J. R. Doherty, G. E. Trahey, K. R. Nightingale, and M. L. Palmeri, “Acoustic radiation force elasticity imaging in diagnostic ultrasound,” *IEEE Transactions on Ultrasonics, Ferroelectrics, and Frequency Control*, vol. 60, no. 4, pp. 685–701, Apr. 2013.

[38] J. J. Dahl, G. F. Pinton, L. Mark, V. Agrawal, K. R. Nightingale, and G. E. Trahey, “A Parallel Tracking Method for Acoustic Radiation Force Impulse Imaging,” *IEEE Trans Ultrason Ferroelectr Freq Control*, vol. 54, no. 2, pp. 301–312, Feb. 2007.

[39] L. Zhai, T. J. Polascik, W.-C. Foo, S. Rosenzweig, M. L. Palmeri, J. Madden, and K. R. Nightingale, “Acoustic radiation force impulse imaging of human prostates: initial in vivo demonstration,” *Ultrasound Med Biol*, vol. 38, no. 1, pp. 50–61, Jan. 2012.

[40] K. Nightingale, M. S. Soo, R. Nightingale, and G. Trahey, “Acoustic radiation force impulse imaging: in vivo demonstration of clinical feasibility,” *Ultrasound in Medicine & Biology*, vol. 28, no. 2, pp. 227–235, Feb. 2002.

[41] B. J. Fahey, R. C. Nelson, D. P. Bradway, S. J. Hsu, D. M. Dumont, and G. E. Trahey, “In vivo visualization of abdominal malignancies with acoustic radiation force elastography,” *Phys Med Biol*, vol. 53, no. 1, pp. 279–293, Jan. 2008.

[42] M. L. Palmeri, J. J. Dahl, D. B. MacLeod, S. A. Grant, and K. R. Nightingale, “On the feasibility of imaging peripheral nerves using acoustic radiation force impulse imaging,” *Ultrason Imaging*, vol. 31, no. 3, pp. 172–182, Jul. 2009.

[43] C. H. Seo, Y. Shi, S.-W. Huang, K. Kim, and M. O’Donnell, “Thermal strain imaging: a review,” *Interface Focus*, vol. 1, no. 4, pp. 649–664, Aug. 2011.

[44] C. Simon, P. Vanbaren, and E. S. Ebbini, “Two-dimensional temperature estimation using diagnostic ultrasound,” *IEEE Trans Ultrason Ferroelectr Freq Control*, vol. 45, no. 4, pp. 1088–1099, 1998.

[45] R. Maass-Moreno and C. A. Damianou, “Noninvasive temperature estimation in tissue via ultrasound echo-shifts. Part I. Analytical model,” *The Journal of the Acoustical Society of America*, vol. 100, no. 4, pp. 2514–2521, Oct. 1996.

[46] M. O’Donnell, A. R. Skovoroda, B. M. Shapo, and S. Y. Emelianov, “Internal displacement and strain imaging using ultrasonic speckle tracking,” *IEEE Transactions on Ultrasonics, Ferroelectrics and Frequency Control*, vol. 41, no. 3, pp. 314–325, 1994.

[47] J. Ophir, I. Céspedes, H. Ponnekanti, Y. Yazdi, and X. Li, “Elastography: A quantitative method for imaging the elasticity of biological tissues,” *Ultrasonic Imaging*, vol. 13, no. 2, pp. 111–134, Apr. 1991.

[48] M. A. Lubinski, S. Y. Emelianov, and M. O’Donnell, “Speckle tracking methods for ultrasonic elasticity imaging using short-time correlation,” *IEEE Trans Ultrason Ferroelectr Freq Control*, vol. 46, no. 1, pp. 82–96, 1999.

[49] E. S. Ebbini, “Phase-coupled two-dimensional speckle tracking algorithm,” *IEEE Trans Ultrason Ferroelectr Freq Control*, vol. 53, no. 5, pp. 972–990, May 2006.

[50] S. K. Alam, J. Ophir, and E. E. Konofagou, “An adaptive strain estimator for elastography,” *IEEE Transactions on Ultrasonics, Ferroelectrics and Frequency Control*, vol. 45, no. 2, pp. 461–472, 1998.

[51] T. Loupas, J. T. Powers, and R. W. Gill, “An axial velocity estimator for ultrasound blood flow imaging, based on a full evaluation of the Doppler equation by means of a two-dimensional autocorrelation approach,” *IEEE Transactions on Ultrasonics, Ferroelectrics and Frequency Control*, vol. 42, no. 4, pp. 672–688, 1995.

[52] M. Alessandrini, A. Basarab, H. Liebgott, and O. Bernard, “Myocardial motion estimation from medical images using the monogenic signal,” *IEEE Trans Image Process*, vol. 22, no. 3, pp. 1084–1095, Mar. 2013.

[53] G. F. Pinton, J. J. Dahl, and G. E. Trahey, “Rapid tracking of small displacements with ultrasound,” *IEEE Trans Ultrason Ferroelectr Freq Control*, vol. 53, no. 6, pp. 1103–1117, Jun. 2006.

[54] F. Viola and W. F. Walker, “A comparison of the performance of time-delay estimators in medical ultrasound,” *IEEE Transactions on Ultrasonics, Ferroelectrics and Frequency Control*, vol. 50, no. 4, pp. 392–401, 2003.

[55] B. Byram, G. E. Trahey, and M. Palmeri, “Bayesian speckle tracking. Part I: an implementable perturbation to the likelihood function for ultrasound displacement estimation,” *IEEE Trans Ultrason Ferroelectr Freq Control*, vol. 60, no. 1, pp. 132–143, Jan. 2013.

[56] B. Byram, G. E. Trahey, and M. Palmeri, “Bayesian Speckle Tracking. Part II: Biased Ultrasound Displacement Estimation,” *IEEE Trans Ultrason Ferroelectr Freq Control*, vol. 60, no. 1, pp. 144–157, Jan. 2013.

[57] L. Chen, R. J. Housden, G. M. Treece, A. H. Gee, and R. W. Prager, “A hybrid displacement estimation method for ultrasonic elasticity imaging,” *IEEE Trans Ultrason Ferroelectr Freq Control*, vol. 57, no. 4, pp. 866–882, Apr. 2010.

[58] M. L. Palmeri, M. H. Wang, J. J. Dahl, K. D. Frinkley, and K. R. Nightingale, “Quantifying Hepatic Shear Modulus In Vivo Using Acoustic Radiation Force,” *Ultrasound in Medicine & Biology*, vol. 34, no. 4, pp. 546–558, Apr. 2008.

[59] M. Tanter, J. Bercoff, A. Athanasiou, T. Deffieux, J.-L. Gennisson, G. Montaldo, M. Muller, A. Tardivon, and M. Fink, “Quantitative Assessment of Breast Lesion Viscoelasticity: Initial Clinical Results Using Supersonic Shear Imaging,” *Ultrasound in Medicine & Biology*, vol. 34, no. 9, pp. 1373–1386, Sep. 2008.

[60] H. L. V. Trees, *Detection, Estimation, and Modulation Theory*. John Wiley & Sons, 2004.

[61] C. Kasai, K. Namekawa, A. Koyano, and R. Omoto, “Real-Time Two-Dimensional Blood Flow Imaging Using an Autocorrelation Technique,” *IEEE Transactions on Sonics and Ultrasonics*, vol. 32, no. 3, pp. 458–464, 1985.

[62] G. C. Carter, “Coherence and time delay estimation,” *Proceedings of the IEEE*, vol. 75, no. 2, pp. 236–255, 1987.

[63] J. Krejza, M. Arkuszewski, S. E. Kasner, J. Weigele, A. Ustymowicz, R. W. Hurst, B. L. Cucchiara, and S. R. Messe, “Carotid Artery Diameter in Men and Women and the Relation to Body and Neck Size,” *Stroke*, vol. 37, no. 4, pp. 1103–1105, Apr. 2006.

[64] M. Naghavi, P. Libby, E. Falk, S. W. Casscells, S. Litovsky, J. Rumberger, J. J. Badimon, C. Stefanadis, P. Moreno, G. Pasterkamp, Z. Fayad, P. H. Stone, S. Waxman, P. Raggi, M. Madjid, A. Zarrabi, A. Burke, C. Yuan, P. J. Fitzgerald, D. S. Siscovick, C. L. de Korte, M. Aikawa, K. E. J. Airaksinen, G. Assmann, C. R. Becker, J. H. Chesebro, A. Farb, Z. S. Galis, C. Jackson, I.-K. Jang, W. Koenig, R. A. Lodder, K. March, J. Demirovic, M. Navab, S. G. Priori, M. D. Rekhter, R. Bahr, S. M. Grundy, R. Mehran, A. Colombo, E. Boerwinkle, C. Ballantyne, W. Insull, R. S. Schwartz, R. Vogel, P. W. Serruys, G. K. Hansson, D. P. Faxon, S. Kaul, H. Drexler, P. Greenland, J. E. Muller, R. Virmani, P. M. Ridker, D. P. Zipes, P. K. Shah, and J. T. Willerson, “From Vulnerable Plaque to

Vulnerable Patient A Call for New Definitions and Risk Assessment Strategies: Part I," *Circulation*, vol. 108, no. 14, pp. 1664–1672, Oct. 2003.

[65] J. H. Stein, C. E. Korcarz, R. T. Hurst, E. Lonn, C. B. Kendall, E. R. Mohler, S. S. Najjar, C. M. Rembold, and W. S. Post, "Use of Carotid Ultrasound to Identify Subclinical Vascular Disease and Evaluate Cardiovascular Disease Risk: A Consensus Statement from the American Society of Echocardiography Carotid Intima-Media Thickness Task Force Endorsed by the Society for Vascular Medicine," *Journal of the American Society of Echocardiography*, vol. 21, no. 2, pp. 93–111, Feb. 2008.

[66] J. A. Jensen and N. B. Svendsen, "Calculation of pressure fields from arbitrarily shaped, apodized, and excited ultrasound transducers," *IEEE Transactions on Ultrasonics, Ferroelectrics and Frequency Control*, vol. 39, no. 2, pp. 262–267, 1992.

[67] W. Walker, "A fundamental limit on delay estimation using partially correlated speckle signals," *Ultrasonics, Ferroelectrics and Frequency Control, IEEE Transactions on*, vol. 42, no. 2, pp. 301–308, Mar. 1995.

[68] K. K. Sheng-Wen Huang, "Inducing and Imaging Thermal Strain Using a Single Ultrasound Linear Array," *Ultrasonics, Ferroelectrics and Frequency Control, IEEE Transactions on*, no. 9, pp. 1718–1719, 2007.

[69] A. M. Mahmoud, D. Dutta, L. Lavery, D. N. Stephens, F. S. Villanueva, and K. Kim, "Noninvasive detection of lipids in atherosclerotic plaque using ultrasound thermal strain imaging: in vivo animal study," *J Am Coll Cardiol*, Jul. 2013.

[70] M. L. Palmeri, S. A. McAleavey, G. E. Trahey, and K. R. Nightingale, "Ultrasonic tracking of acoustic radiation force-induced displacements in homogeneous media," *IEEE Transactions on Ultrasonics, Ferroelectrics and Frequency Control*, vol. 53, no. 7, pp. 1300–1313, Jul. 2006.

[71] "Bioeffects considerations for the safety of diagnostic ultrasound. American Institute of Ultrasound in Medicine. Bioeffects Committee," *J Ultrasound Med*, vol. 7, no. 9 Suppl, pp. S1-38, Sep. 1988.

[72] H. Rivaz, E. M. Boctor, M. A. Choti, and G. D. Hager, "Real-Time Regularized Ultrasound Elastography," *IEEE Transactions on Medical Imaging*, vol. 30, no. 4, pp. 928–945, Apr. 2011.

[73] X. Ding, D. Dutta, A. M. Mahmoud, B. Tillman, S. A. Leers, and K. Kim, "An adaptive displacement estimation algorithm for improved reconstruction of thermal strain," *IEEE Transactions on Ultrasonics, Ferroelectrics, and Frequency Control*, vol. 62, no. 1, pp. 138–151, Jan. 2015.

[74] A. Russo, C. Murphy, V. Lessoway, and J. Berkowitz, "The prevalence of musculoskeletal symptoms among British Columbia sonographers," *Applied Ergonomics*, vol. 33, no. 5, pp. 385–393, Sep. 2002.

[75] K. E. Thomenius, “Evolution of ultrasound beamformers,” in , *1996 IEEE Ultrasonics Symposium, 1996. Proceedings*, 1996, vol. 2, pp. 1615–1622 vol.2.

[76] J. Bercoff, M. Tanter, and M. Fink, “Supersonic shear imaging: a new technique for soft tissue elasticity mapping,” *IEEE Transactions on Ultrasonics, Ferroelectrics, and Frequency Control*, vol. 51, no. 4, pp. 396–409, Apr. 2004.

[77] G. Montaldo, M. Tanter, J. Bercoff, N. Benech, and M. Fink, “Coherent plane-wave compounding for very high frame rate ultrasonography and transient elastography,” *IEEE Transactions on Ultrasonics, Ferroelectrics, and Frequency Control*, vol. 56, no. 3, pp. 489–506, Mar. 2009.

[78] E. S. Ebbini and C. A. Cain, “Multiple-focus ultrasound phased-array pattern synthesis: optimal driving-signal distributions for hyperthermia,” *IEEE Transactions on Ultrasonics, Ferroelectrics, and Frequency Control*, vol. 36, no. 5, pp. 540–548, Sep. 1989.

[79] K. Ranganathan and W. F. Walker, “A novel beamformer design method for medical ultrasound. Part I: Theory,” *IEEE Transactions on Ultrasonics, Ferroelectrics, and Frequency Control*, vol. 50, no. 1, pp. 15–24, Jan. 2003.

[80] K. Ranganathan and W. F. Walker, “A novel beamformer design method for medical ultrasound. Part II: Simulation results,” *IEEE Transactions on Ultrasonics, Ferroelectrics, and Frequency Control*, vol. 50, no. 1, pp. 25–39, Jan. 2003.

[81] M. M. Nguyen, X. Ding, F. Yu, and K. Kim, “Adaptive beamforming for thermal strain imaging using a single ultrasound linear array,” in *Ultrasonics Symposium (IUS), 2014 IEEE International*, 2014, pp. 1686–1689.

[82] X. Ding, M. M. Nguyen, I. B. James, K. G. Marra, J. P. Rubin, S. A. Leers, and K. Kim, “Improved Estimation of Ultrasound Thermal Strain Using Pulse Inversion Harmonic Imaging,” *Ultrasound in Medicine and Biology*, vol. 42, no. 5, pp. 1182–1192, May 2016.

[83] M. L. Palmeri and K. R. Nightingale, “On the thermal effects associated with radiation force imaging of soft tissue,” *IEEE Trans Ultrason Ferroelectr Freq Control*, vol. 51, no. 5, pp. 551–565, May 2004.

[84] R. S. C. Cobbold, *Foundations of Biomedical Ultrasound*. Oxford University Press, 2006.

[85] A. M. Mahmoud, X. Ding, D. Dutta, V. P. Singh, and K. Kim, “Detecting hepatic steatosis using ultrasound-induced thermal strain imaging: an ex vivo animal study,” *Phys Med Biol*, vol. 59, no. 4, pp. 881–895, Feb. 2014.

[86] D. Liu and E. S. Ebbini, “Real-time 2-D temperature imaging using ultrasound,” *IEEE Trans Biomed Eng*, vol. 57, no. 1, pp. 12–16, Jan. 2010.

[87] C. H. Seo, D. N. Stephens, J. Cannata, A. Dentinger, F. Lin, S. Park, D. Wildes, K. E. Thomenius, P. Chen, T. Nguyen, A. de La Rama, J. S. Jeong, A. Mahajan, K. Shivkumar, A. Nikoozadeh, O. Oralkan, U. Truong, D. J. Sahn, P. T. Khuri-Yakub, and M. O’Donnell,

"The feasibility of using thermal strain imaging to regulate energy delivery during intracardiac radio-frequency ablation," *IEEE Trans Ultrason Ferroelectr Freq Control*, vol. 58, no. 7, pp. 1406–1417, Jul. 2011.

[88] C.-Y. Lai, D. E. Kruse, C. F. Caskey, D. N. Stephens, P. L. Sutcliffe, and K. W. Ferrara, "Noninvasive thermometry assisted by a dual-function ultrasound transducer for mild hyperthermia," *IEEE Transactions on Ultrasonics, Ferroelectrics, and Frequency Control*, vol. 57, no. 12, pp. 2671–2684, Dec. 2010.

[89] D. Liu, A. Shrestha, R. Visaria, J. Bischof, and E. S. Ebbini, "Noninvasive temperature estimation using diagnostic ultrasound: In vivo results," *The Journal of the Acoustical Society of America*, vol. 123, no. 5, pp. 3000–3000, 2008.

[90] N. R. Miller, J. C. Bamber, and G. R. ter Haar, "Imaging of temperature-induced echo strain: preliminary in vitro study to assess feasibility for guiding focused ultrasound surgery," *Ultrasound in Medicine & Biology*, vol. 30, no. 3, pp. 345–356, Mar. 2004.

[91] M. A. Lediju, M. J. Pihl, J. J. Dahl, and G. E. Trahey, "Quantitative Assessment of the Magnitude, Impact and Spatial Extent of Ultrasonic Clutter," *Ultrason Imaging*, vol. 30, no. 3, pp. 151–168, Jul. 2008.

[92] J. J. Dahl and N. M. Sheth, "Reverberation Clutter from Subcutaneous Tissue Layers: Simulation and in Vivo Demonstrations," *Ultrasound in Medicine & Biology*, vol. 40, no. 4, pp. 714–726, Apr. 2014.

[93] T. Christopher, "Finite amplitude distortion-based inhomogeneous pulse echo ultrasonic imaging," *IEEE Trans Ultrason Ferroelectr Freq Control*, vol. 44, no. 1, pp. 125–139, 1997.

[94] J. R. Doherty, J. J. Dahl, and G. E. Trahey, "Harmonic Tracking of Acoustic Radiation Force Induced Displacements," *IEEE Trans Ultrason Ferroelectr Freq Control*, vol. 60, no. 11, pp. 2347–2358, Nov. 2013.

[95] P. Song, H. Zhao, M. W. Urban, A. Manduca, S. V. Pislaru, R. R. Kinnick, C. Pislaru, J. F. Greenleaf, and S. Chen, "Improved Shear Wave Motion Detection Using Pulse-Inversion Harmonic Imaging With a Phased Array Transducer," *IEEE Transactions on Medical Imaging*, vol. 32, no. 12, pp. 2299–2310, Dec. 2013.

[96] M. M. Nguyen, S. Zhou, J. Robert, V. Shamdasani, and H. Xie, "Development of Oil-in-Gelatin Phantoms for Viscoelasticity Measurement in Ultrasound Shear Wave Elastography," *Ultrasound in Medicine & Biology*, vol. 40, no. 1, pp. 168–176, Jan. 2014.

[97] T. Czernuszewicz and C. Gallippi, "On the Feasibility of Quantifying Fibrous Cap Thickness with Acoustic Radiation Force Impulse (ARFI) Ultrasound," *IEEE Transactions on Ultrasonics, Ferroelectrics, and Frequency Control*, vol. PP, no. 99, pp. 1–1, 2016.

[98] L. Zhai, J. Madden, W.-C. Foo, M. L. Palmeri, V. Mouraviev, T. J. Polascik, and K. R. Nightingale, "Acoustic Radiation Force Impulse Imaging of Human Prostates Ex Vivo," *Ultrasound in Medicine & Biology*, vol. 36, no. 4, pp. 576–588, Apr. 2010.

[99] V. Rotemberg, M. Palmeri, S. Rosenzweig, S. Grant, D. Macleod, and K. Nightingale, "Acoustic Radiation Force Impulse (ARFI) Imaging-Based Needle Visualization," *Ultrason Imaging*, vol. 33, no. 1, pp. 1–16, Jan. 2011.

[100] A. P. Sarvazyan, O. V. Rudenko, S. D. Swanson, J. B. Fowlkes, and S. Y. Emelianov, "Shear wave elasticity imaging: a new ultrasonic technology of medical diagnostics," *Ultrasound in Medicine & Biology*, vol. 24, no. 9, pp. 1419–1435, Dec. 1998.

[101] R. R. Bouchard, J. J. Dahl, S. J. Hsu, M. L. Palmeri, and G. E. Trahey, "Image quality, tissue heating, and frame rate trade-offs in acoustic radiation force impulse imaging," *IEEE Transactions on Ultrasonics, Ferroelectrics, and Frequency Control*, vol. 56, no. 1, pp. 63–76, Jan. 2009.

[102] D. P. Shattuck, M. D. Weinshenker, S. W. Smith, and O. T. von Ramm, "Explososcan: a parallel processing technique for high speed ultrasound imaging with linear phased arrays," *J. Acoust. Soc. Am.*, vol. 75, no. 4, pp. 1273–1282, Apr. 1984.

[103] N. C. Rouze, M. L. Palmeri, and K. R. Nightingale, "Measurement of the frequency dependent phase velocity and attenuation from the Fourier description of shear wave propagation: Addressing geometric spreading arising from spatially asymmetric Gaussian excitations," in *Ultrasonics Symposium (IUS), 2015 IEEE International*, 2015, pp. 1–4.

[104] N. C. Rouze, M. L. Palmeri, and K. R. Nightingale, "An analytic, Fourier domain description of shear wave propagation in a viscoelastic medium using asymmetric Gaussian sources," *The Journal of the Acoustical Society of America*, vol. 138, no. 2, pp. 1012–1022, Aug. 2015.

[105] K. Nightingale, M. Palmeri, and G. Trahey, "Analysis of contrast in images generated with transient acoustic radiation force," *Ultrasound in Medicine & Biology*, vol. 32, no. 1, pp. 61–72, Jan. 2006.

[106] E. Montagnon, S. Hissoiny, P. Després, and G. Cloutier, "Real-time processing in dynamic ultrasound elastography: A GPU-based implementation using CUDA," in *2012 11th International Conference on Information Science, Signal Processing and their Applications (ISSPA)*, 2012, pp. 472–477.

[107] S. Rosenzweig, M. Palmeri, and K. Nightingale, "GPU-based real-time small displacement estimation with ultrasound," *IEEE Transactions on Ultrasonics, Ferroelectrics, and Frequency Control*, vol. 58, no. 2, pp. 399–405, Feb. 2011.

[108] B. J. Fahey, M. L. Palmeri, and G. E. Trahey, "The Impact of Physiological Motion on Tissue Tracking During Radiation Force Imaging," *Ultrasound Med Biol*, vol. 33, no. 7, pp. 1149–1166, Jul. 2007.

[109] B. J. Fahey, S. J. Hsu, and G. E. Trahey, “A novel motion compensation algorithm for acoustic radiation force elastography,” *IEEE Trans Ultrason Ferroelectr Freq Control*, vol. 55, no. 5, pp. 1095–1111, May 2008.

[110] D. M. Giannantonio, D. M. Dumont, G. E. Trahey, and B. C. Byram, “Comparison of Physiological Motion Filters for In Vivo Cardiac ARFI,” *Ultrason Imaging*, vol. 33, no. 2, pp. 89–108, Apr. 2011.

[111] D. Dutta, A. M. Mahmoud, S. A. Leers, and K. Kim, “Motion artifact reduction in ultrasound based thermal strain imaging of atherosclerotic plaques using time-series analysis,” *IEEE Transactions on Ultrasonics, Ferroelectrics and Frequency Control*, vol. 60, no. 8, pp. 1660–1668, 2013.

[112] Y. Deng, M. L. Palmeri, N. C. Rouze, S. J. Rosenzweig, M. F. Abdelmalek, and K. R. Nightingale, “Analyzing the Impact of Increasing Mechanical Index and Energy Deposition on Shear Wave Speed Reconstruction in Human Liver,” *Ultrasound in Medicine and Biology*, vol. 41, no. 7, pp. 1948–1957, Jul. 2015.

[113] T. Shiina, K. R. Nightingale, M. L. Palmeri, T. J. Hall, J. C. Bamber, R. G. Barr, L. Castera, B. I. Choi, Y.-H. Chou, D. Cosgrove, C. F. Dietrich, H. Ding, D. Amy, A. Farrokh, G. Ferraioli, C. Filice, M. Friedrich-Rust, K. Nakashima, F. Schafer, I. Sporea, S. Suzuki, S. Wilson, and M. Kudo, “WFUMB Guidelines and Recommendations for Clinical Use of Ultrasound Elastography: Part 1: Basic Principles and Terminology,” *Ultrasound in Medicine & Biology*, vol. 41, no. 5, pp. 1126–1147, May 2015.

[114] T. Deffieux, J.-L. Gennisson, L. Bousquet, M. Corouge, S. Cosconea, D. Amroun, S. Tripon, B. Terris, V. Mallet, P. Sogni, M. Tanter, and S. Pol, “Investigating liver stiffness and viscosity for fibrosis, steatosis and activity staging using shear wave elastography,” *Journal of Hepatology*, vol. 62, no. 2, pp. 317–324, Feb. 2015.